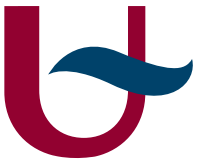

UNIVERSITEIT ANTWERPEN

Faculteit Wetenschappen

Departement Fysica

Theoretical study of excitons in semiconductor quantum wires and related systems

Proefschrift voorgelegd tot het behalen van de graad van doctor in de wetenschappen aan de Universiteit Antwerpen te verdedigen door

Yosyp Sidor

Promotor: Prof. dr. F. M. Peeters
Co-promotor: Prof. dr. B. Partoens

Antwerpen 2007

Contents

List of abbreviations **v**

1 Introduction **1**
1.1 Application of quantum wires 3
1.2 Growth of quantum wires 6
1.2.1 T-shaped quantum wires 6
1.2.2 V-shaped quantum wires 8
1.2.3 Self-assembled quantum wires 9
1.3 Theoretical concepts 11
1.3.1 Band structure of semiconductors. The **k**·**p** method 11
1.3.2 Effective mass theory for a single band 14
1.3.3 Excitons 15
1.3.4 Strain effects on the band structure 17
1.3.5 Presence of a magnetic field 19
1.4 Theoretical results on quantum wires 20
1.5 Overview of the thesis 23
1.5.1 Model Hamiltonian 23
1.5.2 Organization of the thesis 25

2 Electron wavefunction spill-over in self-assembled InAs/InP quantum wires 29
2.1 Introduction 29
2.2 Growth of quantum wires 30
2.3 Experimental and theoretical method 31
2.4 Experimental versus numerical results and discussion 34
2.5 Conclusions 41

3 Exciton in a quantum wire in the presence of parallel and perpendicular magnetic fields 45
3.1 Introduction 45
3.2 Theory 47
3.2.1 Theoretical model and basic equations 47
3.2.2 Solution methods 51
3.2.3 Coulomb interaction 52
3.3 Self-assembled quantum wires with strain 53
3.4 Contribution of Coulomb interaction to the photoluminescence energy 55
3.5 Quantum wire states in a magnetic field 57
3.6 Conclusions 64

4 Exciton confinement in InAs/InP quantum wires and quantum wells in the presence of a magnetic field 67
4.1 Introduction 67
4.2 Theoretical model 68
4.3 Experimental setup 72
4.4 Comparison of vertical confinement in quantum wires and wells 72
4.5 Width fluctuations in quantum well 82
4.6 Conclusions 85

5 Influence of the shape and size of a quantum wire on the trion binding energy 87
5.1 Introduction 87
5.2 Theoretical model 88
5.3 Numerical results and discussions 90
5.4 Conclusions 96

6 Excitons in coupled InAs/InP self-assembled quantum wires 99

6.1 Introduction 99
6.2 Model Hamiltonian 100
6.3 Comparison with experiment 103
6.4 Inter-wire coupling: a theoretical investigation 106
6.5 Conclusions 113

7 High-field magneto-excitons in unstrained GaAs/$Al_xGa_{1-x}As$ quantum dots 117
7.1 Introduction 117
7.2 Theoretical formalism and model 119
7.3 Extent of the particles and the Coulomb energies 123
7.4 Magneto-exciton transitions and comparison between theory and experiment 126
7.5 Conclusions 133

Summary 135

Samenvatting 139

References 145

Curriculum Vitae 157

List of publications 159

List of abbreviations

(in alphabetic order)

Abbreviation or symbol	
1D (2D, 3D)	one-(two-, three-) dimensional
AFM	atomic force microscopy
CEO	cleaved-edge-overgrowth
CQWRs	coupled quantum wires
DOS	density of states
hh	heavy-hole
lh	light-hole
MBE	molecular-beam epitaxy
ML	monolayer
MOVPE	metal-organic vapor phase epitaxy
PL	photoluminescence
QD	quantum dot
QW	quantum well
QWR	quantum wire

Abbreviation or symbol	
SILO	strain-induced lateral-layer ordering
STM	scanning tunneling microscopy
TEM	transmission electron microscopy
XTEM	cross-sectional transmission electron microscopy

1

Introduction

Since the invention by Esaki and Tsu [1] in the 1970s semiconductor quantum wells and superlattices have evolved from scientific curiosities into realization of wealth-created semiconductor devices. During the 1980s, the improved growth techniques have enabled experimentalists to fabricate systems of lower dimensionality, namely quantum wires and quantum dots. In contrast to quantum wells (QWs), where carriers are localized in the direction perpendicular to the layers but move freely in the layer plane, in quantum wires (QWRs) carriers are localized in two directions and move freely along the wire axis. In quantum dots (QDs) they are confined in all three directions resulting in a totally discrete energy spectrum.

Semiconductor QWRs has been studied intensively worldwide for a wide spectrum of materials. Such one-dimensional (1D) nanostructures are not only interesting for fundamental research due to their unique structural and physical properties relative to their bulk counterparts, but also offer fascinating potential for future technological applications. QWRs are promising candidates for opto-electronic and microelectronic devices, following the next generation of classical heterostructures and QWs which are now widely used in many applications, as for instance, heterostructure-based light-emitting diodes, heterostructure bipolar transistors, high-electron-mobility transistors and double heterostructure laser [2]. In particular, a QWR structure has been proposed as a 1D active region for a semiconductor laser where the electron and hole

carriers are allowed to move only in one direction. In contrast, more familiar semiconductor lasers are 3D double heterostructure lasers and 2D QW lasers. Because the 1D density of states (DOS) becomes more enhanced at the bottom of its band edge than the 2D or 3D DOS, a QWR laser is expected to show improvement in lasing performance [3–5].

For application of nanostructures in optoelectronics devices, as in lasers, photodetectors, and amplifiers, a large size homogeneity and spatial distribution is required. This can be achieved by the self-assembly growth process. In recent years there has been a large and growing interest in the fabrication of semiconductor self-assembled nanostructures [6, 7]. In this case the quantum structures are formed by the Stranski-Krastanov mode due to the strain relaxation during heteroepitaxial growth, in which the materials that are deposited on top of each other have substantially different lattice parameters. It was demonstrated [8, 9] that not only self-assembled QD, but also self-assembled QWR structures can be obtained by the molecular-beam epitaxy (MBE) growth method, e.g. InAs on InP(001) substrate, having 3.2 % lattice mismatch. Depending on the wire size and composition, emission tuning capability in the 1.2-1.9 μm range has been demonstrated. The self-assembled InAs/InP quantum QWRs are of particular interest for lasers. Very recently, lasing emission at a wavelength of 1.66 μm from three stacked layers of InAs QWRs as active zone and aluminum-free waveguides on (001)InP substrates was reported [10], showing better QWR laser characteristics than from those based on self-assembled QD systems. Since this QWR lasers could easily reach longer wavelengths than 1.55 μm, they can potentially be applied in optical telecommunication, gas sensing, and molecular spectroscopy [10]. However, a small number of theoretical works has been reported up to date for InAs/InP self-assembled QWRs.

The main goal of my thesis is a theoretical study of the excitonic properties in semiconductor QWRs. Excitons dominate the optical properties of these 1D structures, producing broad or sharp absorption and photoluminescence (PL) lines. The confinement of the electron and the hole is responsible for the properties of the exciton in a QWR. Confinement of the particles can be controlled through the size and shape of the QWR as well as through the selection of structure and barrier materials to produce various band offsets. The application of a magnetic field can give important information about the exciton confinement. Therefore, theoretical investigations of excitons in QWRs is a strong theoretical tool to provide valuable information about QWR characteristics, as size uniformity, dimensions and PL spectrum.

In this thesis, I will consider self-assembled InAs/InP and GaAs/AlGaAs V-shaped QWRs. The calculated PL transition energies in these structures are compared with available experimental data in order to deduce the dimensions of the wires. Both wires are investigated theoretically in the presence of an external magnetic field applied along different directions of the QWRs. The computed exciton diamagnetic shift for both V-shaped and self-assembled QWRs

are reported, and a detailed comparison is obtained with available magneto-PL experimental data. Since strain is important for the formation of the self-assembled QWRs, results on the influence of strain on the electron and hole confinement will also be presented. Further, exciton coupling in self-assembled InAs/InP coupled QWRs is considered. The charge confinement in InAs/InP based QWs and self-assembled QWRs is examined, where for the narrow QW a local circular width fluctuation is included in order to describe the localization of the exciton along the QW. Lastly, the formation of negatively and positively charged excitons in self-assembled InAs/InP and GaAs/AlGaAs V-shaped QWRs is discussed. Additionally, the magnetic field dependence of the excitonic states in unstrained GaAs/AlGaAs QD is studied. Where possible a comparison is made with experimental data.

In this chapter the general knowledge about a semiconductor QWR is presented. First, I will discuss the application of QWRs. Then, I will review some of the existing growth techniques to fabricate QWRs. The theoretical fundamental concepts are further introduced, where the theories for calculating band structures, the excitons and charged excitons in bulk and nanostructures, the influence of strain on the confinement of particles and the presence of an external magnetic field are shortly described. Finally, I will give an overview of my thesis.

1.1 APPLICATION OF QUANTUM WIRES

One of the main directions of contemporary semiconductor physics is the study of low dimensional structures, in order to realize novel devices that make use of quantum confinement effects. In this section I will explain why QWRs are attractive for lasing and also consider the device applications based on 1D quantum structures.

The decreased dimensionality of the free carrier motion results in a modification of the DOS of the carriers. The physical meaning of DOS is a measure of the maximum number of carriers that can occupy an energy range. The DOS, due to carrier motion in the x-, y- and z-directions of the active region in a bulk structure, is schematically shown in Fig. 1.1(a). It can be seen that for a given conduction band or valence band, the DOS is small near the edge of the band and increases with increasing energy.

By reducing the active layer thickness to the order of the de Broglie wavelength a two-dimensional QW is realized (see Fig. 1.1(b)). The corresponding DOS, due to confined carrier motion in the z-direction has a step-like shape offering an improvement over the bulk system. In the QW the number of electrons and holes populating the CB and VB is largest near the edges, therefore such 2D confined quantum structure is more attractive for a laser device. Furthermore, the energy of the optical transition based on QW laser (*i.e.* frequency

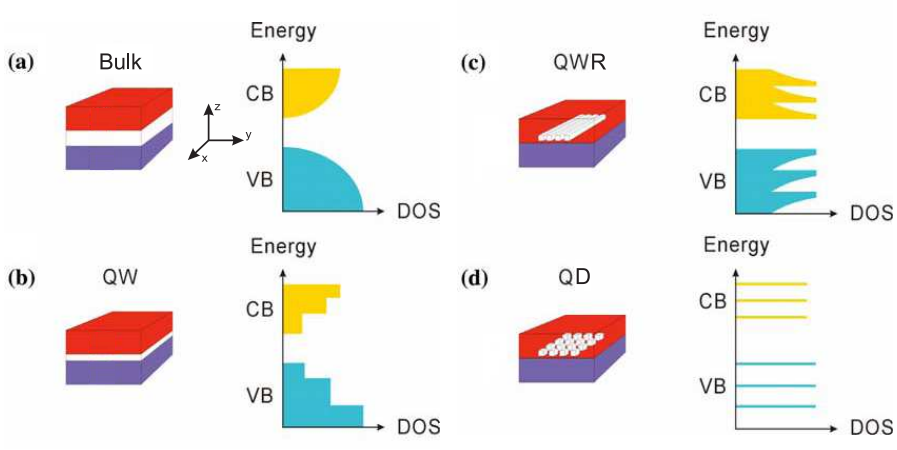

FIG. 1.1: Schematic diagram of the DOS in the conduction band (CB) and valence band (VB) for a (a) bulk, (b) QW, (c) QWR, and (d) QD.

of the output light) can be controlled by the well thickness. The discretisation of the energy levels also means that optical transitions will be sharper (*i.e.* a sharp line in the laser output frequency). As a result, these quantum-size effects significantly reduce the threshold current density and its temperature dependence, and shorten the emission wavelength.

One can further limit the motion of the carriers in the y-direction, as in a QWR (see Fig. 1.1(c)) where carriers are confined in two directions, or also in x-direction considering a QD (see Fig. 1.1(d)) where carriers are confined in all three directions and thus move in zero dimension. The shape of the DOS in QWR and QD is further improved compared to QW. It has an infinite value near the edges of the bands for the QWR whereas in the QD, carriers occupy discrete levels. Therefore, the QWR and QD lasers are expected to resemble the spectral linewidth of gas and solid-state lasers more closely than the conventional double heterostructure and QW lasers.

A quantum wire laser was first achieved by Kapon and coworkers [4] in 1989, though lasing occurred only at higher subbands in multi-mode V-shaped GaAs/AlGaAs wires (in section 1.2 I will describe the methods to fabricate the V-shaped and other shaped QWRs). In 1993, Wegscheider and coworkers [5] demonstrated ground-state lasing in T-shaped GaAs/AlGaAs QWRs. Laser with an active volume consisting of only a single T-shaped QWR was demonstrated by Hayamizu *et al.* [11] in 2002. In 2006, F. Suárez *et. al* presented [10] results on the growth by atomic layer molecular beam epitaxy and characterization of lasers with stacked layers of InAs/InP self-assembled QWRs as active zone. Moreover, nowadays semiconductor QWR structures can be realized for several other applications. Interacting 1D semiconductor quantum

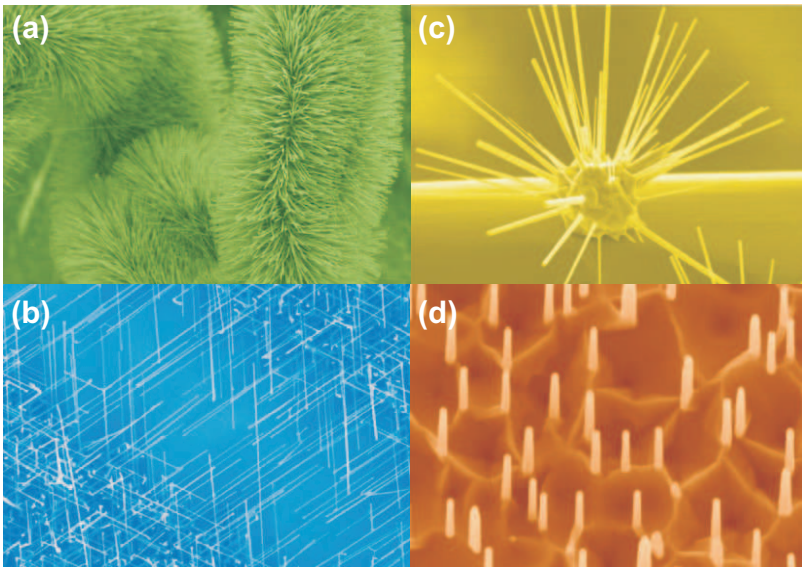

Fig. 1.2: A group of freestanding nanostructures based on ZnO: a) cluster of nanowires growing like brushes around a microwire; b) nanowires oriented with threefold symmetry; c) nanorods growing radially on the surface of a particle; d) nanorods extending from peaks of interconnected ZnO pyramids (from Ref. [21]).

structures are of interest with respect to fundamental investigations on tunnel coupling between two quantum systems. Recently, it was demonstrated that level spectroscopy and identification of single and coupled QWR states can be established by all-electrical means. This paves the way for quantum engineering of coupled quantum waveguide devices, such as bi-directional couplers [12], quantum waveguide inverters [13]. Possible other applications are in quantum information processing [14]. In particular, 1D electron transport in combination with wavefunction engineering in two QWRs coupled through a potential barrier has been proposed for the elementary quantum bit realization [15]. Besides, coupled QWRs can be used for light-emitting devices, such as diodes [16]. All these QWRs are embedded in a matrix. Recently also freestanding 1D nanowires and nonorods (see Fig. 1.2) were obtained. They provide a great potential for applications, such as transistors [17], diodes [18], memory elements [19], and chemical and biological sensors [20]. These structures have unique size-dependent mechanical properties, an increased luminescence efficiency and a reduced threshold for laser operation [21]. The QWRs studied in this work are the embedded QWRs, not the freestanding ones.

1.2 GROWTH OF QUANTUM WIRES

Thanks to progress in the fabrication technology of semiconductor nanometer-sized structures, a substantial number of growth techniques have been developed to fabricate QWRs. In 1982, a first step toward the realization of a 1D QWR was reported by Petroff *et al.* [22], where GaAs/AlGaAs quantum well-wires with dimensions as small as 200×200 Å were fabricated using MBE combined with electron-beam lithography and wet/dry chemical etching. Another attempt to obtain QWRs was done by Kash *et al.* [23], who employed a direct processing of QWs into QWRs using the same growth technique. However, large wire size fluctuations resulting from lithography and chemical etching processes was observed, and the wire dimensions were rather large, *i.e.* of order 1000 Å.

Since the end of the 1980s much efforts have been concentrated on the *in situ* methods of the formation of QWRs owing to the availability of advanced epitaxial growth techniques. In 1987 Kapon *et al.* [4] fabricated GaAs/AlGaAs V-shaped QWR (V-QWR) using a novel (at that time) heterostructure patterning technique. The V-QWRs were grown by metal-organic vapor phase epitaxy (MOVPE) growth method. A year later, a GaAs/AlGaAs T-shaped QWR (T-QWR) was obtained by Pfeiffer *et al.* [24] using a MBE machine and cleaved-edge-overgrowth (CEO) technique. Recently, González *et al.* demonstrated that InAs/InP self-organized QWRs can be formed through Stranski-Krastanow growth mode due to their lattice and energy gap mismatch. Moreover, there exists several other types of QWRs, namely, ridge-type QWRs, QWRs on sidewalls, QWRs based on control of monoatomic or multiatomic steps, and QWRs on corrugated high-index substrates including freestanding 1D nanowires and nonorods. A detailed overview of growth methods and formation of such QWRs is given in Refs. [21, 25]. Nevertheless, I will focus my discussion on the T-shaped, V-shaped, and self-assembled QWRs, since they represent the most investigated QWR nanostructures.

1.2.1 T-shaped quantum wires

The concept of the T-shaped QWR structure was originally proposed by Chang, Chang, and Esaki [26] in 1985. In 1990, the CEO method combined with MBE, was developed by Pfeiffer *at al.* at Bell Laboratories, which enabled them to combine two thin-film growth processes in two different directions to define QWRs [24]. In fact, they not only fabricated the T-QWR structure by the CEO method, but also showed PL results [27] in 1992, and demonstrated laser action by means of optical pumping [5] in 1993 and by means of current injection [28] in 1994.

The fabrication process consists of three steps, as illustrated in Fig. 1.3. In the first step, a GaAs/AlGaAs single or multiple QW is grown on a [001] GaAs

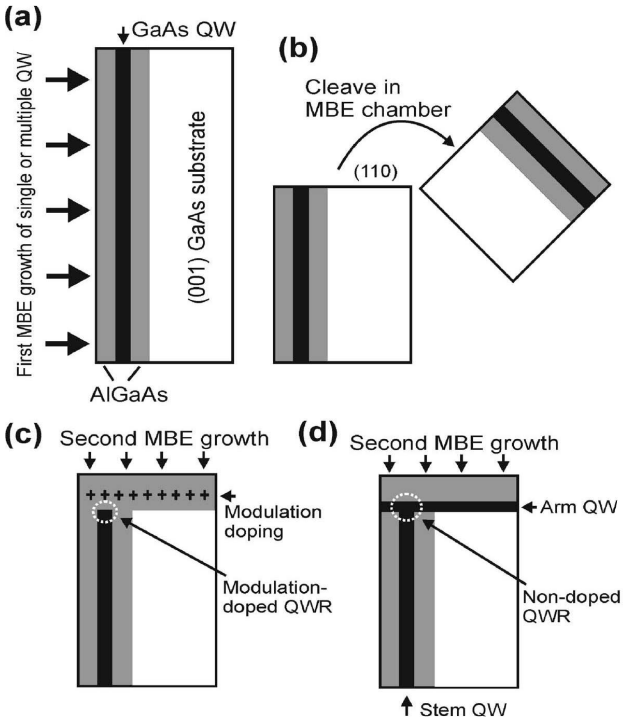

Fig. 1.3: Schematic illustration of the fabrication processes of T-shaped GaAs/AlGaAs QWRs: (a) growth of single or multiple QW, (b) cleave in MBE chamber, (c) and (d) growth of T-shaped GaAs/AlGaAs QWRs (from Ref. [25]).

substrate (see Fig. 1.3(a)). Then, the sample is cleaved in ultrahigh vacuum chamber of a MBE machine to expose the [110] surface (see Fig. 1.3(b)). In the third step, a second MBE growth is immediately performed after the cleavage on the exposed [110] surface. With such method two different structures can be grown: a modulation-doped AlGaAs layer (see Fig. 1.3(c)) or a GaAs well layer followed by an AlGaAs barrier layer (see Fig. 1.3(d)). In the first structure, electrons are electrostatically confined at the intersection of the first grown QW and the overgrown modulation-doped AlGaAs layers. In the second structure, 1D electronic and hole states are formed at the T intersection of two parent QWs, namely the first QW forming the 'stem' part of the letter 'T' and the second QW forming the 'arm' part of it, as schematically shown in Fig. 1.3(d). The typical QWR size of 52×48 Å, which is formed quantum mechanically at the T-shaped intersection, was observed recently [29]. The T-QWR is a convenient structure for electron transport investigation since the 1D electron gas is smoothly connected to the arm QW. This makes the formation of electrical

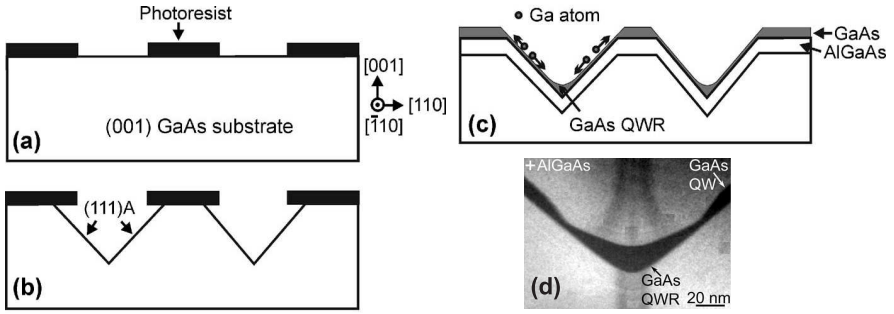

FIG. 1.4: Schematic drawing of the fabrication processes of V-shaped GasAs/AlGaAs QWRs: (a) prepartion of photoresist pattern, (b) formation of V grooves by wet chemical etching, (c) growth of V-shaped GaAs/AlGaAs QWRs (from Ref. [25]). (d) Cross-sectional transmission electron microscopy (XTEM) image of the GaAs/AlGaAs QWR (from Ref. [45]).

contacts to QWRs easier. The properties of 1D excitons has been intensively studied in such T-QWR structures (see, for example, Refs. [11, 30–36]).

1.2.2 V-shaped quantum wires

In the late 1980s Kapon *et al.* [37, 38] reported a novel selective-growth method using MBE on non-planar substrates to achieve lateral confinement by QW thickness variation. Lately, they demonstrated laser action by current injection in the quasi-1D QWRs [4] obtained by a MOVPE selective-growth method on V-shaped QWRs defined by conventional photolithography and wet chemical etching.

The typical fabrication process of V-QWR is illustrated in Fig. 1.4. First, using photolithography or electron-beam lithography a photoresist pattern is formed on a GaAs substrate (see Fig. 1.4(a)). Then, V-shaped grooves composed of two intersecting (111)A sidewall facets were realized by wet chemical etching (see Fig. 1.4(b)). In the final step, GaAs QWRs were fabricated at the V-groove bottom by growing GaAs/AlGaAs multilayers on this substrate because the growth rate of GaAs at the V-groove bottom is usually higher than that on the sidewall facets under the growth conditions (see Fig. 1.4(c)). Such vertically stacked GaAs/AlGaAs V-QWRs were obtained by Y. Nagamune *et. al.* [39]. Figure 1.4(d) shows the high-resolution secondary electron image of the region near the vertically stacked GaAs/AlGaAs QWRs. The V-QWR structure has proved itself as one of the most studied structure for 1D exciton properties. A large number of publications have been devoted to the investigation of such V-QWR structures [4, 39–43], including those reported in recent years [16, 44, 45].

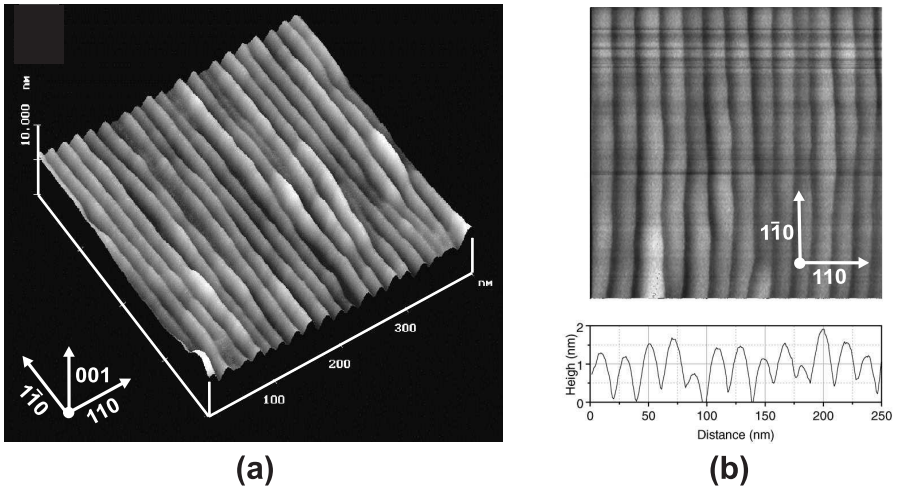

Fig. 1.5: (a) Typical atomic force microscopy (AFM) image of an uncapped InAs/InP QWRs grown by MBE on an InP(001) substrate (from Ref. [8]) and (b) AFM topographic image of such wires. A periodicity of 20 and 1.5 nm peak to valley amplitude can be obtained from this AFM profile (from Ref. [9]).

1.2.3 Self-assembled quantum wires

In 1993, Cheng *et al.* reported [46] the fabrication and operation of $Ga_xIn_{1-x}P$ heterostructure laser diodes with a multiple QWR active region based on the strain-induced lateral-layer ordering (SILO) process. Strained multiple QWRs were fabricated simply by sandwiching a thin layer of short-period superlattices (SPSs) during gas source MBE with thick bulk materials in the growth direction. The basic technique of the SILO process is based on the deposition of alternating thin layers of two different materials to form a SPS, where each of the layers is strained with respect to the growth substrate [47]. The key factor of the SILO process is that the strain in each of the alternating layers is opposite in sign (tensile and compressive) to ensure a total minimal strain (strain balance) due to lattice relaxation. Later, they reported a similar QWR formation for the $Ga_xIn_{1-x}As$ material [48], as well as presented a theory on the SILO process [49], where the required number of monolayer pairings within the SPS to maintain strain-balanced conditions has been established. However, such a technique has the disadvantage of a poor size uniformity of the formed wires [50].

The investigation of self-assembled semiconductor nanostructures of InAs grown on InP material has received considerable attention due to their potentiality for optoelectronic devices operating in the wavelength range 1.3 and 1.55 μm. Very much research, up to date, has been conducted on the self-assembled

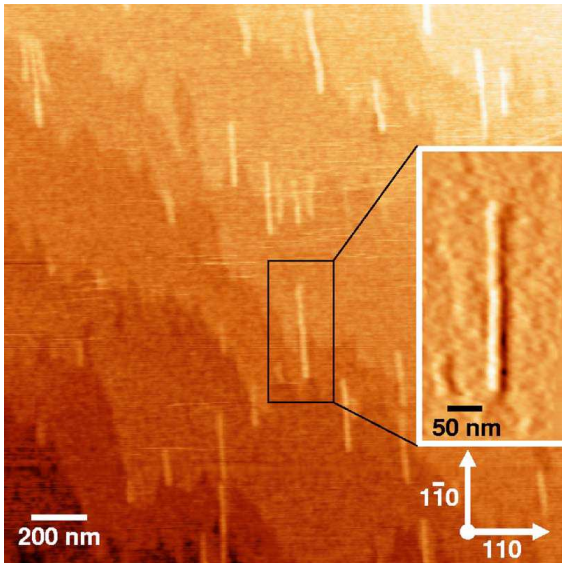

FIG. 1.6: AFM image of the InAs/InP uncovered sample surface. Inset: Zoom over a region containing a long QWR (from Ref. [54]).

InAs/InP QWRs by the experimental group from Instituto de Microelectrónica de Madrid [8–10, 51–54]. They demonstrated that self-assembled QD and QWR structures can be obtained by MBE growth of InAs on InP, above a certain critical thickness [8]. The self-organized InAs/InP QWRs are formed by Stranski-Krastanow growth mode, because of the presence of a substantial difference of 3.2% in lattice mismatch between the wire and the barrier material. The basis of the formation of QWRs rather than dots is an anisotropy in the built-in stress at the InAs/InP(001) interface [9], where the stress is higher in the [110] direction than along [1$\bar{1}$0] (see Fig. 1.5(a) and (b)). In this way, when an InAs monolayer is grown, the distorted In-As bonds contribute to the appearance of a compressive stress in the [110] direction, while no stress appears in the [1$\bar{1}$0] direction. Further deposition of InAs increases the compressive stress equally in both directions, and as a result, the critical amount of stress necessary to cause relaxation is first reached in the [110] direction. Therefore, wires form that are oriented in the [1$\bar{1}$0] direction. The relaxation of the epitaxial stress in the [110] direction amounts to about 20% of the total accumulated stress during growth [9]. QWR formation is characteristic of solid-source MBE growth under group V stabilized (2×4 reconstruction) surface for heteroepitaxial systems with different group V elements. Growing under other surface conditions or other growth procedures (metalorganic chemical vapor deposition, chemical beam epitaxy, and gas-source MBE) results in the usual QD formation. AFM

images of an uncapped InAs/InP QWRs show the variation in wire heights (see Fig. 1.5(b)). A typical zero-field PL spectrum consists of several gaussian contributions that correspond to emission from QWR with a height of a discrete number of monolayers [51]. Following this work, in my thesis I also assumed the rectangular shape of InAs/InP wires as a first approximation for the real shape. Recent cross-sectional scanning tunneling microscopy results [55] shows that InA/InP QWRs are rather triangular-shaped with a gradient of compositions. A further theoretical investigation is needed to study the possible consequences of considering these wires as prisms with a base which is a triangle and of the effect of the composition gradient. For applications of semiconductor devices based on quantum nanostructures a good uniformity in size is desired. Recently, the above mentioned experimental group from Madrid reported results on uniform QWR growth and fabrication of aluminum-free InAs QWR lasers on (001) InP substrates with laser emission at 1.66 μm [10]. Lately, they demonstrated that isolated (single) InAs self-assembled QWRs can be grown in nominally flat InP(001) substrates [54] (see Fig. 1.6). These elongated InAs/InP QWRs appeared randomly distributed with average widths and lengths of 21±3 nm and 185±50 nm, respectively.

1.3 THEORETICAL CONCEPTS

To understand the excitonic properties of a semiconductor QWR, we have to know the electronic band structure. Knowing the initial electron and hole states and corresponding wavefunction, we can calculate the PL peak energy transitions, diamagnetic shift and exciton binding energy within the single-band effective mass approximation including the strain influence on the confinement potentials. Here, I discuss the numerical methods to calculate the band structure, the formation of neutral and charged excitons, the effect of strain on the band structure and the derivation of the main equations in the presence of an external magnetic field.

1.3.1 Band structure of semiconductors. The $\mathbf{k}\cdot\mathbf{p}$ method

For a periodic potential of the semiconductor crystal, the electronic band structure can be derived from the Hamiltonian, which satisfy the symmetry of such a crystal. Numerical methods to find the band structure include the tight binding, the pseudopotential, the orthogonalized and augmented plane wave, Green's function, the cellular methods and $\mathbf{k}\cdot\mathbf{p}$ method, which are detailed described in many textbooks (see, for example, Ref. [56]). Fig. 1.7 shows an example of the InAs band structure which was calculated using the pseudopotential method. The initial idea of all these theories follows the Bloch theorem.

For an electron in a bulk periodic potential

$$V(\mathbf{r}) = V(\mathbf{r} + \mathbf{R}), \tag{1.1}$$

where $\mathbf{R}$ is the lattice vector in the real space. The electron wavefunction satisfies the Schrödinger equation

$$\Big[-\frac{\hbar^2}{2m_0}\nabla^2 + V(\mathbf{r})\Big]\psi(\mathbf{r}) = E(\mathbf{k})\psi(\mathbf{r}), \tag{1.2}$$

where m_0 is the free-electron mass. Because, the Hamiltonian is invariant under the next translation of the lattice vector $\mathbf{r} \rightarrow \mathbf{r} + \mathbf{R}$, the general solution of Eq. (1.2) can be written as

$$\psi_{n\mathbf{k}}(\mathbf{r}) = \exp\left[i\mathbf{k}\cdot\mathbf{r}\right] u_{n\mathbf{k}}(\mathbf{r}), \tag{1.3}$$

where $u_{n\mathbf{k}}(\mathbf{r} + \mathbf{R}) = u_{n\mathbf{k}}(\mathbf{r})$ is a periodic function, E is the energy which is given by $E = E_n(\mathbf{k})$, n refers to the electron band, and $\mathbf{k}$ denotes the wavevector of the electron. The wavefunction $\psi_{n\mathbf{k}}(\mathbf{r})$ is often called the Bloch function. This result is the Bloch theorem.

The $\mathbf{k}\cdot\mathbf{p}$ method is a useful method for studying the band structure of III-V direct band gap semiconductors structures near a particular point $\mathbf{k}_0$ in the Brillouin zone. The $\mathbf{k}\cdot\mathbf{p}$ method was originally introduced by Bardeen [58] and Seitz [59]. Later, Luttinger-Kohn's model for the heavy-hole and light-hole valence bands was reported [60, 61]), and it was extended to the $\mathbf{k}\cdot\mathbf{p}$ theory for the three topmost valence bands including spin-orbit split-off band. 8×8 multiband Hamiltonian, called Kane's model, was devised in late 50s [62], which explicitly take into account mixing between the conduction band and the three valence bands, all doubly degenerate because of their spin counterpart. In the strained semiconductors, the strain dependent part was added to the multiband Hamiltonian by Pikus and Bir [63].

Here, I will discuss the $\mathbf{k}\cdot\mathbf{p}$ method for a single band. The electron wavefunction in the nth band written in terms of $u_{n\mathbf{k}}(\mathbf{r})$ (see Eq. (1.3)) is obtained by solving the following Schrödinger equation

$$\Big[\frac{p^2}{2m_0} + \frac{\hbar}{m_0}\mathbf{k}\cdot\mathbf{p} + V(\mathbf{r})\Big]u_{n\mathbf{k}}(\mathbf{r}) = \Big[E_n(\mathbf{k}) - \frac{\hbar^2k^2}{2m_0}\Big]u_{n\mathbf{k}}(\mathbf{r}). \tag{1.4}$$

Let us consider a single band, as for instance the band edge of the conduction band, labeled with n, while neglecting the coupling to the rest of the bands, $n' \neq n$. Further, we consider $\mathbf{k}_0$=0 around the Γ point, where the minimum of the conduction band and the maximum of the valence band are localized. Then, we assume that the Hamiltonian $H_0 = p^2/2m_0 + V(\mathbf{r})$ for $\mathbf{k}_0$=0 has the solution

$$\Big[\frac{p^2}{2m_0} + V(\mathbf{r})\Big]u_{n0}(\mathbf{r}) = E_n(0)u_{n0}(\mathbf{r}). \tag{1.5}$$

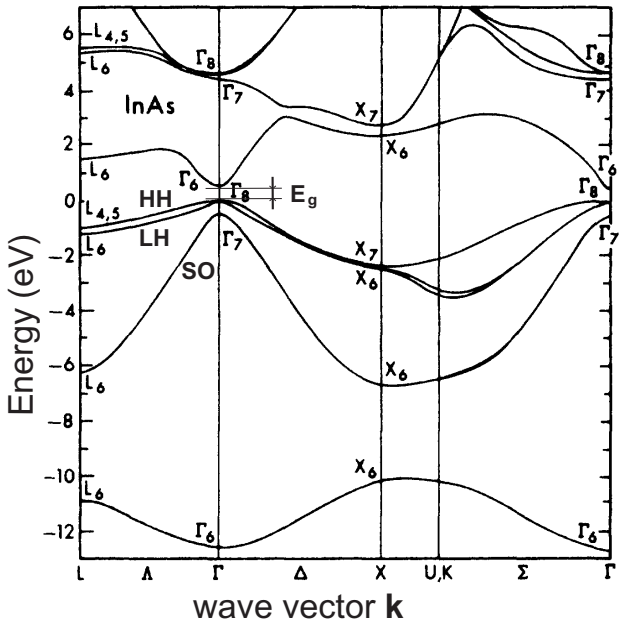

Fig. 1.7: InAs band structure calculated by the pseudopotential method (from Ref. [57]). Near the band edges of the direct band gap E_g the heavy-hole (HH), light-hole (LH), and spin-orbit (SO) split-off bands are shown.

Using perturbation theory we can solve Eq. (1.4). This gives the energy to second order in perturbation

$$E_n(\mathbf{k}) = E_n(0) + \frac{\hbar^2 k^2}{2m_0} + \frac{\hbar^2}{m_0^2} \sum_{n \neq n'} \frac{|\mathbf{k} \cdot \mathbf{p}_{nn'}|^2}{E_n(0) - E_{n'}(0)}, \tag{1.6}$$

and the wavefunction to the first order in perturbation

$$u_{n\mathbf{k}}(\mathbf{r}) = u_{n0}(\mathbf{r}) + \frac{\hbar}{m_0} \sum_{n \neq n'} \Big[\frac{\mathbf{k} \cdot \mathbf{p}_{nn'}}{E_n(0) - E_{n'}(0)} \Big] u_{n0}(\mathbf{r}), \tag{1.7}$$

with the momentum matrix elements

$$\mathbf{p}_{nn'} = \int u^*_{n0}(\mathbf{r}) \mathbf{p} u_{n'0}(\mathbf{r}) \, d\mathbf{r}. \tag{1.8}$$

It should be noted, that the $\mathbf{k}\cdot\mathbf{p}$ method has been efficiently used in studying bulk semiconductors. Moreover, this theory is also very popular and easily transferable to QWs, QWRs and QDs (see, for example, Refs. [64–66]).

1.3.2 Effective mass theory for a single band

The crystal potential of semiconductor materials is complex. However, the effect of the periodic crystal potential on an electron moving inside of it can be approximated by replacing the free-electron mass m_0 with an effective mass m^*. For a non-degenerate band, the wavefunctions and the energies for arbitrary $\mathbf{k}$'s are defined by Eqs. (1.6) and (1.7). For small values of $\mathbf{k}$

$$E_n(\mathbf{k}) = E_n(0) + \frac{\hbar^2 k^2}{2m^*}, \tag{1.9}$$

where the effective mass m^* is

$$\frac{1}{m^*} = \frac{1}{m_0} + \frac{2}{m_0^2 k^2} \sum_{n \neq n'} \frac{|\mathbf{k} \cdot \mathbf{p}_{nn'}|^2}{E_n(0) - E_{n'}(0)}. \tag{1.10}$$

In general, the effective mass is a tensor and its components are related to the band structure as

$$\frac{1}{m^*_{ij}} = \left. \frac{\partial^2 E}{\hbar^2 \partial k_i \partial k_j} \right|_{k=0}, \tag{1.11}$$

and it can be empirically obtained as a fitting parameter from the experimental measurements.

The most important result of the effective mass theory for a single band is that the single particle solution of the Schrödinger equation with an external potential $U(\mathbf{r})$ can be obtained as follows

$$\left[\frac{p^2}{2m^*} + U(\mathbf{r}) \right] \Psi(\mathbf{r}) = E\Psi(\mathbf{r}), \tag{1.12}$$

where the potential $U(\mathbf{r})$ can be an impurity potential in bulk material, or in the case of semiconductor nanostructures, a QW (QWR or QD) confinement potential for the electron (hole), and E and $\Psi(\mathbf{r})$ are the energy and wavefunction of the corresponding particle, respectively. Note, that the effective mass equation (1.12) contains only the external potential $U(\mathbf{r})$, since the effective mass determines the periodic crystal potential $V(\mathbf{r})$.

The single-band effective approximation may not be sufficient for very narrow nanoscale systems, because in this case explicit coupling between degenerate bands needs to be treated as a perturbation, which can be included, for example, using the multi-band $\mathbf{k}\cdot\mathbf{p}$ method, the tight-binding method and the pseudo-potential method. However, the single-band effective mass method has been widely used for the description of the optical properties close to the zone center, where $k \to 0$. Through this thesis we deal with the optical properties near the fundamental band-gap energy for the InAs/InP and GaAs/AlGaAs QWRs. Therefore, the single-band effective mass theory will be used to obtain the electron and hole wavefunctions and energies, as well as to study the exciton properties in the QWRs and in the related low-dimensional systems.

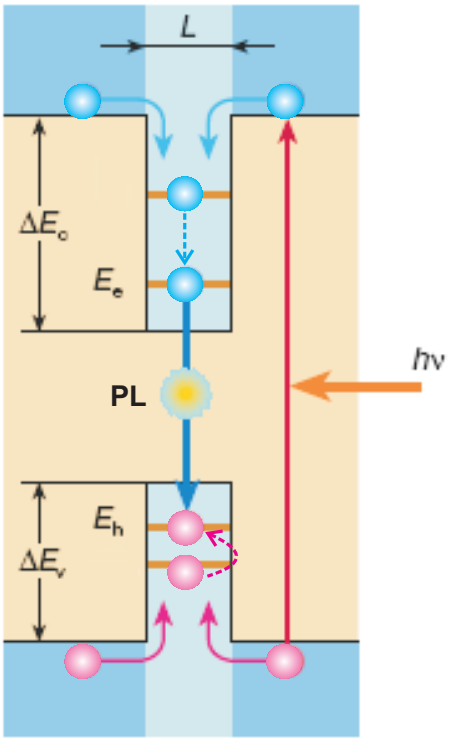

Fig. 1.8: Schematics showing the non-resonant generation of excitons in QW. $\hbar\nu$ is the energy of the phonon excitation, L denotes the QW width, PL is the photoluminescence energy, ΔE_c and ΔE_v are the conduction and valence band offsets, respectively.

1.3.3 Excitons

The simplest excitation in a semiconductor occurs when an electron from the valence band jumps across the band gap into the conduction band. In this case an empty positively charged state is created within the valence band, named a hole. Having charges of the opposite sign, the electron and hole are bound by the Coulomb interaction between them. This bound electron-hole state is known as an exciton.

Because the hole mass is generally much larger than the electron mass, the two-body system is similar to a hydrogen atom. The exciton moves, as a free particle with the mass $M{=}m_e^*{+}m_h^*$, where m_e^* and m_h^* are the effective mass of the electron and the hole, respectively. The relative motion of the exciton has mass $\mu{=}m_e m_h/M$. Thus, the binding energy of the exciton (X) in bulk

becomes

$$E_X = -\frac{\mu e^4}{2\epsilon^2\hbar^2} = \frac{e^2}{2\epsilon a_{ex}}, \tag{1.13}$$

where $a_{ex} = \epsilon\hbar^2/\mu e^2$ is the effective Bohr radius, e is the free-electron charge, and ϵ is the dielectric constant. Using the typical values for bulk GaAs, one can obtain the exciton binding energy of 4.2 meV and the Bohr radius of 150 Å.

When photons of energy $\hbar\nu$ comparable to the band gap of the barrier material in the semiconductor nanostructure are absorbed by the electrons they will leave behind a hole in the valence band, and in this way creating an electron-hole pair inside the quantum nanostructure. The schematics representing the non-resonant formation of 2D exciton in QW is illustrated in Fig. 1.8, which is similar to the formation of a 1D exciton in QWR or 0D exciton in QD. Whereas in bulk, the total energy of the exciton is simply the energy of the bang gap plus the exciton binding energy (since the Coulomb potential energy E_X is negative, the excitonic levels will be below the conduction band in bulk), in a nanostructure there are additional components due to the electron and hole confinement

$$E_{tot} = E_g + E_X(\text{bulk}) \quad E_{tot} = E_g + E_e + E_h + E_X(\text{nanostructure}). \tag{1.14}$$

The total energy is a function of the specific quantum nanostructure because of the size dependence of the confinement energy. Besides, the exciton binding energy is also dependent on the dimensions of such structures because both the electron and hole bound by the Coulomb interaction in addition are also confined by the conduction and valence band offset ΔE_c and ΔE_v, respectively (see Fig. 1.8). Moreover, it should be stressed that the decreased structure dimensionality increases the exciton binding energy. Thus, excitons are more stable in semiconductor nanostructures than in bulk. Therefore, exciton recombination is an important feature of low temperature PL in quantum structures. Knowing the exciton binding energy and the particles confinement energies, one can calculate the total exciton energy, which is equal to the PL energy (see Fig. 1.8).

When an electron is bound by the Coulomb interaction to an exciton a negatively charged exciton (X^-) is formed. A hole and an neutral exciton bound together form a positively charged exciton (X^+). They are also often called *trions* or exciton complexes. Enhancement of the binding energy of trions is expected in quantum confined systems of low dimensionality. The stability of charged excitons in bulk was proven theoretically by Lampert [67] in late fifties, but only recently they were experimentally observed in QWs [68], QWRs [69], and QDs [70].

In the present thesis the main focus is on excitons in QWRs, and some results on the excitonic properties in QWs and QDs will be presented. Moreover,

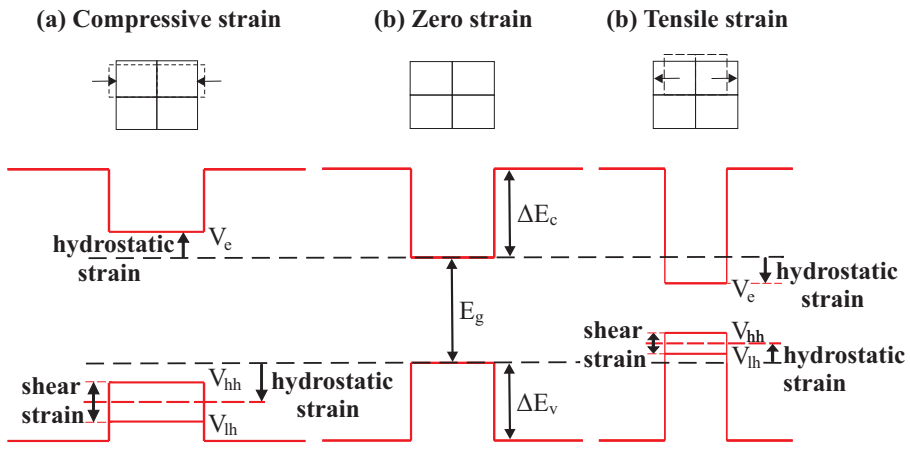

Fig. 1.9: Band-edge (red) profile for (a) a compressive strained, (b) an unstrained and (c) a tensile strained QW.

the stability of the charged excitons in V-shaped and self-assembled QWRs is theoretically investigated.

1.3.4 Strain effects on the band structure

When a crystal is under a uniform deformation, it may preserve the periodic property such that the Bloch theorem may still be applicable. The modulation part of the Bloch function remains periodic, with a period equal to that of the new elementary cell, since the elementary cell is also deformed. Such deformation is introduced in the strained 6×6 Pikus-Bir Hamiltonian which is developed for a strained semiconductor, as was already mentioned in section 1.3.1 of this chapter.

For a quantum nanostructure, the strain modifies the band structure including the conduction and the valence edge energies which are among the most important parameters characterizing them. We assume that the conduction band is decoupled from the valence band. The edge of the conduction band responds only to the hydrostatic strain

$$V_e = \Delta E_c + a_c \varepsilon_{hyd}, \tag{1.15}$$

where ΔE_c is the unstrained conduction band offset, a_c is the hydrostatic deformation potential for the conduction band, $\varepsilon_{hyd} = \varepsilon_{xx} + \varepsilon_{yy} + \varepsilon_{zz}$ denotes the hydrostatic strain, and ε_{xx}, ε_{xx}, and ε_{zz} are the components of the strain tensor ε. For most III-V semiconductors, the split-off bands are several hundred meV below the heavy- and light-hole bands. Since the energy range of interest

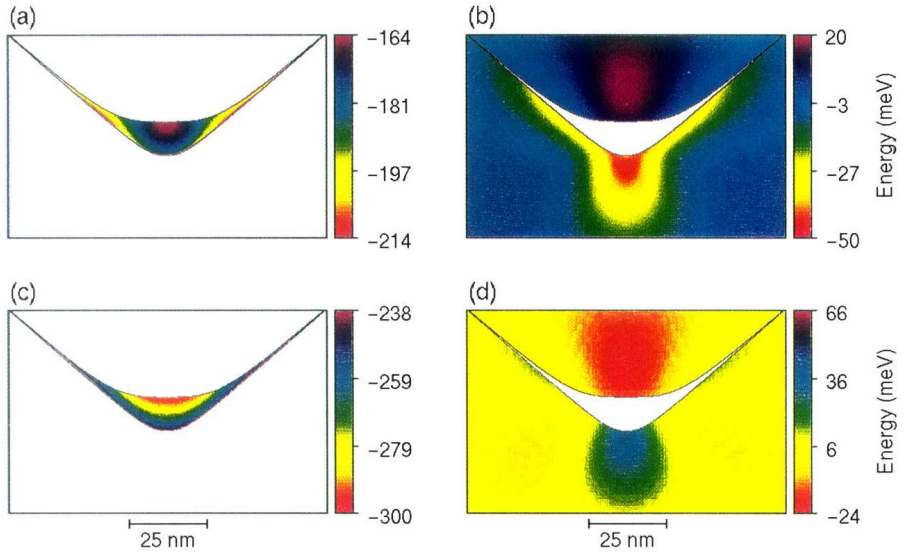

FIG. 1.10: Confinement potentials for hole in the wire (a), and in the barrier (b) and electron in the wire (c), and in the barrier (d) for a V-shaped InGaAs/AlGaAs QWR (from Ref. [72]).

is only several tens of meV, it is usual to assume that the split-off bands can be ignored. In this case the band structure of the heavy- and light-hole bands is approximately described by the 4×4 Hamiltonian [71]

$$H = \begin{bmatrix} P+Q & S & 0 & -R \\ S^{\dagger} & P-Q & R & 0 \\ 0 & R^{\dagger} & P+Q & S^{\dagger} \\ -R^{\dagger} & 0 & S & P-Q \end{bmatrix}. \tag{1.16}$$

where the matrix elements of this Hamiltonian are given using the deformation potentials a_v, b and d of the valence band

$$P = a_v(\varepsilon_{xx} + \varepsilon_{yy} + \varepsilon_{zz}), \tag{1.17}$$

$$Q = \frac{b}{2}(\varepsilon_{xx} + \varepsilon_{yy} - 2\varepsilon_{zz}), \tag{1.18}$$

$$R = -\frac{\sqrt{3}}{2}b(\varepsilon_{xx} - \varepsilon_{yy}) + id\varepsilon_{xy}, \tag{1.19}$$

$$S = -d(\varepsilon_{zx} - i\varepsilon_{yz}). \tag{1.20}$$

For the 4×4 Hamiltonian the solutions, that represent the heavy-hole and light-hole valence band edges, are simply

$$V_{hh} = \Delta E_v + P + sgn(Q)\sqrt{Q^2 + RR^\dagger + SS^\dagger}, \tag{1.21}$$

$$V_{lh} = \Delta E_v + P - sgn(Q)\sqrt{Q^2 + RR^\dagger + SS^\dagger}, \tag{1.22}$$

where ΔE_v is the unstrained part due to the valence band offset between the quantum confined structure and the barrier material. Note that it is important to include the sign factor $sgn(Q)$ in front of the square root, because Q could be either negative (compressive strain) or positive (tensile strain) while the quare root is conventionally taken as positive.

Fig. 1.9 illustrates, that in a QW in the presence of compressive (tensile) strain the bottom of the conduction band is shifted up (down) by the value of the hydrostatic stain. In the case of the holes the situation is more complicated. The edge of the valence band for the heavy-hole and light-hole is shifted up or down depending on the tensile or compressive strain (see Eqs. (1.17),(1.21) and (1.22)), but also shifted by a value which depends on the shear strain (see Eqs. (1.18),(1.21) and (1.22)), as shown in Fig. 1.9. However, these results can be obtained for $\mathbf{k}$=0 when excluding the off-diagonal elements R and S in the strain Hamiltonain (1.16). As an example, in Fig. 1.10 the results of the confinement potential for the hole and electron in crescent-shaped QWR are compared, when the strain Hamiltonian includes all matrix elements.

In my thesis I will calculate the strained confinement potentials for the electron and holes in self-assembled rectangular InAs/InP QWRs. In order to derive the strain components ε_{xx}, ε_{yy} and ε_{zz} of the QWR within the rectangular cross section we adapted the method given by Downes [73].

1.3.5 Presence of a magnetic field

To construct the Hamiltonian in the presence of a magnetic field, described by a vector potential $\mathbf{A}$, the momentum of any particle of electrical charge q, has to be replaced by the expression $\mathbf{p} - \frac{q}{c}\mathbf{A}$, so that the unrelativistic Hamiltonian becomes

$$H = \frac{1}{2m^*}\left(\mathbf{p} - \frac{q}{c}\mathbf{A}\right)^2 + U(\mathbf{r}), \tag{1.23}$$

where m^* is the effective mass of the particle, and $U(\mathbf{r})$ any other potential due to non-magnetic forces. This classical expression may be translated into quantum mechanics replacing the momentum $\mathbf{p}$ by the operator $-i\hbar\nabla$. Further, taking into account that in quantum confined systems the effective mass of a

particle m^* is in general spatial dependent, it can be simplified to

$$H = -\frac{\hbar^2}{2}\nabla\frac{1}{m^*}\nabla + \frac{qi\hbar}{2c}\left(\mathrm{div}\mathbf{A} + \frac{1}{m^*}\mathbf{A}\cdot\nabla + \mathbf{A}\cdot\nabla\frac{1}{m^*}\right) + \frac{q^2}{2m^*c^2}\mathbf{A}^2 + U(\mathbf{r}). \quad (1.24)$$

Depending on the magnetic field orientation relative to the quantum structure, several cases can be realized where the magnetic field has an influence on the energy spectrum and the particle wavefunction. When a magnetic field is applied along a certain direction, the gauge is chosen such that is simplifies the problem as much as possible. For instance, for in-plane magnetic field in a QW (*when neglecting the Coulomb interaction*) the following nonsymmetric gauge can be chosen $\mathbf{A}{=}{-}zB\hat{y}$, while considering the case of a magnetic field oriented along the z-direction, that is normal to the QW, it is convenient to choose the vector potential as $\mathbf{A}{=}{-}yB\hat{x}$ [74]. In a QWR, where the particles are free to move in the longitudinal direction, taken here as z-axis, and confined by lateral confinement in the xy-plane, a more useful gauge for a magnetic field $\mathbf{B} = B\hat{y}$ is a gauge which preserves translational symmetry along the wire axis, namely $\mathbf{A} = -xB\hat{z}$ [75], and for magnetic field which is applied perpendicular to the wire plane one can use the symmetric gauge $\mathbf{A} = \mathbf{B}\times\mathbf{r}/2$ [76]. The inclusion of the magnetic field leads to additional linear and quadratic terms with respect to B_i, r_i and ∇_i ($i = x, y$ and z) in the kinetic part, which differ for the different orientation of external field $\mathbf{B}$.

In this thesis I will study the magnetic field dependence of the excitonic states in semiconductor nanostructures. In particular, I will calculate the diamagnetic shift of exciton energy for QWs and QWRs in the presence of parallel and perpendicular magnetic fields, and for QDs in magnetic fields of varying orientation.

1.4 THEORETICAL RESULTS ON QUANTUM WIRES

In section 1.2 I presented a review on major advances achieved over the past years in the field of fabrication of semiconductor QWRs. In this section, I will give a brief overview of the theoretical studies that have been performed to investigate the electronic and optical properties in semiconductor QWRs.

Parallel to the effort concerning the fabrication and characterization of embedded QWRs, their theoretical modeling was developed in order to enable the prediction of the physical properties of such structures and to enable a deeper understanding of experimental results. In 1980, it was first time predicted by Sakaki [77] that the electron mobility is drastically enhanced at low temperature in QWR structures. In this work, the transport properties of the electrons confined in the ultrafine GaAs wire structures were studied theoretically. A T-shaped 1D QWR was proposed by Chang *et al.* [26] in 1985. They presented for

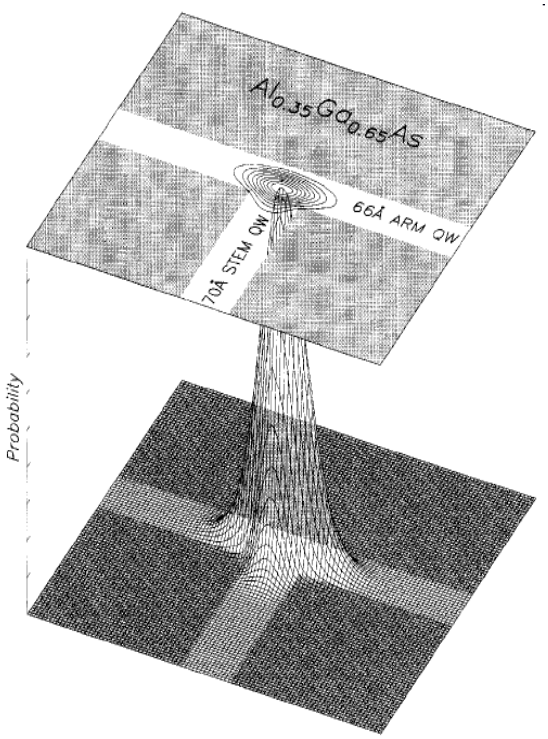

Fig. 1.11: Schematic cross-section of the GaAs/AlGaAs QWR, showing the center-of mass wavefunction of an exciton trapped at the T-intersection of the stem and arm QWs (from Ref. [88]).

the first time the calculations of the lowest conduction band energy and exciton binding energy for such QWR structure. Following these two pioneering works the electrical transport, the hydrogenic impurity states, the electron-phonon interactions in QWRs have been discussed in many papers [78–82].

The electronic and optical properties in semiconductor QWRs of the different *shapes* were investigated using the tight-binding [83] and the effective bond-orbital [84] models as well as the parabolic band approximation [85, 86]. Early work for the *rectangular-shaped* QWRs by Degani *et al.* [87] used model calculations to describe the properties of excitons confined to unstrained QWRs. The excitons in the *T-shaped* GaAs/AlGaAs QWRs were investigated by Hasen *et al.* [88] using the fixed-node Monte Carlo method (see Fig. 1.11). In this work metamorphosis of a QWR into QDs was reported. At low temperatures a transition from the broad continuous PL to an energetically sharp and spatially localized intense set of emission peaks was observed indicating that QWR acts like a sparse set of QDs. A number of studies concerning valence-band mixing

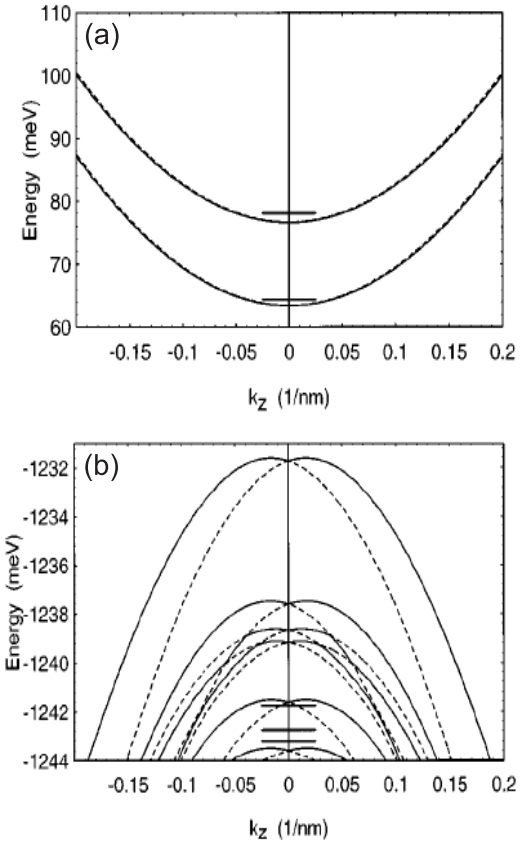

FIG. 1.12: (a) Lowest four 1D conduction bands and (b) topmost twelve 1D valence bands in the InGaAs/AlGaAs QWR (alternating solid and dashed). The energy zero is E_c of unstrained bulk InGaAs. The solid markers indicate the quantum levels calculated by a parabolic band approximation (from Ref. [92]).

effects in the *T-shaped*, the *V-shaped* and the *rectangular-shaped* QWRs have been carried out [89–91]. Stier *et al.* [92] calculated numerically the 1D band structure of the *V-shaped* InGaAs/AlGaAs single QWR using eight-band $\mathbf{k}\cdot\mathbf{p}$ theory, as shown in Fig. 1.12. They found a dominant impact of a strain-induced piezoelectricity on the band structure, a spin splitting of the valence bands and a strong conduction band nonparabolicity.

An applied uniform magnetic field is one of the main probes used for studying the physical properties of nanostructures. The application of a magnetic field modifies the symmetry of the electron motion and the nature of the electron wavefunction. The magnetic properties of QWRs have been treated by

many authors. Notomi *et al.* [93] have studied the dependence of exciton binding energy on the magnetic field in the T-shaped QWRs using a six-band Luttinger models that incorporates the conduction band nonparabolicity and valence band coupling. Kyrychenko *et al.* [94] performed calculations of the valence band states in the diluted semiconductor QWR structures. They showed that it is possible to control the relative contribution of the light- and the heavy-hole components of the total wavefunction of the holes by changing an external magnetic field. Bryant *et al.* [95] calculated the diamagnetic shift in the T-shaped QWRs with perturbation theory and lately Madureira *et al.* [75] have investigated the magnetoexciton states and optical-absorption spectrum in such QWRs. They found an enhancement of the exciton binding energy with increasing magnetic field, as was expected from experimental data. Recently, Silva *et al.* [96] have studied the excitonic behavior under the applied magnetic field of SiGe cylindrical quantum wires embedded in a silicon matrix. They found that the exciton energies in type-I wires (the electron and hole are both confined in the QWR) are weakly affected by the magnetic field, while such a field alters drastically the excitonic behavior for type-II wires (one charge carrier is localized inside the wire, and the other one in the barrier material), since the ringlike shape of electron states is responsible for the occurrence of the Aharonov-Bohm effect.

1.5 OVERVIEW OF THE THESIS

In this thesis, I will investigate the excitonic properties in semiconductor nanostructures. However, the main contribution of this work is the study of excitons in QWRs.

1.5.1 Model Hamiltonian

To calculate the excitonic states in a QWR we use the single-band effective mass approximation, where the mass mismatch between the wire and the barrier, the effect of strain on the confinement potentials of the electron and hole, the presence of an external magnetic field, conduction band nonparabolicity, and the Coulomb interaction between the electron and the hole can be included. We assumed further approximations. Along the wire growth direction (here taken to be the z-direction) there is no confinement for the particles in the wires, while in the xy-plane the electron and hole are strongly confined. For this reason we separate the z-motion from the xy-motion. We also treat the Coulomb interaction term as a perturbation, so that we can separate the electron and hole wavefunctions. Next, we introduce the relative coordinates $z = z_e - z_h$ and the center-of mass coordinates $Z = (m_e^* z_e + m_h^* z_h)/M$ and we calculate the single electron and hole states in the xy-plane, where $m_{e(h)}^*$ is the effective mass

Table 1.1: Input material parameters for InAs/InP and GaAs/$Al_{0.4}Ga_{0.6}As$ QWR's used in the calculations: lattice constant a_0, band gap E_g, electron mass m_e, Luttinger parameters γ_1 and γ_1, nonparabolicity parameters α, the hydrostatic deformation potential for the conduction band a_c, the deformation potentials of the valence band a_v, b and d, strain coefficients C_{11} and C_{12}, and dielectric constant ε.

Parameter	InAs	InP	GaAs	$Al_{0.4}Ga_{0.6}As$
a_0 (Å)	6.058	5.869	- -	- -
E_g (eV)	0.417	1.424	1.519	2.018
m_e (m_0)	0.023	0.077	0.067	0.1
γ_1	20	5.08	6.98	5.69
γ_2	8.5	1.6	2.06	1.57
α (eV^{-1})	1.4	- -	0.64	- -
a_c (eV)	-5.08	- -	- -	- -
a_v (eV)	1	- -	- -	- -
b (eV)	-1.8	- -	- -	- -
d (eV)	-3.6	- -	- -	- -
C_{11} (GPa)	83.29	- -	- -	- -
C_{12} (GPa)	45.26	- -	- -	- -
ε	15.15	12.5	12.9	11.76

of the electron (hole). The single particle 2D Hamiltonian is

$$H_{e(h)} = \left(\mathbf{p}_{e(h)} - \frac{q}{c}\mathbf{A}\right) \frac{1}{2m^*_{e(h)}(x,y)} \left(\mathbf{p}_{e(h)} - \frac{q}{c}\mathbf{A}\right) + V_{ec(vh)}(x,y), \quad (1.25)$$

where $\mathbf{A}$ is the vector potential of the magnetic field, and $V_{ec(vh)}(x,y)$ denotes the confinement potential of the electron (hole) due to the conduction (valence) band offset and strain. To obtain the exciton binding energy in the QWR we solve an effective 1D Schrödinger equation for the motion in the z-direction

$$\left[-\frac{\hbar^2}{2\mu_z}\nabla_z^2 - \int dx_e dy_e dx_h dy_h |\Psi_e|^2 |\Psi_h|^2 \frac{e^2}{\varepsilon|\mathbf{r_e} - \mathbf{r_h}|}\right] \varphi(z) = E_X \varphi(z), \quad (1.26)$$

where μ_z denotes the reduced mass of the exciton along the QWR growth direction, $\Psi_{e(h)}$ is the electron (hole) wavefunction in the xy-plane, E_X is the exciton binding energy, and ε is the dielectric constant taken as the average value of the wire and the barrier. Thus we averaged the 3D Schrödinger equation with the Hamiltonian (1.25) over the single particle electron and hole wavefunctions in the confinement directions x and y. This is an approximation which is valid as long as the confinement energy is much larger than the Coulomb exciton energy, as is the case in our study. We consider both heavy-hole and light-hole

states. The mass of the heavy-hole and the light-hole is taken the same in each direction

$$\frac{m_0}{m^*_{hh}} = \gamma_1 - 2\gamma_2, \tag{1.27}$$

$$\frac{m_0}{m^*_{lh}} = \gamma_1 + 2\gamma_2, \tag{1.28}$$

where m_0 is the vacuum electron mass, and γ_1 and γ_1 are Luttinger parameters. We include the effect of band nonparabolicity in our calculations by using an energy dependent electron mass

$$m^*_{nonp.e} = m^*_e(1 + \alpha E), \tag{1.29}$$

where $m_{nonp.e}$ is the nonparabolic electron mass, α is the nonparabolicity parameter, and E is the energy of the electron obtained by solving the single particle Schrödinger equation using the electron bulk mass m^*_e.

The simulations for InAs/InP and GaAs/AlGaAs QWRs in the presence of a magnetic field are performed using two independent numerical procedures: one is based on a two-dimensional finite difference technique with uniform grid space, while the other relies on the finite element method on a variable size grid. The input parameters used for our calculations are presented in Table 1.1.

1.5.2 Organization of the thesis

The thesis is organized in the following way:

In chapter 2, I present the results on the charge confinement in InAs/InP self-assembled QWRs. In our calculations, we used the adiabatic approximation within the effective-mass theory to calculate the exciton energy of an electron-hole pair in a rectangular QWR. Magneto-photoluminescence experiments and our theoretical calculations were combined to study the electron wavefunction spill-over in InAs/InP QWRs.

In the third chapter, I consider V-shaped GaAs/AlGaAs QWRs and self-assembled rectangular InAs/InP QWRs in the presence of an external magnetic field. I calculate the diamagnetic shift of the exciton energy for both V-shaped and self-assembled QWRs when the magnetic field is along different directions of the QWR. I analyze different sizes and shapes of the QWRs and compare them with the magneto-photoluminescence experimental measurements.

In the fourth chapter using the single-band effective mass approximation but including strain effects and conduction band nonparabolicity, I investigate the charge confinement in InAs/InP QW and self-assembled InAs/InP QWRs. I study the exciton energy shift of QWR and QW with a local thickness fluctuation in magnetic fields up to 50 T and compare theoretical and experimental data.

In the fifth chapter, I report the results on the stability of charged excitons in V-shaped GaAs/AlGaAs QWRs and self-assembled rectangular InAs/InP QWRs. I study the binding energies of negative and positive trions in such wires. The calculations are performed within the single-band effective mass approximation including the true geometrical shape of the wires, as well as the mass mismatch between the wire and the barrier, and the influence of strain on the particle confinement potentials.

Chapter 6 is devoted to the study of the dependence of the single-particle energies and the behavior of the electron and hole densities on the distance between two vertically and two horizontally coupled InAs/InP quantum wires, the Coulomb interaction energy, and the exciton energy on the small distance between two vertically coupled InAs/InP quantum wires. I also calculate the PL transition energies in these structures as a function of the height of the wires and compare them with available experimental data in order to deduce the height of the coupled wires.

In the seventh chapter, I study the energy spectrum of single excitons in the presence of an applied magnetic field for unstrained GaAs/AlGaAs QDs. The real experimental 3D shape of the dot with a QW on the top and asymmetrical AlGaAs barriers is considered. I study the exciton energy shift for the ground and the excited states of the QD in magnetic fields up to 50 T of varying orientation.

2

Electron wavefunction spill-over in self-assembled InAs/InP quantum wires

2.1 INTRODUCTION

Under certain growth conditions, uniform arrays of selfassembled quantum wires can be obtained by solid source MBE deposition of InAs on an InP substrate [8, 9, 51, 97]. InAs QWRs embedded in an InP matrix are a type-I system, and act to confine the electron and hole to the InAs wires [98]. They are promising candidates for optical applications at the telecommunication wavelengths (1.3 and 1.55 μm), although they generally show a broad PL spectrum consisting of several peaks that are attributed to QWRs of heights which differ by a discrete number of monolayers [51]. Here, information on the confinement of excitons in such wires is obtained by careful analysis of the energy shift of the PL peaks in high magnetic fields ($\leq$50 T) and by a strain dependent effective mass approximation [71, 73, 99]. Although both conduction and valence band offsets are large (0.657 and 0.35 eV, respectively) and thus electrons and holes are expected to be strongly confined to the InAs wire, we find that for very flat wires a large fraction of the electron wavefunction is located in the InP barrier material. In this regime, the exciton wavefunction extent is inversely related to the wire height. Such a wavefunction penetration into the barrier material has already been predicted and observed for $In_{0.1}Ga_{0.9}As$/GaAs quantum wells [100], T- and V-shaped GaAs QWRs [34, 86, 95, 101], Ge/Si quantum dots [102], and other nanostructures, where the charge confinement is relatively

weak in the absence of a magnetic field [103, 104]: much weaker than in the InAs/InP QWRs under study. In these systems, the wavefunction spill-over was investigated mainly theoretically [95, 101, 104] or by PL in zero field [102] or low magnetic fields up to 12 T [86, 100]. A detailed overview of exciton confinement in GaAs QWRs is given by Akiyama [34]. In addition, the dependence of the wavefunction penetration on the dimensionality of the system was studied and shows that, due to the lower dimensionality of the QWR, the confinement energy is increased and thus the wavefunction penetration into the barrier is larger as compared to a QW with similar band offsets [95, 103, 105]. Three methods of fabricating QWRs, other than the self-assembly process mentioned here, have been applied to the In(Ga)As/InP system. The first is the deposition of an unstrained $In_{0.53}Ga_{0.47}As$/InP multi-QW on a vicinal (001) InP substrate, which leads to very thin quasi-1D filaments [106] in which exciton wavefunction penetration is expected due to the monolayer thickness [99], but to date, has not been quantitatively studied. A second method is based on the deposition of a lithographically patterned stressor on top of an InGaAs/InP QW [107], and the third method relied on the prepatterning of the substrate [108]. In this way, large QWRs have been created for which, consequently, no wavefunction penetration is expected. In the self-assembled InAs/InP system (both wires and dots), a wavefunction spill-over into the barrier material was not expected and thus had not been considered to date [51, 109, 110], but it has important consequences for applications. To improve the performance of lasers based on InAs/InP wire structures, the growth procedure should be adjusted to allow higher wires to develop uniformly in which there is a reduced wavefunction spill-over, an enhanced electron-hole overlap and an improved carrier confinement.

2.2 GROWTH OF QUANTUM WIRES

We report on the investigation of three different QWR samples. The first sample (A) was fabricated by atomic layer molecular beam epitaxy. A 200 nm thick InP buffer layer was grown on top of an InP substrate at 430°C. The temperature was kept constant during the deposition of 2.5 monolayer (ML) of InAs. The sample was subsequently annealed for 2 min at 530°C. For this sample, it was during the annealing that the QWRs formed. Afterwards, the temperature was lowered again to the original value for deposition of the 50 nm thick InP capping layer. For the second sample (B), the growth was similar but at different temperatures. The deposition temperature was 430°C and the annealing temperature was 560°C. In sample C, InAs was grown at 515°C. In this sample, due to the elevated temperature, QWRs were formed during growth after 1.7 ML of InAs was deposited, without any further annealing step. Immediately after wire formation, the InAs growth was interrupted and a 20

nm InP cap layer was grown at the same temperature. In all samples, the InAs QWRs are oriented along the $[1\bar{1}0]$ direction with a height that is an order of magnitude thinner than the width [9, 51] (see the inset of Fig. 2.1).

An estimate of the size and shape of the wire can be made by analyzing AFM images on similar but uncapped structures. These show a wire period of 24 nm, a wire width of 18 nm, and an average vertical peakto- valley amplitude of 1.4 nm [9, 51]. The typical length exceeds 1 μm. Since the height is much smaller than the width, the wires can be regarded as ribbons. While the width is more or less constant, the height varies substantially between 0.6 and 2.0 nm for different wires. Therefore, a broad luminescence spectrum is expected, and the different PL peaks in samples B and C (see Fig. 2.1) can be attributed to wires of different heights of a discrete number of monolayers [51]. Such a monolayer splitting was also recently observed in InAs/GaAs (Ref. [111]) and InAs/InP QDs [109]. It is found that the geometric characteristics of the uncapped wires are independent of variations in growth conditions such as those of the three samples studied. Due to the capping process, however, a temperature dependent As/P exchange occurs at the surface [97]. In sample C, which has the highest growth temperature of the InP cap layer, this exchange process is most pronounced, reducing the amount of InAs incorporated in the wires. Therefore, the smallest wires are expected for sample C, and from its large zero-field PL energy, a smaller wire height is indeed inferred. The fact that only two pronounced peaks are present reflects a reduced distribution in the wire height.

2.3 EXPERIMENTAL AND THEORETICAL METHOD

The PL experiments were carried out at 4.2 K in a helium bath cryostat that is placed in the bore of a pulsed magnet. Excitation light, provided by a Nd:yttrium aluminum garnet laser operating at 532 nm, was focused into a 200 μm core optical fiber. At the cryostat end, six detection fibers placed around the excitation fiber collected the luminescence from the sample, which was then dispersed in a 0.3 m spectrometer coupled to an InGaAs diode array detector. The magnetic field can be applied parallel to the growth direction ($\mathbf{B}//[011]$), parallel to the wires ($\mathbf{B}//[1\bar{1}0]$) or perpendicular to both ($\mathbf{B}//[110]$, see the inset of Fig. 2.1). In the latter two cases, the sample is mounted vertically and a mirror is placed at 45° to increase the luminescence intensity that is picked up by the fibers. In about 20 ms field pulse, up to 4 spectra were taken at different values of the field, each with a 0.5 ms photon integration time and a field variation that is $\pm 3\%$ at most.

Applying a magnetic field provides information on the exciton confinement in the plane perpendicular to B. The InAs/InP QWRs are clearly not cylindrically symmetric in this plane for any direction of the field. In such a case,

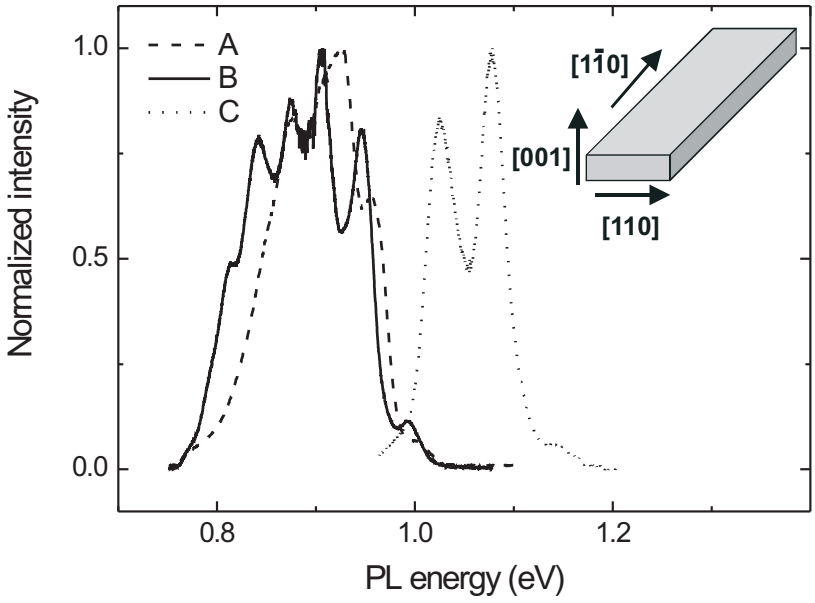

FIG. 2.1: Zero-field spectra for the samples A (dashed), B (solid), and C (dotted). The inset shows a schematic representation of the wire with the different crystallographic directions.

the diamagnetic energy shift is determined mainly by the direction of strongest confinement in the plane perpendicular to B [112]. For example, with $\mathbf{B}$ along [001] the confinement in the direction of the width is probed (see the inset of Fig. 2.1). And if $\mathbf{B}$ is applied along the width, i.e., along [110], information about the wire height can be gained. If one of the charge carriers of the exciton (either electron or hole) has a very different extent than the other, the diamagnetic shift will, in general, be determined by the particle with the largest extent.

The diamagnetic energy shift generally has a parabolic field dependence at low magnetic fields that is given by $\Delta E = e^2 \langle \rho^2 \rangle B^2/8\mu$, where $\langle \rho^2 \rangle$ and μ are the exciton radius and effective mass, respectively, in the plane perpendicular to the field. For a noncylindrically symmetric system, $\langle \rho^2 \rangle^{1/2}$ should be regarded as an averaged radius in the direction of the strongest confinement only, as mentioned above. For sufficiently high fields, when the magnetic length becomes smaller than the spatial confinement, the magnetic confinement will dominate and a linear behavior is observed parallel to the lowest Landau level: $\Delta E \propto \hbar e B/2\mu$. Combining these formulas into a single function, with the requirement that this function and its derivative is continuous, generates a unique

set of values for $\langle\rho^2\rangle^{1/2}$ and μ [113]. Other methods that combine the low and high field limit more gradually, such as that presented by Janssens *et al.* [114] and a description via Fock-Darwin states [115] are found to produce similar $\langle\rho^2\rangle^{1/2}$ and μ. However, when the high field limit is not entirely reached, all three models fail, even when a deviation from the parabolic field dependence is already clearly observed; i.e., when the ΔE is plotted as a function of B^2. Due to the small heights of the InAs/InP QWRs, the crossover between parabolic and linear field dependence occurs at high magnetic field when B is perpendicular to [001]. This results in only a small deviation from parabolic behavior in the 0-50 T range. Therefore, in this work, the aforementioned set of expressions from Ref. [113] are used only to detect the onset of this "crossover field" regime rather than to quantify the exciton radius and mass. We find that, compared to the two other models, this model is the most sensitive to the deviation from parabolic behavior, and gives a crossover field that corresponds well with that seen in plots of ΔE versus B^2. Since the crossover field regime is inversely proportional to the exciton radius and independent of the exciton effective mass, the field at which this deviation is detected directly provides qualitative information on the exciton extent. Quantitatively, however, the uncertainty is due to the small size of the deviation from the parabolic field behavior and would be improved if higher magnetic fields could be applied.

In our calculations, we used the adiabatic approximation within the effective mass theory to calculate the exciton energy of an electron-hole pair in a rectangular QWR. The conduction and valence band offsets are taken to be E_c=0.657 eV and E_v=0.35 eV [98]. To include the strain, which shifts the electron and hole confinement potentials, we used the expressions for the strain tensor of Ref. [73]. The edge of the conduction band is shifted by the hydrostatic strain

$$E_{ce} = E_{c0} + a_c\varepsilon_{hyd}, \tag{2.1}$$

where a_c denotes the hydrostatic deformation potential for the conduction band. The heavy hole and light hole band edges are calculated from the Pikus-Bir Hamiltonian [71]

$$E_{vhh} = E_v + P + sgn(Q)\sqrt{Q^2 + RR^\dagger + SS^\dagger}, \tag{2.2}$$

$$E_{vlh} = E_v + P - sgn(Q)\sqrt{Q^2 + RR^\dagger + SS^\dagger}, \tag{2.3}$$

where P, Q, R, and S are matrices that depend on the deformation potentials a_v, b, and d of the valence band. We found that the heavy hole will be the hole ground state due to the shear separation potential, as in the case of a QW. We approximated the heavy hole confinement potential by a rectangular shape in which the depth was determined by its value in the center of the wire. This simplifies our calculation and we checked that including the nonrectangular shape only changes the hole energy by less than 2%.

Table 2.1: Material parameters for InAs and InP used in the calculations.

Parameter	InAs	InP
Lattice constant (Å)	6.058	5.869
Band gap (eV)	0.417	1.424
Electron mass (m_0)	0.026	0.08
Hh mass along [110] (m_0)	0.513	0.885
Hh mass along [001] (m_0)	0.333	0.532
a_c (eV)	-5.08	- -
a_v (eV)	1	- -
b (eV)	-1.8	- -
d (eV)	-3.6	- -
Strain coefficient C_{11} (GPa)	83.29	- -
Strain coefficient C_{12} (GPa)	45.26	- -
Dielectric constant	15.15	12.5

Different anisotropic effective masses are assumed inside and outside of the InAs/InP QWR and along the [001] and the [110] directions. In the adiabatic approach, one first solves the one-dimensional problem in the narrow [001] direction, and then uses the energy level found as the bottom of the potential well for a second one-dimensional problem in the other [110] direction [99]. This approach yields very good results as long as there is an appreciable difference in confinement widths [99], which is certainly the case for the wires studied here. The Coulomb interaction between the electron and the hole is not included as it is a small correction: from the formula for the upper bound of the exciton binding energy in a QW, this correction is estimated to be less than 9 meV [74]. All physical parameters used are listed in Table 2.1 and are taken from Refs. [98] and [116].

2.4 EXPERIMENTAL VERSUS NUMERICAL RESULTS AND DISCUSSION

Recombination of electrons and holes in the wires results in photoluminescence with photon energies ranging from 0.7-1.2 eV for the three samples (see Fig. 2.1). The samples A and B, grown at low temperature, have a broad PL signal, in which, for sample A, a clear distinction between the different contributions cannot be made. For sample B there are at least six Gaussian peaks present. Sample C has only two pronounced peaks at higher energies. It is apparent from the number of peaks that the growth conditions for sample C improve the homogeneity in wire height.

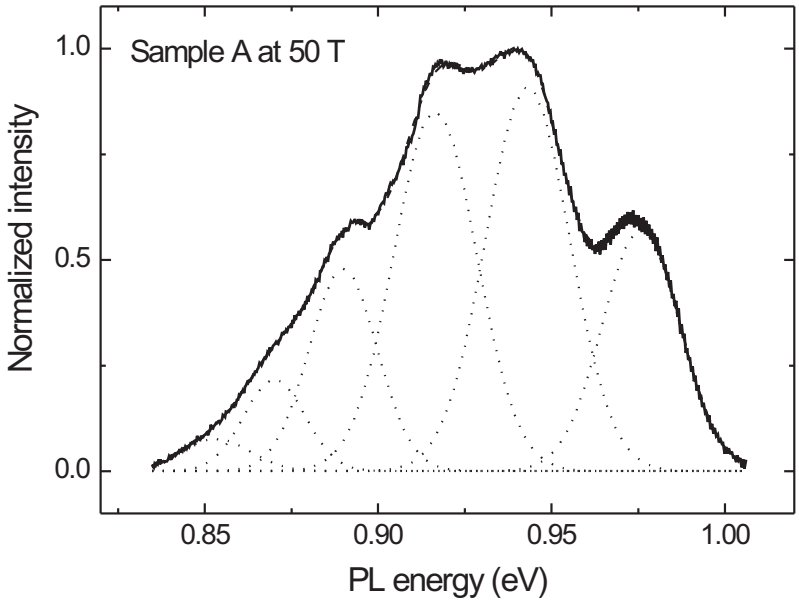

Fig. 2.2: In a high field of 50 T, the different contributions to the PL of sample A become narrower and are clearly distinguishable. The dotted lines are the fitted Gaussian contributions.

At zero field, sample A reveals a broad spectrum (122 meV overall width) with hardly any visible structure (see Fig. 2.1). If a magnetic field of 50 T is applied parallel to the growth direction [001], the various contributions to the PL become distinguishable (see Fig. 2.2). Since the overall width decreases to 95 meV, the peaks are not separated by the field, meaning that the individual PL peaks become discernable because they narrow in field. Since this effect is insignificant when the field is applied in the growth plane, it shows that for sample A, the zero-field linewidth of the different contributions is determined mostly by variations of the wavefunction extent in the growth plane; i.e., by the inhomogeneity in the width of the wires.

The different contributions to the PL from sample B can already be seen at zero field. This shows that the size inhomogeneity in the growth plane has improved substantially compared to that of sample A. It is therefore possible to compare the experimental peak energies with those expected from numerical calculations, using the assumption that the PL peaks originate from wires of different heights that vary by a discrete number of monolayers [51]. Taking into account that the exciton ground state is expected to consist of an electron bound to a heavy hole, the best correspondence in peak separation is found for wire heights from 6 to 13 ML (1 ML=0.303 nm for bulk InAs) for the high- to

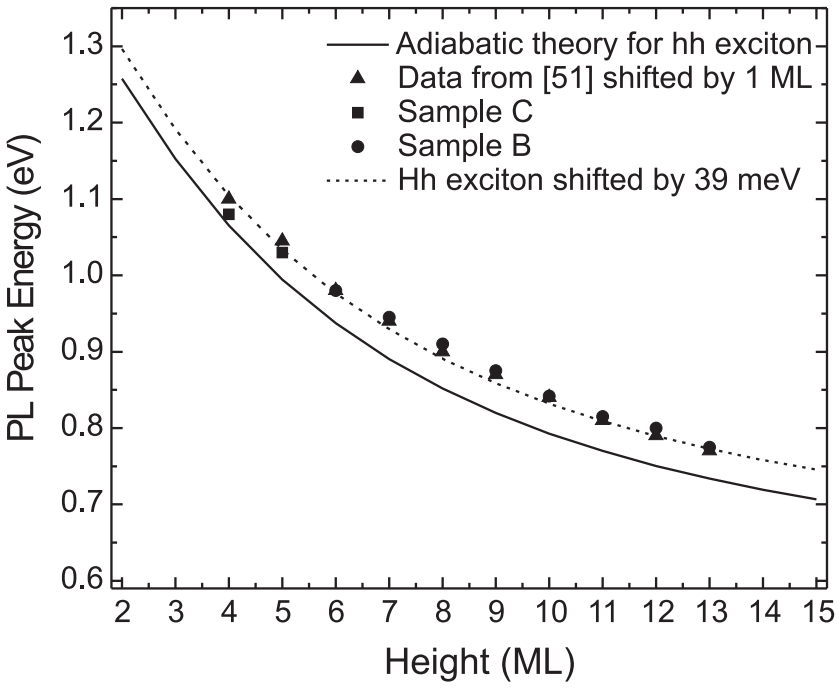

Fig. 2.3: PL peak energies as a function of the QWR height in the adiabatic approximation for heavy hole excitons (solid). The circles correspond to the peak positions for sample B and the squares to those of sample C. The triangles represent data from Ref. [51] and are shifted to the left by one monolayer. The dashed curve shows the calculated heavy-hole exciton PL peak energies shifted up by 39 meV.

low-energy peaks, respectively, and with the calculated peak energies shifted up by 39 meV (see Fig. 2.3). Such a shift is justified because of the uncertainty in the band offsets [98]. In comparison with data obtained on other samples and with values calculated using an eigenfunction expansion method (as reported in Ref. [51]), we find that the peaks originate from wires that are one monolayer thinner, which is in better correspondence with the heights obtained by AFM for those data [51].

The overall broadness of sample B complicates the analysis of the in-field data due to technical limitations. Therefore, qualitative results are only obtained for the peak at 0.94 eV, which is the most intense and has a relatively large separation from the other peaks. From Fig. 2.3, the PL at 0.94 eV is assigned to annihilation of an exciton bound to a 7 ML (or 2.1 nm) high wire. When applying a magnetic field parallel to [110], the exciton wavefunction extent in the direction of the wire height is investigated, and thus a parabolic

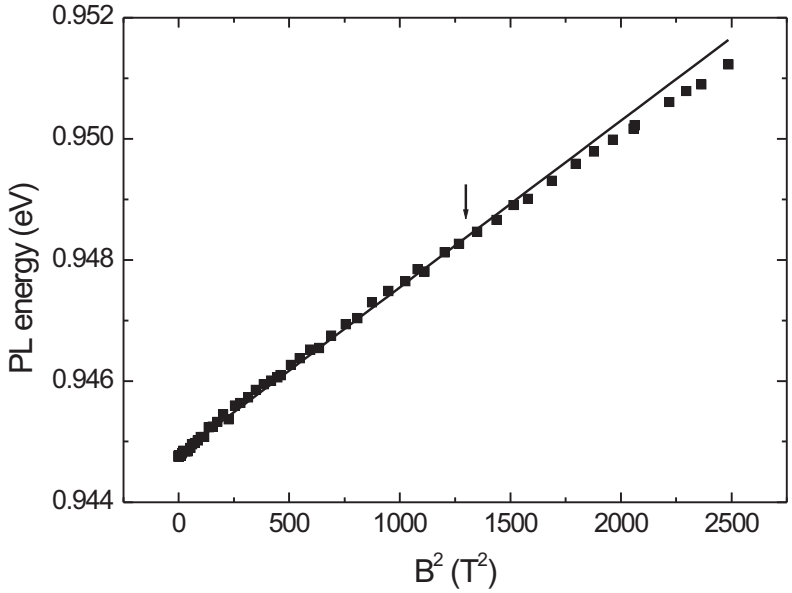

Fig. 2.4: PL peak energy as function of the square of the magnetic field $\mathbf{B}//[110]$ for the 0.94 eV peak of sample B. The solid line is the extrapolation of a linear fit between 0 and 1300 T^2. The deviation of the data from the straight line, indicated by the arrow, demonstrate a nonparabolic field dependence of the ΔE and thus a relatively large exciton radius.

field dependence of the diamagnetic shift might be expected up to 50 T due to the small wire height. However, when the PL energy is plotted against B^2 (see Fig. 2.4) a clear deviation from the linear behavior is detected. The exciton wavefunction size is thus much larger than the wire height of 2.1 nm. A magnetic length of 2.1 nm corresponds to 149 T, whereas the deviation starts at 36 T, as indicated by the arrow in Fig. 2.4. Such a field gives a magnetic length of 4.3 nm and a $\langle \rho^2 \rangle^{1/2}$ of 6.0 nm using the model from Ref. [113]. The data therefore demonstrate that the QWR is too thin to enclose a large portion of the wavefunction, which must be partially located in the InP matrix above and/or below the InAs wire. Such a penetration of the wavefunction into the barrier material is common in nanostructures that have weak charge localization, such as in GaAs/AlGaAs QWRs formed by junction of QWs [95] or by a bend in a well [86, 101], but was not anticipated in the samples under study due to the large conduction and valence band offsets of 657 and 350 meV, respectively. For comparison, the conduction band offset is 225 meV for

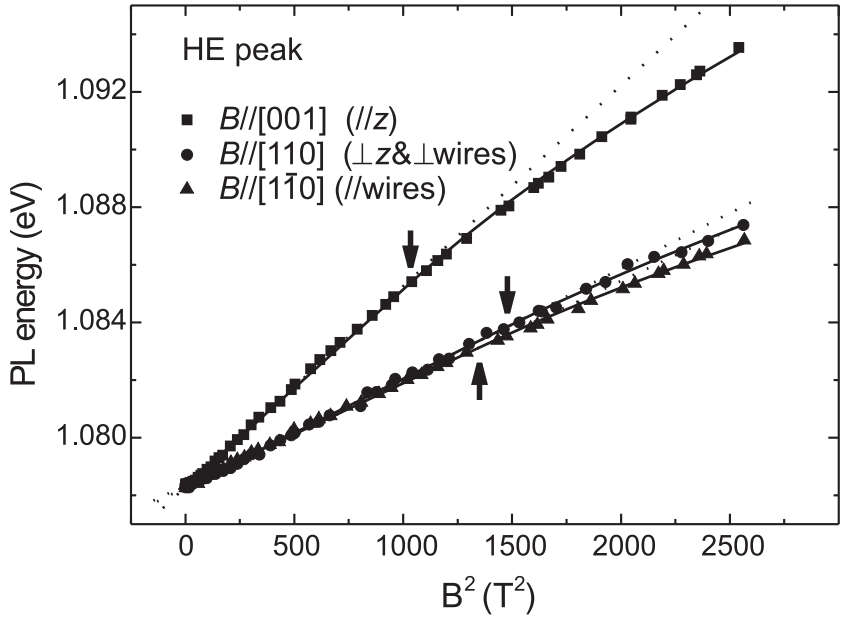

FIG. 2.5: The same as Fig. 2.4, but now for the HE peak of sample C where the magnetic field is applied along the three different crystallographic directions indicated in the inset of Fig. 2.1. The arrows indicate the crossover fields. The dashed lines are extrapolations of the parabolic field dependence.

Table 2.2: PL energies, crossover fields, and associated exciton extents for the two pronounced peaks of sample C and all three field directions.

Peak	Field direction	Crossover field (T)	Exciton extent (nm)
LE (1.03 eV)	[001] ($B//z$)	37.7	5.9
	[1$\bar{1}$0] ($B//wires$)	43.5	5.5
	[110]	$\geq$43.5	$\leq$5.5
HE (1.08 eV)	[001] ($B//z$)	32.1	6.4
	[1$\bar{1}$0] ($B//wires$)	36.7	6.0
	[110]	38.6	5.8

GaAs/$Al_{0.3}Ga_{0.7}$As QWRs [101], 79 meV for $In_{0.1}Ga_{0.9}$As/GaAs QWs [98], and 120 meV for Ge/Si QDs [102].

Sample C, which has a less broad overall spectrum and well-separated peaks, is best suited for analysis of the diamagnetic energy shift. Due to the low number of peaks, it is not possible to compare the curvature in peak energy versus wire height with the numerical PL energies of Fig. 2.3. However, because of

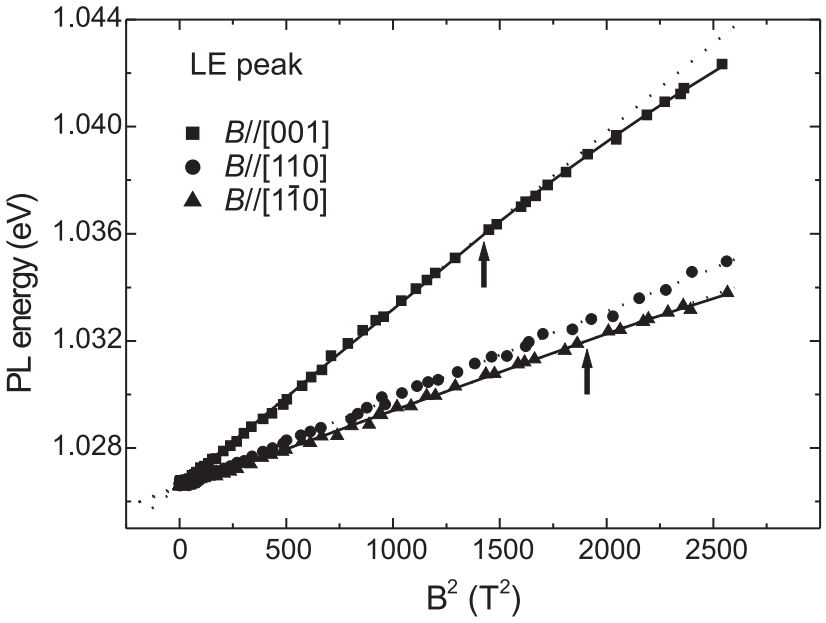

Fig. 2.6: The same as Fig. 2.5, but now for the LE peak of sample C.

the larger growth temperature, and thus a larger As/P exchange during the capping procedure [97], there is less InAs present in the wire than for sample B, and reduced dimensions are expected for the wire height and/or width. By comparing the PL energies with those of sample B, wire heights of 4 and 5 ML are estimated for the high-energy (HE) and low-energy (LE) peaks, respectively (see Fig. 2.3). In Fig. 2.5 the PL energy of the HE peak is plotted as a function of B^2 for all three field directions. They are analyzed with aforementioned set of expressions [113] and the dashed lines are the extrapolation of the parabolic dependence. It is clear from these extrapolations that all three curves deviate from a linear B^2 dependence. The crossover fields as provided by our model are given in Table 2.2, together with the corresponding exciton extents. Note that, as mentioned in section 2.3, for crossover fields this close to the maximum obtainable field, these sizes are a qualitative measure of the exciton extent rather than of the real exciton radius. For $B//[110]$, the clear deviation from the linear B^2 behavior for the HE peak reflects the vertical spread of the wavefunction into the InP, which we also observed for sample B. Since in the $(1\bar{1}0)$ plane (the wire cross section), the direction of strongest confinement is [001], the diamagnetic shift with a field applied along $[1\bar{1}0]$ resembles most that of the $B//[110]$ situation, as can be seen in Fig. 2.5 and Table 2.2.

The LE peak of sample C has a less obvious sublinear dependence on B^2 for $B//[1\bar{1}0]$, and for $B//[110]$ a deviation from the linear behavior is not even detected (see Fig. 2.6). The latter means that the crossover field is larger than that for $B//[1\bar{1}0]$ and thus that 5.5 nm is an upper limit for the exciton extent in the wire height direction (see Table 2.2). If we now compare the exciton extents for $B//[110]$ and both peaks, we observe a *decrease* from 5.8 to $\leq$5.5 nm for *increasing* wire height. This means that the exciton extent significantly decreases as the wires becomes thicker and a larger portion of the exciton wavefunction is confined to the InAs QWR.

The inverse relation of the exciton extent to the wire height is clarified by Fig. 2.7, where a schematic diagram of a wavefunction confined to a nanostructure is given. If the potential well is not too narrow, a decrease in size leads to a shrinkage of the wavefunction extent; i.e., in Fig. 2.7(b) the extent is smaller than in Fig 2.7(a). However, if it is made even thinner, the confinement energy becomes comparable to the band offset. This causes the wavefunction to significantly spread out into the barrier material and thus to increase its extent with decreasing wire height (compare Figs. 2.7(b) and 2.7(c)).

Calculated contour plots of the electron and heavy-hole wavefunctions reveal that for a wire height of 5 ML, the electron radius is much larger than that of the heavy-hole in the direction of the wire height, and that the electron is indeed substantially spread out into the InP (see Fig. 2.8 insets (a) and (b)). This is made more quantitative in Fig. 2.8 by the calculation of the percentage of the electron and hole wavefunction inside the QWR as function of the height of the QWR for a width of 180 Å. We now make a qualitative comparison of the numerical *electron* wavefunction radius with the experimental *exciton* extent. The theoretical data confirm the inverse dependence on the wire height up to 6 ML (18.18 Å) for the electron (see Fig. 2.9). Between 4 and 5 ML the theoretical decrease in the electron wavefunction radius with wire height is found to be 7%, which corresponds reasonably well with the experimental decrease in exciton wavefunction extent of $\geq$5% between HE and LE of sample C. For these flat wires, a considerable portion of the electron wavefunction is indeed found to

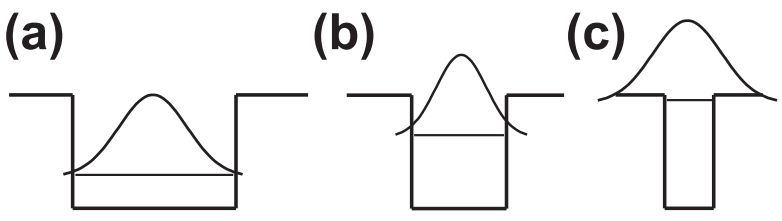

FIG. 2.7: Schematic drawing of the change in confinement with wire height.

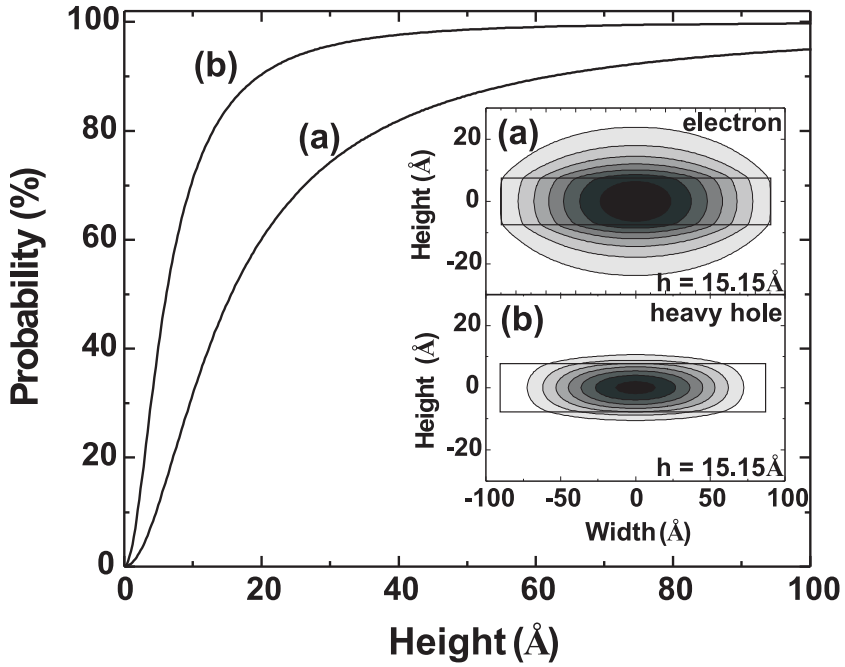

Fig. 2.8: Probability of (a) the electrons and (b) the heavy-holes to be inside the QWR as a function of the wire height. The insets are the contour plots of the (a) electron and (b) heavy-hole wavefunctions confined to a QWR with height 5 ML (15.15 Å) and width 180 Å.

be located above and below the QWR, i.e., 61% and 51% for heights of 4 and 5 ML, respectively (see Fig. 2.8), resulting in respective electron wavefunction radii of 0.74 and 0.69 nm in the [001] direction (see Fig. 2.9).

The wire height at which the exciton wavefunction is smallest indicates the regime in which the wavefunction spill-over starts to be significant, and is found to be at 6 ML (18.18 Å). This is about 3 times smaller than the 50 Å that was experimentally and theoretically deduced for the $In_{0.1}Ga_{0.9}As/GaAs$ QW structures [100, 103, 105], although the confining potential for the electron is about five times larger in the InAs/InP wires [98].

2.5 CONCLUSIONS

Magneto-photoluminescence experiments and theoretical calculations within the effective mass approximation were combined to study the charge confinement in self-assembled InAs/InP QWR samples. Despite the large conduction

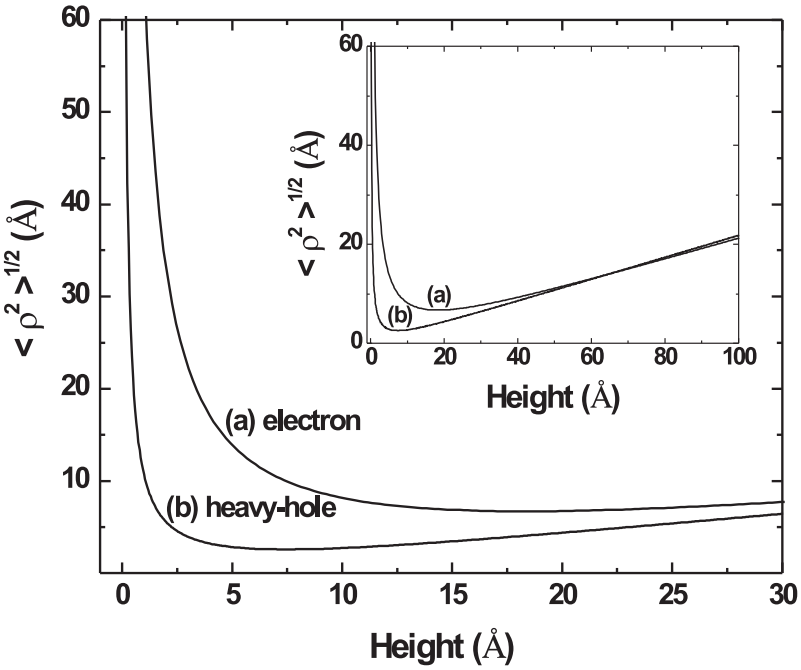

FIG. 2.9: Wavefunction radii for (a) the electron and (b) the heavy-hole in the [001] direction. The inset shows the same information but for much larger heights.

band offset, the confinement energy for thin wires is large enough to cause a considerable portion of the electron wavefunction to be located outside the wire in the direction of the wire height. In this regime, a decrease of the electron wavefunction extent is experimentally observed for increasing wire height in agreement with the theoretical calculations.

The wavefunction penetration into the barrier is a crucial aspect that has to be kept in mind for applications since it reduces the electron-hole overlap and augments carrier escape at room temperature. To avoid these effects, growth procedures should be focused on enhancing the size uniformity of wires (and dots) with a height of at least 6 ML.

Publications. The results in this chapter were published as:

- J. Maes, M. Hayne, Y. Sidor, B. Partoens, F. M. Peeters, Y. González, L. González, D. Fuster, J. M. García, and V. V. Moshchalkov, *Electron wave-function spill-over in self-assembled InAs/InP quantum wires*, Phys. Rev. B **70**, 155311 (2004).

- The paper Phys. Rev. B **70**, 155311 (2004) was also selected for the November 1, 2004 issue of Virtual Journal of Nanoscale Science & Technology.

3

Exciton in a quantum wire in the presence of parallel and perpendicular magnetic fields

3.1 INTRODUCTION

The investigation of low-dimensional structures, such as semiconductor quantum wires and quantum dots, have attracted much attention for potential application in high performance devices since they are theoretically predicted to offer superior optical and electrical characteristics [3, 117]. A few main techniques exist to fabricate QWRs, such as electron beam lithography and etching, growth on nonplanar substrates, selective growth on masked substrate, molecular beam epitaxy, and cleaved-edge overgrowth method. Different shapes for QWRs using the aforementioned methods have been realised, for example the T-shaped QWRs [5, 118, 119] and the V-shaped QWRs [39, 120–123] have been studied theoretically and investigated experimentally. Early work for rectangular-shaped QWRs by Degani *et al.* [87] and later other several studies used model calculations to describe the properties of excitons confined to unstrained QWRs [124–126]. Approaches, which show the role of electron-hole Coulomb interaction together with realistic profiles of the confining potential (see for example Refs. [124, 127]) have also been presented. On the other hand, valence-band mixing effects in the T-shaped and the V-shaped QWRs was studied by Goldoni *et al.* [90] using four-band $\mathbf{k}\cdot\mathbf{p}$ theory, by Stier *et al.* [92] using eight-band $\mathbf{k}\cdot\mathbf{p}$ theory which was later applied to rectangular-shaped QWRs [91]. In all the latter cases the Coulomb interaction was neglected and

the calculation was done for zero magnetic field. There has been much theoretical interests in the study of the magnetic properties of QWRs. Kyrychenko *et al.* [94] performed calculations of the valence band states in diluted semiconductor QWR structures. They showed that it is possible to control the relative contribution of the light- and the heavy-hole components of the total wavefunction of the holes by changing an external magnetic field. Bryant *et al.* [95] calculated the diamagnetic shift in T-shaped QWRs with perturbation theory and lately Madureira *et al.* [75] have investigated the magnetoexciton states and optical-absorption spectrum in QWRs. They found an enhancement of the exciton binding energy with increasing magnetic field, as was expected from experimental data.

Recently, considerable efforts was devoted to the achievement of self-assembled QWRs, which can be formed under certain growth conditions by solid source molecular beam epitaxy. In this case the wires are formed by the Stranski-Krastanow growth mode in which the materials which are deposited on top of each other have a substantially different lattice parameter. Spontaneous formation of self-assembled InAs QWRs on InP (001) substrate, having 3.2% lattice mismatch, was recently demonstrated [8, 128]. These nanostructures are promising candidates for light emitting devices for wavelengths 1.3 and 1.55 μm [51, 129]. They have rectangular shape and show a broad PL spectrum with several peaks that correspond to different heights of the QWRs which can differ by a number of monolayers [51].

The aim of the present work is to investigate the magnetic-field dependence of the exciton energy in such QWRs. We consider V-shaped GaAs/$Al_{0.4}Ga_{0.6}$As QWRs studied experimentally in Ref. [39] and also self-assembled rectangular InAs/InP QWRs which were investigated experimentally in Refs. [51] and [129] in the presence of an externally applied magnetic field. In our approach we include the true geometrical shape of the wire, as well as the mass mismatch between the wire and the barrier. The calculations are based on a finite difference scheme within the single-band effective mass approximation. Since strain is important for the formation of the self-assembled QWRs we include the influence of strain on the confinement potential for both the electron and the hole. We calculate the diamagnetic shift of the exciton energy for both V-shaped and self-assembled QWRs, when the magnetic field is along different directions of the QWR. We analyze different sizes and shapes of the QWRs and compare them with the experimental measurements. The effect of the Coulomb interaction between the electron and the hole is also studied.

This chapter is organized as follows. In Sec. 3.2, we describe briefly the method and the theoretical model. The influence of strain on the electronic structure in InAs/InP self-assembled QWRs is discussed in Sec. 3.3. Section 3.4 is devoted to the study of the Coulomb interaction in QWRs. In the last section 3.5 of this chapter, we present results of the excitonic spectrum in a magnetic field and make a detailed comparison with available experimental data.

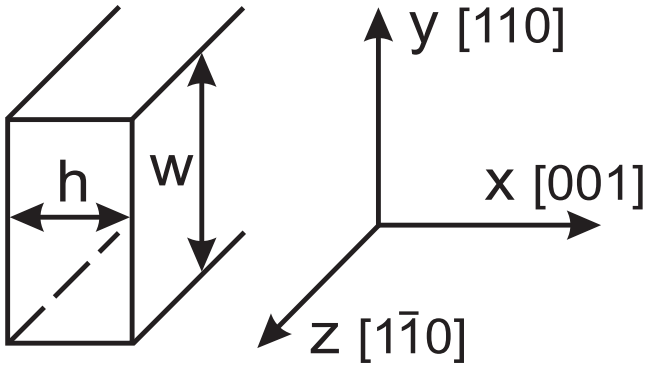

Fig. 3.1: Schematic illustration of a two-dimensional rectangular quantum box with height h and width w which reproduce the model of rectangular self-assembled InAs/InP QWR.

3.2 THEORY

3.2.1 Theoretical model and basic equations

We deal with the optical properties near the fundamental band-gap energy for GaAs/$Al_{0.4}Ga_{0.6}$As and InAs/InP QWRs. We assume that the conduction and highest valence bands are decoupled. The full Hamiltonian for the system can be written in the form

$$H = H_e + H_h + U(x_e - x_h, y_e - y_h, z_e - z_h), \tag{3.1}$$

where H_e is the electron Hamiltonian, H_h is the hole Hamiltonian and the Coulomb interaction between the electron and the hole is

$$U(x, y, z) = -\frac{e^2}{\varepsilon\sqrt{x^2 + y^2 + z^2}}, \tag{3.2}$$

where ε is taken as the average value of the wire and the barrier. We can assume this approximation, since there is only a small variation of ε inside and outside the QWR.

Let us first introduce the Hamiltonian for the InAs/InP QWR. In this work, we consider the geometry of InAs/InP QWR, as a 2D rectangular quantum box with height h along the x-direction and width w along the y-direction. Different effective masses are assumed inside and outside the wire. We identify the crystal orientations [001], [110], and [1$\bar{1}$0] with the x, y, and z axes, as depicted in Fig. 3.1, where [1$\bar{1}$0] is the growth direction corresponding to the experiment [51, 129] situation.

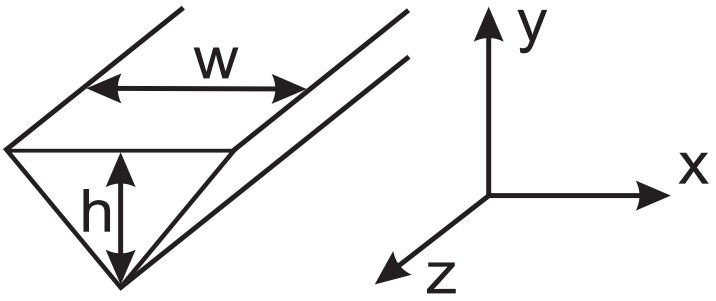

FIG. 3.2: Schematic illustration of a triangular shaped QWR with height h and base length w.

The single-particle Hamiltonian for the electron in the presence of strain is the following

$$H_e = -\nabla_{xe}\frac{\hbar^2}{2m_e^*(x,y)}\nabla_{xe} - \nabla_{ye}\frac{\hbar^2}{2m_e^*(x,y)}\nabla_{ye} + E_{ce}(x,y) + a_c\varepsilon_{hyd}(x,y), \quad (3.3)$$

where m_e^* is the effective mass of the electron, $E_{ce}(x,y)$ is the unstrained conduction band offset, a_c is the hydrostatic deformation potential for the conduction band and $\varepsilon_{hyd}(x,y)$ denotes the hydrostatic strain. The Hamiltonian describing the heavy-hole and the light-hole states is respectively given by

$$H_{hh} = -\nabla_{xhh}\frac{\hbar^2}{2m_{hh}^*(x,y)}\nabla_{xhh} - \nabla_{yhh}\frac{\hbar^2}{2m_{hh}^*(x,y)}\nabla_{yhh} + V_{vhh}(x,y), \quad (3.4)$$

$$H_{lh} = -\nabla_{xlh}\frac{\hbar^2}{2m_{lh}^*(x,y)}\nabla_{xlh} - \nabla_{ylh}\frac{\hbar^2}{2m_{lh}^*(x,y)}\nabla_{ylh} + V_{vlh}(x,y), \quad (3.5)$$

m_{hh}^*, m_{lh}^* are the effective masses of the heavy- and the light-holes, respectively, $V_{vhh}(x,y)$ and $V_{vlh}(x,y)$ are the confinement potentials for both holes due to the band offsets and strain. To derive these potentials we use the diagonalized 4x4 Pikus-Bir Hamiltonian [71]

$$V_{vhh}(x,y) = E_{vh}(x,y) + P + sgn(Q)\sqrt{Q^2 + RR^\dagger + SS^\dagger}, \quad (3.6)$$

$$V_{vlh}(x,y) = E_{vh}(x,y) + P - sgn(Q)\sqrt{Q^2 + RR^\dagger + SS^\dagger}, \quad (3.7)$$

where $E_{vh}(x,y)$ is the unstrained valence band offset between the wire and the barrier material, P, Q, R and S are matrix elements which can be calculated using the deformation potentials a_v, b and d of the valence band and the components of the strain tensor ε

$$P = a_v(\varepsilon_{xx} + \varepsilon_{yy} + \varepsilon_{zz}), \quad (3.8)$$

$$Q = \frac{b}{2}(\varepsilon_{xx} + \varepsilon_{yy} - 2\varepsilon_{zz}), \tag{3.9}$$

$$R = -\frac{\sqrt{3}}{2}b(\varepsilon_{xx} - \varepsilon_{yy}) + id\varepsilon_{xy}, \tag{3.10}$$

$$S = -d(\varepsilon_{zx} - i\varepsilon_{yz}). \tag{3.11}$$

In order to obtain the strain components of the QWR within the square cross section we adapted the method given by Downes [73]. ε_{xx} and ε_{yy} are determined as a function of the height and the width of the wire, while ε_{zz} is equal to the misfit strain $\epsilon_0 = (a_{0InAs} - a_{0InP})/a_{0InP}$ within the strained QWR and equal to zero in the barrier. Therefore, the expression $\varepsilon_{hyd}(x,y) = \varepsilon_{xx} + \varepsilon_{yy} + \varepsilon_{zz}$ in the case of hydrostatic strain for the electron, depends only on the x and the y coordinates, as well as the confinement potentials for the holes $V_{vhh}(x,y)$ and $V_{vlh}(x,y)$.

The Hamiltonian of the V-shaped wire for the electron and for the hole is the same as for the self-assembled wires, but without the strain parts. We take, like in previous case, different masses inside the wire and in the barrier. As shown in Fig. 3.2, we use for the simulation a triangular shape of the QWR with height h and base length w.

In the case of an applied magnetic field the kinetic operator for the particles is given by

$$T^{e,h}(x,y) = \left(\mathbf{p}_{e,h} - \frac{q}{c}\mathbf{A}\right)\frac{1}{2m^*_{e,h}}\left(\mathbf{p}_{e,h} - \frac{q}{c}\mathbf{A}\right), \tag{3.12}$$

where q is the charge of the particle, $\mathbf{p} = -i\hbar\nabla$ is the momentum and $\mathbf{A}$ is the vector potential of the magnetic field. The gauge is chosen such that it simplifies the problem as much as possible.

When the magnetic field is applied along the wire growth direction, *i.e.* $\mathbf{B} = B\hat{z}$, we chose the symmetric gauge $\mathbf{A} = \frac{B}{2}(-y\hat{x} + x\hat{y})$. Then the aforementioned kinetic-energy term for the electron and the hole (the subscripts are left out of the equation) can be written as

$$\begin{aligned} T(x,y) \;=\; & p_x\frac{1}{2m^*(x,y)}p_x + p_y\frac{1}{2m^*(x,y)}p_y + \frac{qBy}{4m^*(x,y)c}p_x + \frac{qBy}{4c}\frac{p_x}{m^*(x,y)} \\ & - \frac{qBx}{4m^*(x,y)c}p_y - \frac{qBx}{4c}\frac{p_y}{m^*(x,y)} + \frac{q^2B^2}{8c^2m^*(x,y)}(x^2+y^2). \end{aligned} \tag{3.13}$$

The total diamagnetic contribution to the kinetic part consists of five terms, from which the first four are linear and the last one is an extra parabolic confinement. Note that the resulting problem becomes two-dimensional.

Table 3.1: Input material parameters for InAs/InP and GaAs/$Al_{0.4}Ga_{0.6}As$ QWRs used in the calculations: lattice constant a_0, band gap E_g, electron mass m_e (Refs. [130–132]), heavy-hole mass m_{hh}, light-hole mass m_{lh}, the hydrostatic deformation potential for the conduction band a_c, the deformation potentials of the valence band a_v, b and d, strain coefficients C_{11} and C_{12}, and dielectric constant ε.

Parameter	InAs	InP	GaAs	$Al_{0.4}Ga_{0.6}As$
a_0 (Å)	6.058	5.869	- -	- -
E_g (eV)	0.417	1.424	1.519	2.018
m_e (m_0)	0.023	0.077	0.067	0.1
m_{hh}[110] (m_0)	0.513	0.885	0.51	0.61
m_{hh}[001] (m_0)	0.333	0.532	0.51	0.61
m_{lh} (m_0)	0.026	0.111	- -	- -
a_c (eV)	-5.08	- -	- -	- -
a_v (eV)	1	- -	- -	- -
b (eV)	-1.8	- -	- -	- -
d (eV)	-3.6	- -	- -	- -
C_{11} (GPa)	83.29	- -	- -	- -
C_{12} (GPa)	45.26	- -	- -	- -
ε	15.15	12.5	12.9	11.76

For the magnetic field applied parallel to the y-direction $\mathbf{B} = B\hat{\mathrm{y}}$, the following non-symmetric gauge is used $\mathbf{A} = -Bx\hat{z}$. With this gauge the kinetic-energy term is

$$\begin{aligned} T(x,y) &= p_x \frac{1}{2m^*(x,y)} p_x + p_y \frac{1}{2m^*(x,y)} p_y \\ &\quad + p_z \frac{1}{2m^*(x,y)} p_z - \frac{qBxp_z}{cm^*(x,y)} + \frac{q^2B^2x^2}{2c^2m^*(x,y)}. \end{aligned} \tag{3.14}$$

The total Hamiltonian (with the confinement) still commutes with p_z, and therefore the wavefunction in the z-direction can still be taken as a plane wave. The ground state is obtained for p_z=0.

Consider now the case of a magnetic field oriented along the x-direction. If we choose the vector potential as $\mathbf{A} = By\hat{z}$, then the kinetic part of the Hamiltonian is given by the equation

$$\begin{aligned} T(x,y) &= p_x \frac{1}{2m^*(x,y)} p_x + p_y \frac{1}{2m^*(x,y)} p_y \\ &\quad + p_z \frac{1}{2m^*(x,y)} p_z + \frac{qByp_z}{cm^*(x,y)} + \frac{q^2B^2y^2}{2c^2m^*(x,y)}. \end{aligned} \tag{3.15}$$

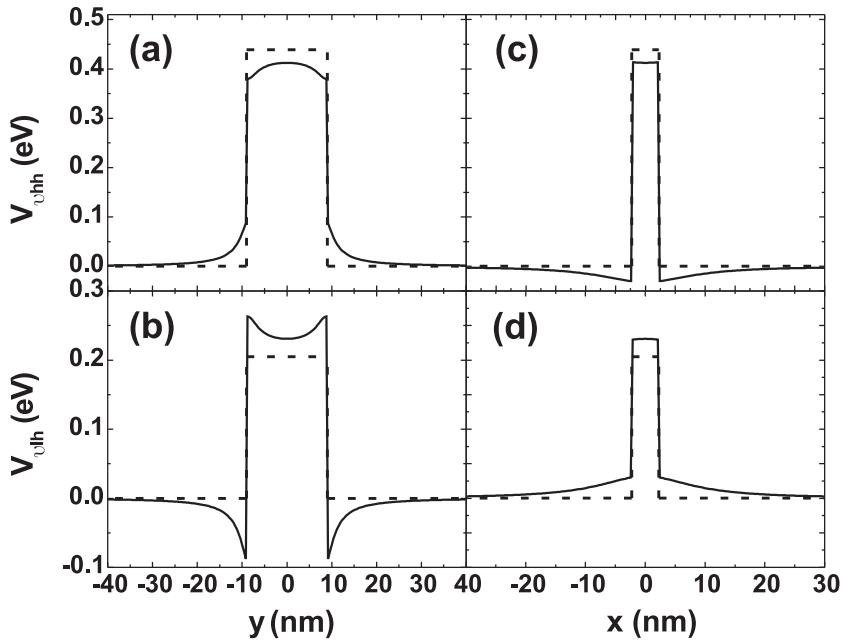

Fig. 3.3: Heavy-hole ((a) and (c)) and light-hole ((b) and (d)) band edges of InAs/InP QWR with w=180 Å and h=15 ML (1 ML is 3.03 Å) along the x- and the y-direction. The full curves and dashed curves denote potentials calculated from the strain Hamiltonian with and without (shear potential) off-diagonal matrix elements, respectively.

Again p_z commutes with the Hamiltonian and as a result the problem is still 2D.

3.2.2 Solution methods

The electron and hole states in the QWR were solved separately and can be described by the following Schrödinger equations

$$H_e\Psi_e(x_e, y_e) = E_e\Psi_e(x_e, y_e), \tag{3.16}$$

$$H_{hh}\Psi_{hh}(x_{hh}, y_{hh}) = E_{hh}\Psi_{hh}(x_{hh}, y_{hh}), \tag{3.17}$$

$$H_{lh}\Psi_{lh}(x_{lh}, y_{lh}) = E_{lh}\Psi_{lh}(x_{lh}, y_{lh}). \tag{3.18}$$

In order to solve these single-particle equations we used two independent numerical procedures, one is based on a two-dimensional finite difference technique with uniform grid space, while the other relies on finite element technique. In these methods the real 2D confinement potential and the different masses

inside and outside of the QWR for the different particles was included. The values of the parameters used in the calculations are listed in Table 3.1. All parameters have been taken from Ref. [98], unless indicated otherwise.

3.2.3 Coulomb interaction

In the next step, we consider the Coulomb interaction between the particles. Electron and hole are confined in the x- and the y-directions and can move freely along the wire direction. Because of the strong confinement in the xy-plane we are allowed to separate the z motion from the lateral motion in the xy-plane and to assume that the Coulomb interaction has no effect on the xy-motion of the particles. In this case an approximate solution to Eq. (3.1) has the form

$$\Psi(x_e, x_h, y_e, y_h, z) = \Psi_e(x_e, y_e)\Psi_h(x_h, y_h)\varphi(z), \tag{3.19}$$

where $\varphi(z)$ is the wavefunction which describes the relative motion of the exciton in the z-direction, *i.e.* $z = z_e - z_h$. Averaging the Hamiltonian over the x-y direction with the above wavefunctions we obtain an effective one-dimensional equation for the motion in the wire direction

$$\left[E_e + E_h - \frac{\hbar^2}{2\mu_z}\nabla_z^2 + U_{eff}(z)\right]\varphi(z) = E_{ex}\varphi(z), \tag{3.20}$$

where μ_z is the reduced mass of the electron and hole along the wire axis and $U_{eff}(z)$ is the effective potential which can be described by

$$\begin{aligned} U_{eff}(z) &= \int\int\int\int dx_e dy_e dx_h dy_h |\Psi_e(x_e, y_e)|^2 \\ &\quad |\Psi_h(x_h, y_h)|^2 U(x_e - x_h, y_e - y_h, z), \end{aligned} \tag{3.21}$$

$$\begin{aligned} \frac{1}{\mu_z} &= \int\int\int\int dx_e dy_e dx_h dy_h |\Psi_e(x_e, y_e)|^2 \\ &\quad |\Psi_h(x_h, y_h)|^2 \left(\frac{1}{m_e^*(x_e, y_e)} + \frac{1}{m_h^*(x_h, y_h)}\right). \end{aligned} \tag{3.22}$$

In order to solve Eq. (3.20) we have to perform a four-dimensional integration to calculate the effective potential. We used two independent methods to calculate $U_{eff}(z)$: a direct integration and an analytical method based on the Fourier transformation of the Coulomb potential. The exciton binding energy is then obtained from a solution of the Eq. (3.20) which was solved numerically using a finite difference scheme.

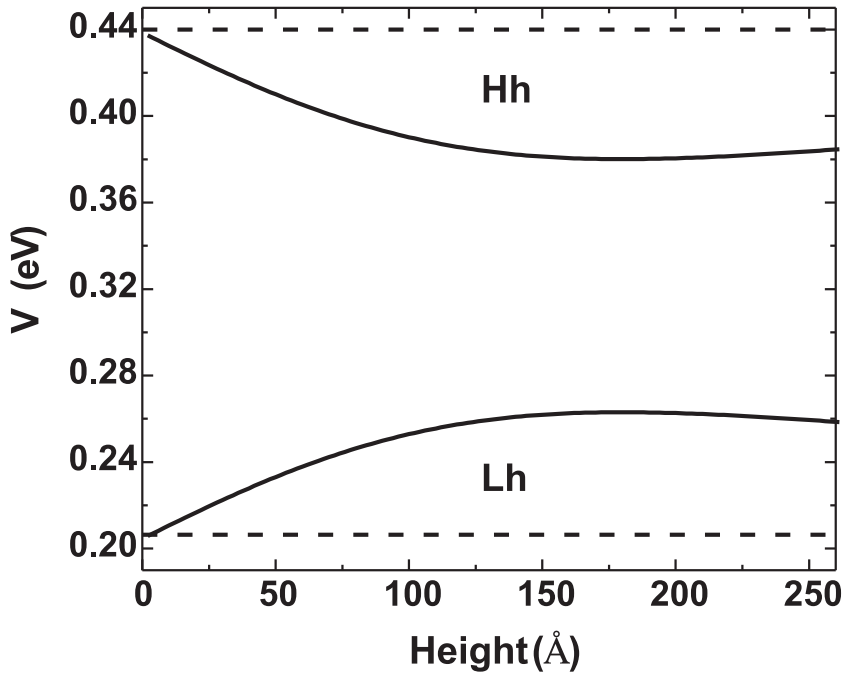

Fig. 3.4: The center of the confinement potentials for heavy-hole and light-hole as function of the height of the InAs/InP QWR with w=180 Å. The dashed curves are the corresponding values for the shear potential.

3.3 SELF-ASSEMBLED QUANTUM WIRES WITH STRAIN

The formation of self-assembled InAs/InP QWRs is based on the strain-relaxation effect. It is therefore interesting and important to investigate the influence of strain on the electronic properties of the QWR. For the electron, as was defined in Eq. (3.3), the edge of the conduction band is shifted down by the hydrostatic strain $a_c\varepsilon_{hyd}$, which is 144 meV for InAs/InP QWR. It should be noted, that in our strain calculation model this value is independent of the size of the QWR, because the sum of the normal strain components $\varepsilon_{hyd} = \varepsilon_{xx} + \varepsilon_{yy} + \varepsilon_{zz}$ is constant [133]. It means that in the presence of strain the bottom of the electron confinement potential is shifted by the value of the hydrostatic strain.

In the case of the holes the situation is more complicated. The heavy-hole and light-hole band edges can be obtained from the aforementioned Pikus-Bir Hamiltonian, characterized in Sec. 3.2 by the formulas (3.6) and (3.7). In Fig. 3.3 the results for the profiles of the confinement potential for the heavy-

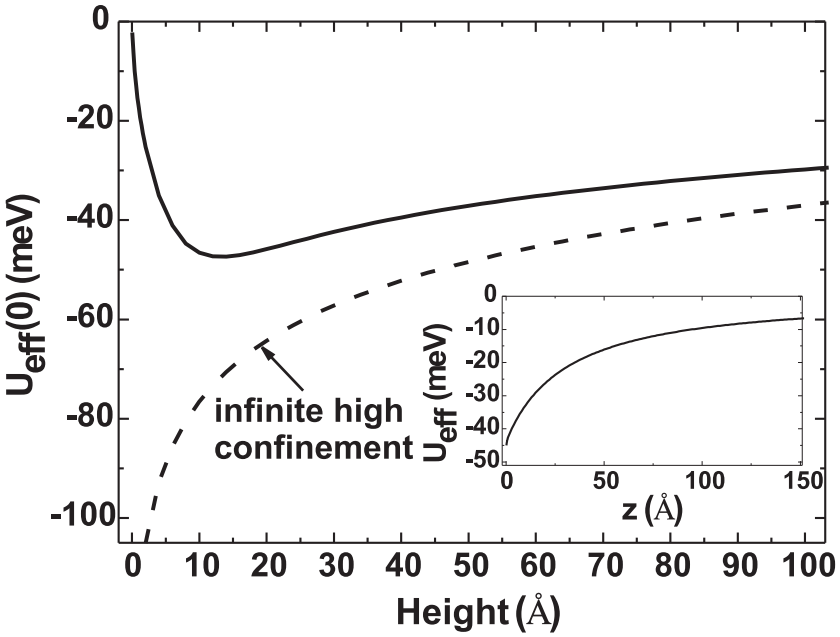

FIG. 3.5: The effective Coulomb potential at z=0 as a function of the height of the InAs/InP QWR with w=180 Å. The inset shows the effective Coulomb potential as a function of the z-direction for a wire width w=180 Å and wire height h=5 ML.

and light-hole along the x- and y-direction are compared. We plotted the case when the off-diagonal R and S matrices are neglected (dashed curves) and the case when the strain Hamiltonian includes all matrix elements (full curves). The first simple case gives the same behavior as for the conduction band, *i.e.* the edges of the valence band for the heavy- and light-holes are shifted by a value which depends on the P and Q diagonal matrix elements.

Further we investigate the dimensional dependence of the heavy-hole and light-hole confinements for fixed width of the QWR as a function of the height, which is shown in Fig. 3.4. For this purpose we take the central point of the potentials and observe their dependence on the height of the QWR, as depicted by the full curves. Note that the heavy-hole is above the light-hole states in the range of the height from 0 to 250 Å and therefore is the ground state. This means that heavy- and light-holes in flat QWRs behave in a similar way as in quantum wells.

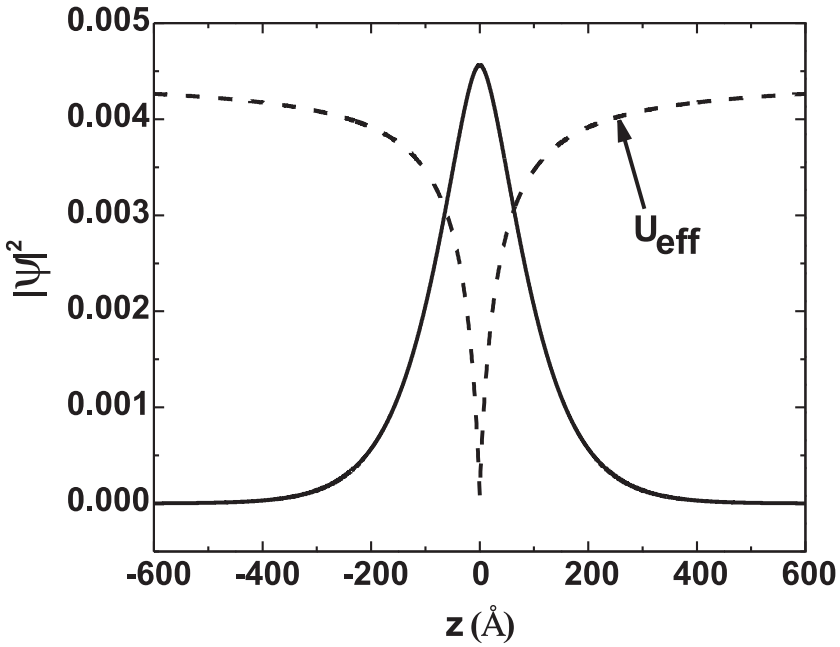

Fig. 3.6: The probability density (solid curve) and effective potential (dashed curve) of the exciton in InAs/InP QWR as a function of the z-direction for w=180 Å and h=5 ML.

3.4 CONTRIBUTION OF COULOMB INTERACTION TO THE PHOTOLUMINESCENCE ENERGY

Here we investigate the Coulomb interaction between the electron and the hole in the wire. Using the wavefunctions from a numerical solution of the single-particle equation for the electron and the heavy-hole we perform a direct integration in order to calculate the effective Coulomb potential $U_{eff}(z)$ (see Eq. (3.21)). The heavy-hole state is the ground state for the InAs/InP QWR, as was mentioned before, and for the GaAs/$Al_{0.4}Ga_{0.6}$As QWRs, because the valence bound confinement depth is the same for the light- and the heavy-holes for these V-shape wires. In Fig. 3.5 we plot the effective potential $U_{eff}(0)$ as a function of InAs/InP wire height (solid curve) and compare the results with the case when the confinement potential along the x- and y-direction is assumed to be infinitely high (dashed curve). The difference in the behavior for small values of the wire height is a result of the wavefunction spill-over effect (see chapter 2). For the infinity potential the wavefunction will always be confined inside the potential well, and the potential divergence at z=0 when $h \to 0$.

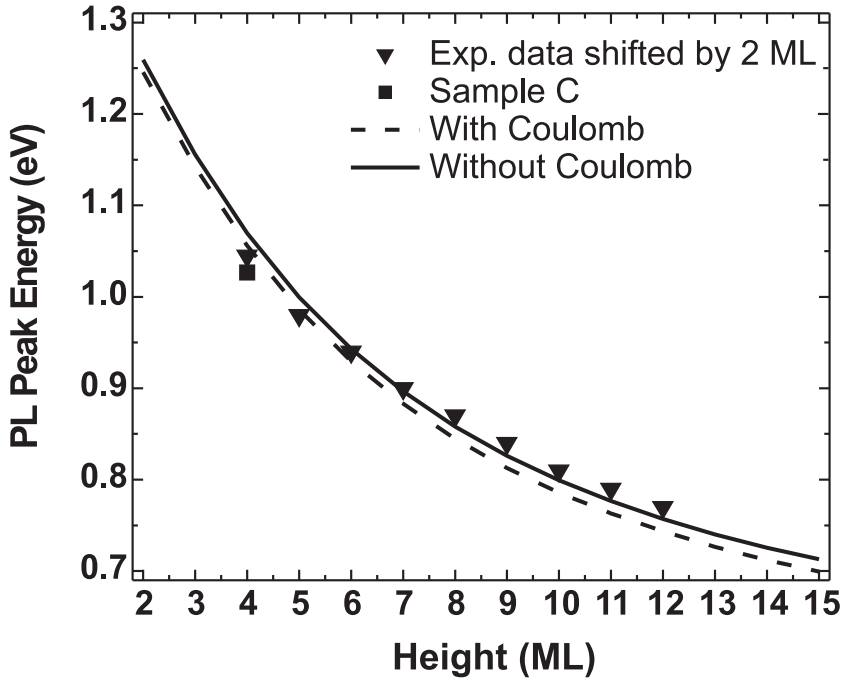

FIG. 3.7: PL peak energies as a function of the InAs/InP QWR height. The solid and dash lines are the theoretical calculations for the heavy-hole excitons with and without taking into account the Coulomb interaction, respectively. The triangles correspond to the experimental data from Ref. [51] shifted by 2 ML and the square to sample C (see chapter 2 and Ref. [134]).

The inset of Fig. 3.5 shows the calculated effective Coulomb potential for the InAs/InP QWR when w=180 Å and h=5 ML.

In the next step, having the effective Coulomb potential, we solve the one-dimensional effective Schrödinger equation, Eq. (3.20), for the relative exciton wavefunction in the z-direction, in order to find the binding energy of the exciton. We used the finite difference technique. The wavefunction squared is shown in Fig. 3.6. We found that the binding energy of the exciton for the InAs/InP rectangular QWRs depends weakly on the height of the flat QWR. When the wire width is equal to 180 Å, which corresponds to the experimental value, the binding energy of the electron-hole pair is 14.14 meV and 13.35 meV for 5ML and 10ML, respectively. In the case of the V shaped $GaAs/Al_{0.4}Ga_{0.6}As$ QWR the difference is more pronounced. When the wire height is 10 nm and base length 20 nm and 40 nm, the Coulomb interaction

between the electron and the heavy-hole is 18.73 meV and 15.58 meV, respectively.

In Ref. [51] results were reported of PL experiments from an array of self-assembled QWRs. The PL spectrum consists of several peaks that correspond to emission from QWR with different height, which can vary by a discrete number of monolayers. The relation between the wire heights and the individual peaks in the PL spectrum are unknown. But we know that the height of the QWR can only vary by a discrete number of monolayers, it gives us the exact freedom to shift the experimental data. In Ref. [134], it was proposed to shift the experimental data with 1 ML in comparison with the results presented in Ref. [51]. However, the calculated peak energies had also to be shifted up with 39 meV in order to obtain a good agreement. In the present calculations using parameters taken from Table 3.1 we also included the Coulomb interaction between the electron and the hole. The best agreement in the shape of the calculated curves in Fig. 3.7 with (solid curve) and without (dashed curve) inclusion of the Coulomb interaction is obtained when the experimental data are shifted by 2 ML in comparison with the results which were presented in Ref. [51]. The small disagreement can be explained for example by the size dependence of the bandgap in InAs/InP QWR [135] or by the uncertainty on the band offsets [98].

3.5 QUANTUM WIRE STATES IN A MAGNETIC FIELD

In this section we calculate the diamagnetic shifts for different directions of the magnetic field and compare with experimental measurements. In Fig. 3.8 we show the shift of the PL peaks in the InAs/InP QWR for the magnetic field applied along the z-direction. We compare our theoretical results, which are denoted by three different curves, with the experimental data of Ref. [134] for QWRs with heights equal to 3 and 4 ML and with width 180 Å. As the magnetic field increases, the wavefunctions are squeezed due to the extra confinement of the magnetic field. This squeezing leads to an increase in energy, as we see in Fig. 3.8. Up to 25 T a good agreement is obtained between the experimental points and the theoretical curves for the heights of 3 and 4 ML. The discrepancy between theory and experiment for both heights at 50 T is about 1 meV. The numerical results for the QWR with a height of 5 ML are also shown for comparison.

When the magnetic length is much larger than the exciton diameter, the effect of the magnetic field can be treated as a perturbation and the resulting diamagnetic shift can be expressed as $\Delta E = \beta B^2$, with the diamagnetic coefficient $\beta = e^2 < \rho >^2 /8\mu$, where μ is the reduced mass of electron and hole, and $< \rho >$ is the average quadratic distance between electron and hole. However,

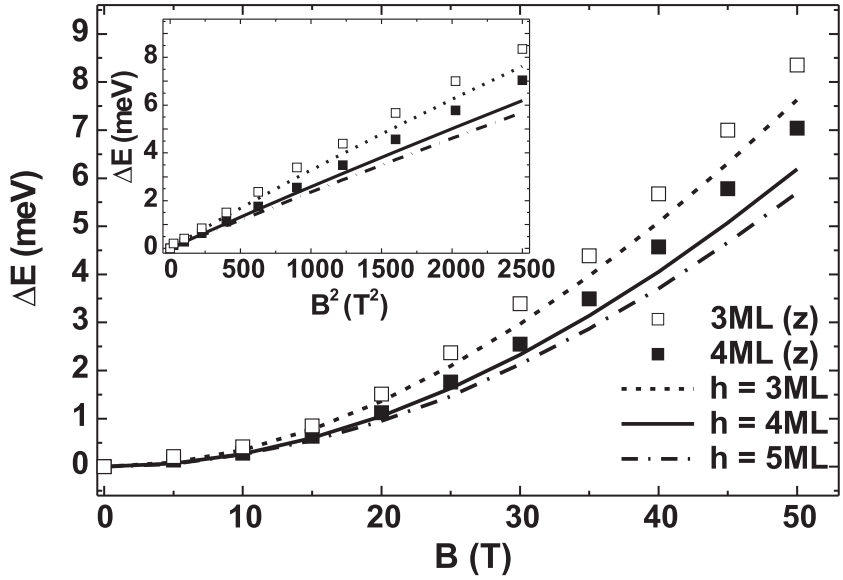

FIG. 3.8: The exciton diamagnetic shift as a function of magnetic field ($\mathbf{B}//\hat{z}$) for the InAs/InP QWR. The dashed, full and the short dash dot curves correspond to the numerical calculations done for different heights of the wire. The open squares and full squares represent the experimental data for the wire height 3 ML and 4 ML, respectively, with width equal 180 Å. The inset shows the same dependencies using a quadratic scale for the magnetic field B.

when the magnetic field is large enough, *i.e.* the magnetic length is comparable to the dimensions of the wire in the direction perpendicular to the applied field, the magnetic confinement becomes dominant and the parabolic dependence changes to a linear one $\Delta E = \hbar\omega_c^*$, with $\omega_c^* = eB/m^*$. From the inset in Fig. 3.8 we see the fully parabolic behavior of the diamagnetic shift energy of the experimental data as function of the magnetic field B. The theoretical curves show a very small deviation from a linear dependence.

Next, we investigated the effect of a magnetic field applied along the y-direction of the InAs/InP rectangular self-assembled QWR. Fig. 3.9 shows the experimental results [134] and the present theoretical calculations. Numerical results for three different heights of the wire are depicted. Again a fair agreement between the experimental points and the theoretical curves is obtained. A more pronounced difference of 1.5 meV for the height of 4 ML at 50 T is observed in comparison with the previous figure, while for 3 ML it is about 1 meV. The deviation of the theoretical calculations from a linear dependence is seen for B>25 T in the inset of Fig. 3.9. The expected magnetic field value for which the magnetic length equals the height of 4 ML is about 450 T (for 3

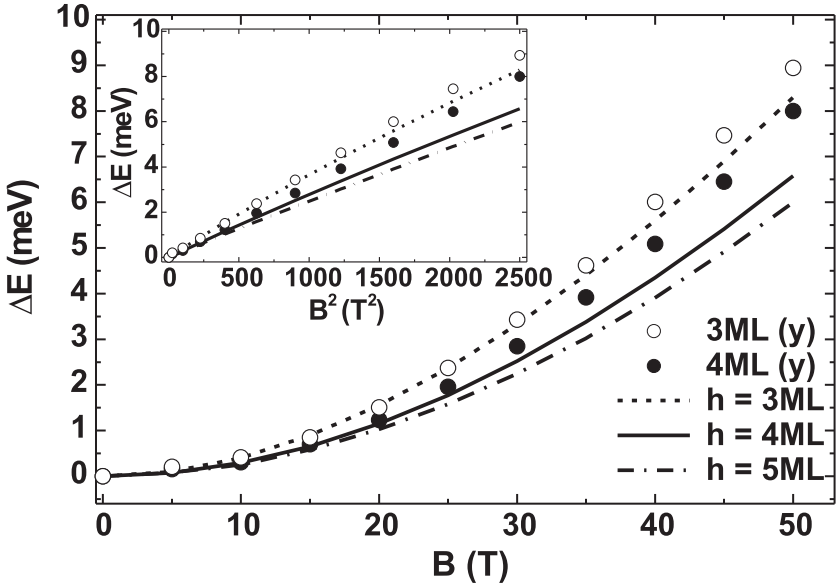

Fig. 3.9: The exciton diamagnetic shift as a function of magnetic field ($\mathbf{B}//\hat{y}$) for the InAs/InP QWR. The dashed, full and the short-dash-dotted curves correspond to our numerical calculations for different heights of the wire. The open circles and full circles represent the experimental data for the wire height 3 ML and 4 ML, respectively, with width equal 180 Å. The inset shows the the same dependencies with a quadratic scale of the magnetic field B.

ML it will be even larger) and thus much larger than 50 T. But because of the significant spread of the wavefunction into the barrier material of the QWR for such a narrow height we find already a deviation for smaller B-values. For instance, at the magnetic field 25 T the magnetic length is about 50 Å, which is the value of the wavefunction radii along the height direction [134].

The reason for the small quantitative deviation between the experimental data and the theoretical curves at high magnetic field along the z- and the y-direction might be due to the following:

1) We neglected the coupling between the heavy-hole and the light-hole which increases with increasing magnetic field. This causes only an insignificant deviation since the energy contribution of holes in the diamagnetic shift is very small in comparison with the contribution of the electron.

2) The variation of ε inside of the wire and in the barrier was not included. This can only slightly modify (1-2 meV) the Coulomb term of the ground state for zero magnetic field for this rectangular QWR. However, the Coulomb energy between the electron and hole in InAs/InP QWR practically does not change

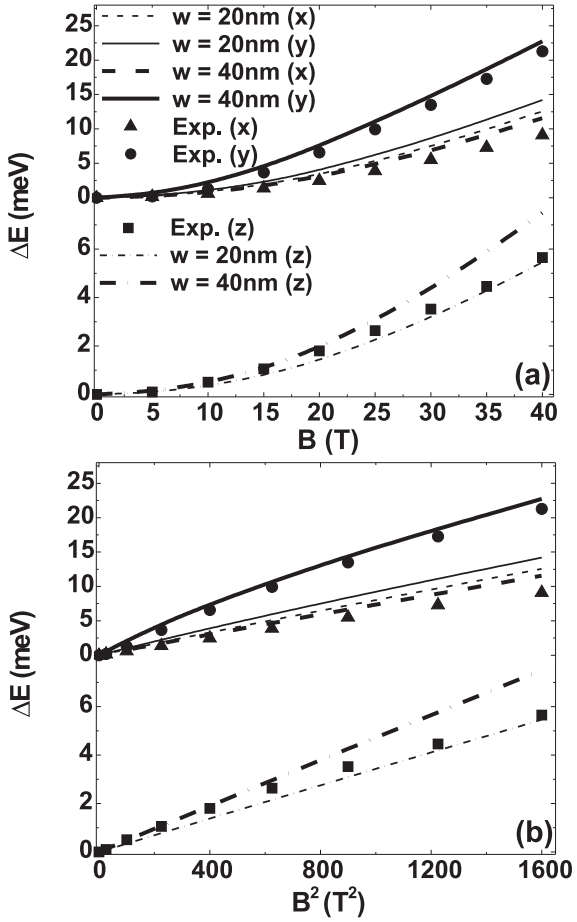

FIG. 3.10: The exciton diamagnetic shift as function of magnetic field B for the V-shaped GaAs/$Al_{0.4}Ga_{0.6}As$ QWRs with h=10 nm and for w=20 nm (thin curves) and w=40 nm (thick curves). The solid and dashed curves denote our numerical results for a magnetic field applied along the y- and x-direction, whereas the dash-dotted curves are for $\mathbf{B}//\hat{z}$. The experimental data [39] for the x-, y- and z-direction of the magnetic field are indicated by full triangulares, circles and squares, respectively. The results are represented for a linear (a) and quadratic (b) scale of B-scale.

for magnetic fields up to 50 T, as we will see later. Therefore, the diamagnetic shift is not affected by including spatial dependence of ε.

3) The most realistic reason for the discrepancy is that we assumed a rectangular shape for the QWR, which may not be the exact shape, and that we assumed an abrupt interface between the wire and the barrier material. But

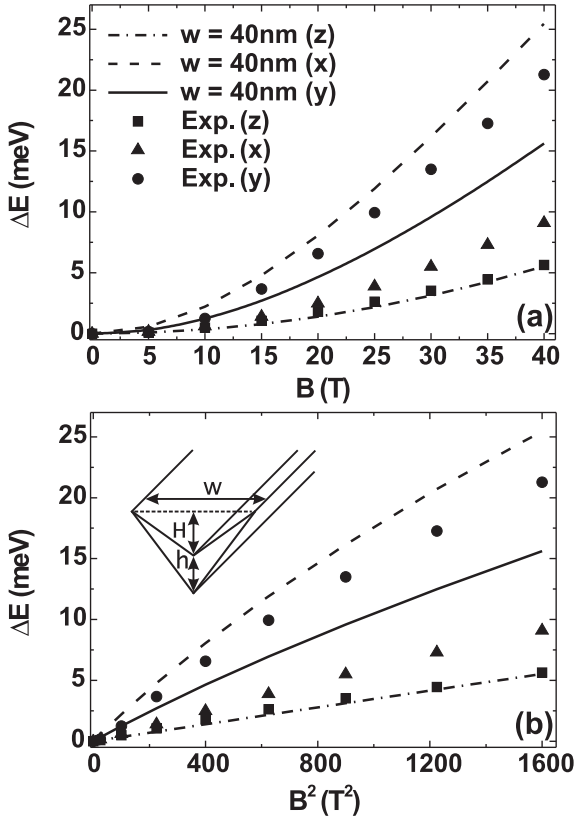

Fig. 3.11: The exciton diamagnetic shift as function of magnetic field B for V-shaped GaAs/$Al_{0.4}Ga_{0.6}As$ QWR with the profile shown in the inset (b). The heights of the QWR h=10 nm and H=19.3 nm, the base length w=40 nm. The solid and dashed curves denote our numerical calculation for the magnetic field applied along y- and x-direction, whereas the dash-dotted curves are for $\mathbf{B}//\hat{z}$. The experimental data [39] for the x-, y- and z-direction of the magnetic field are indicated by full triangulares, circles and squares, respectively.

because of the lack of detailed structural information of the QWR we are not able to do better without introducing extra unknown parameters.

Next, we present our results for the V-shaped GaAs/$Al_{0.4}Ga_{0.6}As$ QWRs. The parameters used in the simulations are shown in Table 3.1. Experimental results [39] were reported on vertically stacked triangular-shaped QWRs of which the average base length w and height h were reported to be 20 and 10 nm, respectively. The orientation of the magnetic field was applied along the x-, y- and z-direction. In Fig. 3.10 the diamagnetic shift of the exciton ground

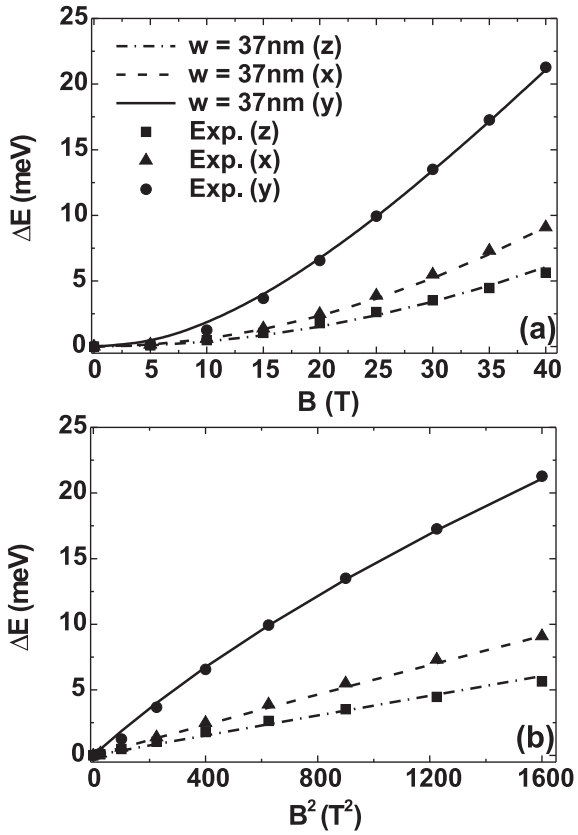

FIG. 3.12: The exciton diamagnetic shift as function of magnetic field B, for the V-shaped GaAs/$Al_{0.4}Ga_{0.6}As$ QWR with h=8.6 nm and w=37 nm. The solid and dashed curves denote numerical calculation for the magnetic field applied along y- and x-direction, whereas the dash dotted curves are for $\mathbf{B}//\hat{z}$. The experimental data [39] for the x-, y- and z-direction of the magnetic field are indicated by full triangulares, circles and squares, respectively.

state energy is plotted as a function of the magnetic field for all 3 cases. For comparison, we show theoretical calculations for the QWR with a height 10 nm and a base lengths of 20 and 40 nm, according to Fig. 3.2. Note again, that the diamagnetic shift reflects the lateral size of the wavefunction perpendicular to the magnetic field. Therefore in Fig. 3.10(a) we can observe a rather large difference for the numerical curves with base length 20 and 40 nm, when the magnetic field is applied in the y-direction, as well as in the z-direction (the base length is along the x-direction). And as expected, when the magnetic field is applied along the x-direction, the variation is small, even at 40 T it is less

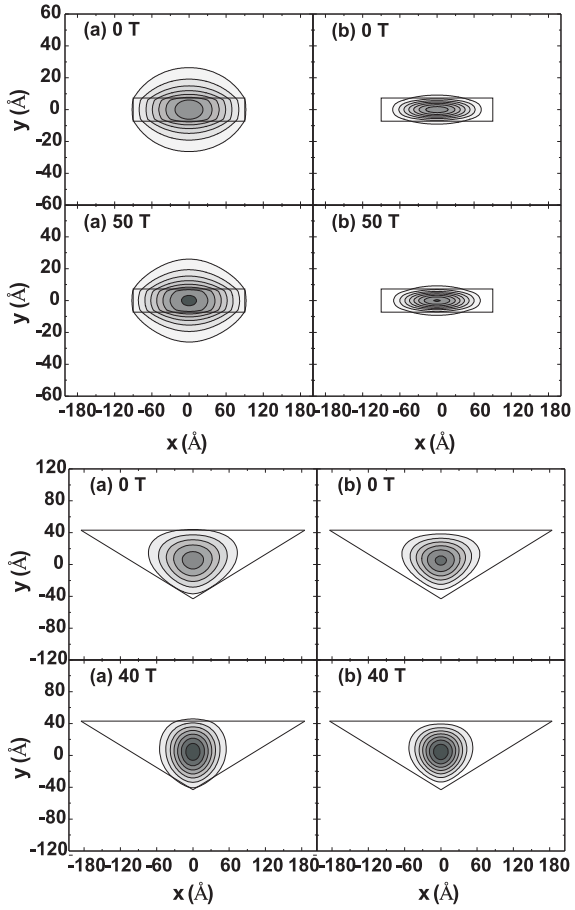

Fig. 3.13: The contour plot of the densities in the rectangular InAs/InP (upper figure) and the V-shape GaAs/$Al_{0.4}Ga_{0.6}As$ (lower figure) QWRs for electron (a) and heavy-hole (b) at magnetic field 0 T, 40 T and 50 T.

than 1 meV. We also see that the qualitative agreement with the experimental measurements is best for w=40 nm up to 20 T beyond which there are small deviations between theory and experiment which become substantial for $\mathbf{B}//\hat{z}$. Fig. 3.10(b) shows the magnetic dependencies of the GaAs/$Al_{0.4}Ga_{0.6}As$ QWR as a function of B^2. The deviation from a linear behavior is found for both the numerical and the experimental curves. This is not surprising, since the lateral size of the wire is relatively large, and so the magnetic field becomes important even at small values.

We also investigate another shape of the V-shaped GaAs/$Al_{0.4}Ga_{0.6}As$ QWR, as suggested by the high-resolution secondary electron image of the wire in

Ref. [39]. In Fig. 3.11 we compare our simulations for this new shape shown in the inset of Fig. 3.11(b). However, only for the z-direction a good fit with experimental measurements is obtained. While for the other two directions of the magnetic field, a large discrepancy between theory and experiment is found. Accordingly, it should be stressed, that the shape of the wire confinement plays a rather important role in the simulation of the magnetic properties for QWRs. The best fit between the experimental points and the numerical curves is obtained for the shape mentioned in Fig. 3.2 with h=8.6 nm and w=37 nm, as plotted in Fig. 3.12. As we can see from Figs. 3.12(a) and 3.12(b), full agreement is observed in the whole B region, for each direction of magnetic field. In comparison with the experimental determined dimensions of the QWR, the height of 8.6 nm is about the same as the aforementioned experimental average height of 10 nm, however the base length w=37 nm is found to be almost twice larger as mentioned in the experimental paper [39], namely 20 nm. However, from the high-resolution electron image of the wire in Ref. [39], the value of 20 nm as base length seems indeed to be a clear underestimation.

Next, we discuss the influence of the magnetic field on the exciton binding energy. In Fig. 3.13 we show the density for the electron and the heavy-hole for both InAs/InP and V-shaped GaAs/$Al_{0.4}Ga_{0.6}$As QWRs at different values of the magnetic field. Note that for both cases the effect of the applied field enhances the particle confinement into the wire, particulary for the wider V-shaped wires. This is also confirmed when comparing the Coulomb interaction. For the InAs/InP QWR the Coulomb contribution to the exciton energy is 13.79 meV and 13.89 meV, for 0 T and 50 T, respectively, while for GaAs/$Al_{0.4}Ga_{0.6}$As the difference is larger: 16.72 meV and 18.93 meV for 0 T and 40 T, respectively.

3.6 CONCLUSIONS

In summary, the excitonic properties in the presence of a magnetic field in InAs/InP self-assembled and V-shaped GaAs/$Al_{0.4}Ga_{0.6}$As QWRs were investigated theoretically. We include the effect of strain on the electronic structure of InAs/InP QWRs. The heavy-hole states are found to be the ground states for both types of wires. We show that the Coulomb interaction energy between the electron-hole pair has a relatively small value for the considered self-assembled QWRs and a very small change is observed, as the wire height increases. While for the V-shaped wire the Coulomb energy between the particles depends more strongly on the dimensions of the wire.

By calculating the effective potential in the rectangular InAs/InP QWR we confirm the spill-over effect in the case of flat wires with a height much narrowed as compared to its width. We also compare our theoretical results with the experimental measurements on the PL peak energies in the self-assembled

QWR. A good agreement is reached between them in the region of the height of the wire from 4 ML till 13 ML, when the width is fixed and taken equal to 180 Å.

Numerical simulations of the diamagnetic shift are performed for InAs/InP self-assembled QWR. Deviation from the experiment at B=50 T is found to be less than 1.5 meV, when the magnetic field is applied along the y-direction. For the z-direction of the magnetic filed it is even smaller than 1 meV. Calculations for three difference heights of the wire are compared. Further, the results for the diamagnetic shift for the GaAs/$Al_{0.4}Ga_{0.6}$As QWRs show a very good agreement between the experimental data and the theoretical curves, when the shape of the wire is considered as triangular. The non-parabolic dependence as a function of B starts at a small magnetic field value for both the experimental and the theoretical data, which is a consequence of the larger dimensions of the V-shaped wire.

Publications. The results in this chapter were published as:

- Y. Sidor, B. Partoens, and F. M. Peeters, *Exciton in a quantum wire in the presence of parallel and perpendicular magnetic fields*, Phys. Rev. B **71**, 165323 (2005).
- The paper Phys. Rev. B **71**, 165323 (2005) was also selected for the May 9, 2005 issue of Virtual Journal of Nanoscale Science & Technology.

4

Exciton confinement in InAs/InP quantum wires and quantum wells in the presence of a magnetic field

4.1 INTRODUCTION

The optical properties of quantum nanostructures have been intensively studied towards achieving novel device applications and because they provide the confinement for electrons and holes in such systems. The confinement of the electron and the hole is responsible for the properties of an exciton in such systems. Confinement of the particles depends on the size and shape of the semiconductor nanostructure. It can also be controlled through a selection of structure and barrier materials to obtain various band offsets. Moreover, the application of an external magnetic field can give important information about the carrier confinement.

The magnetoexcitons in a QWR have been theoretically investigated by a number of authors [75, 94, 95], as it was discussed in chapter 3 and Ref. [136]. An exciton in a QW in the presence of an external magnetic field has been intensively studied over the last decades. For the QW exciton in the presence of an in-plane magnetic field only a small number of studies have been published [137, 138] due to the increased complexity as a consequence of the breaking of the conservation of the total pseudo-momentum [139]. Most of the investigations on magnetoexcitons were restricted to the case when the magnetic field is applied along the growth direction (see, for example, Refs. [140–142]). However, all the mentioned studies of the exciton in a perpendicular

magnetic field did not include local QW width fluctuations, where excitons (as well as trions and biexcitons) can be trapped [143–146]. Such fluctuations can induce an additional weak lateral confinement which leads to the confinement of the particles in all three dimensions, *i.e.* a shallow quantum structure is formed.

One of the promising fabrication methods made it possible to create self-organized nanostructures, formed during the initial stage of heteroepitaxial growth in lattice-mismatched systems. Deposition of InAs on InP by molecular beam epitaxy can lead to a QW or self-assembled quantum wires and dots, depending on the growth conditions. Self-assembled InAs/InP quantum wires and dots are promising candidates for optical applications at telecommunication wavelengths 1.3 and 1.55 μm [8, 134, 147, 148], among other things because of the enhanced charge confinement as compared to QW. In this chapter we investigate the charge confinement in InAs/InP QW and self-assembled InAs/InP QWRs. Both are designed to emit PL around 1.3 μm at room temperature. We report temperature, laser power, and pulsed magnetic field dependence of the PL spectrum. We perform the calculations within the single band effective mass approximation but including strain effects and conduction band nonparabolicity. We study the exciton energy shift of QWR and QW with a local thickness fluctuation in magnetic fields up to 50 T and compare theoretical and experimental data.

4.2 THEORETICAL MODEL

In our calculations, we model the quantum wire as a 2D quantum box with height h and width w, as shown in Fig. 4.1(a) and follow our earlier theoretical approach of Ref. [136]. We identify the crystallographic axes [110], [001], and [1$\bar{1}$0] of the InAs/InP self-assembled QWR [8, 134, 136] with the x, y and z axes of the wire, and the z axis of the QW with the growth direction of the well (see Fig. 4.1). For the narrow quantum well of width h we include a local circular well width fluctuation of 1 ML with radius R, as illustrated in Fig. 4.1(b).

The single-band effective mass theory is used to calculate the exciton states in both QW and QWR. In our previous work on InAs/InP self-assembled QWR (see chapter 3) we presented the basic equations of the QWR in the presence of parallel and perpendicular magnetic fields. In the present work we extend that work to QW in the presence of parallel and perpendicular magnetic fields and when a local well width fluctuation is present. The components of magnetic field $\mathbf{B}$ perpendicular and parallel to the plane motion: $\mathbf{B}=\mathbf{B}_{\perp}+\mathbf{B}_{||}$, where $\mathbf{B}_{\perp}//\hat{z}$ and $\mathbf{B}_{||}\perp\hat{z}$. Without going into a detailed description of the basic equations for the QW in the presence of perpendicular and parallel magnetic fields, three points have to be stressed:

(1) The effect of strain on the electron and the hole confinement potentials

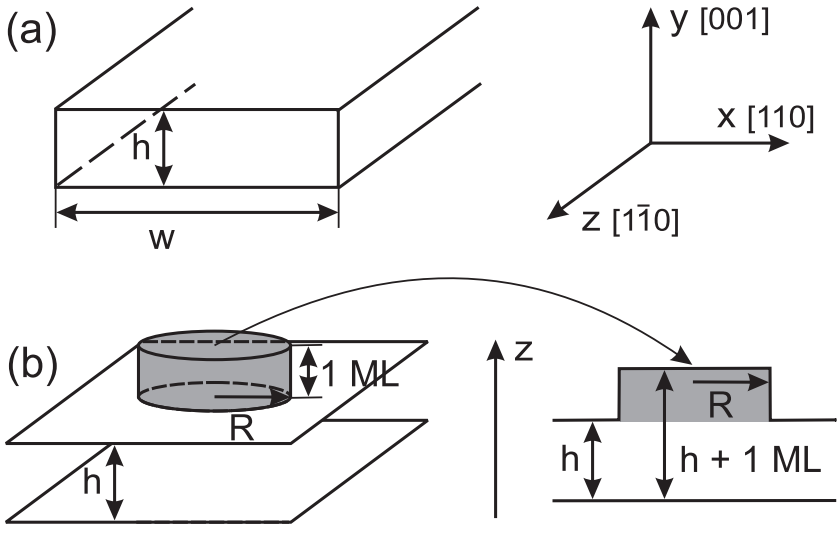

Fig. 4.1: Schematics drawing of (a) our model of rectangular self-assembled InAs/InP quantum wire with height h and width w, and (b) our model of two-dimensional InAs/InP quantum well with width h. The quantum well width fluctuation of 1 ML and radius R is modeled by the gray area.

was included [71, 149] by calculating the hydrostatic strain in the conduction and the valence bands of the QW, and the shear separation potential in the valence band of the QW. The heavy-hole is found to be the ground state in the InAs/InP QW due to the shear separation potential. We include the effect of band nonparabolicity [150] in our calculations by using an energy dependent electron mass

$$m_{nonp.e} = m_e(1 + \alpha E), \tag{4.1}$$

where m_e and $m_{nonp.e}$ is the bulk and nonparabolic electron mass, respectively, α is the nonparabolicity parameter, which we assume to be [151, 152] α=1.4 eV^{-1}, and E is the energy of the electron obtained by solving the single particle Schrödinger equation using the electron bulk mass.

(2) In a parallel magnetic field ($\mathbf{B}_{||}\perp\hat{z}$) we introduce the center-of-mass (c.m.) $\mathbf{R}$=$(m_e\mathbf{r}_e+m_h\mathbf{r}_h)/M$ and relative motion coordinates $\mathbf{r}$=$\mathbf{r}_e$-$\mathbf{r}_h$ to describe the exciton state in the QW, where m_e (m_h) denotes the electron (hole) mass, $\mathbf{r}_e$ ($\mathbf{r}_h$) is the electron (hole) coordinates in the xy-plane and M=m_e+m_h is the total mass of the exciton. In the case of a parallel magnetic field we compare the numerical results for different well width, but we do not include the local QW width fluctuation (see the dark region in Fig. 4.1(b)). This is motivated by the fact that the magnetic field mainly influences the extent of the

exciton wavefunction in the z-direction while a local well width fluctuation will trap the exciton and shift its energy slightly which will have a very weak magnetic field dependence. This leads to the following Hamiltonian for the exciton

$$\begin{aligned} H &= -\frac{\hbar^2}{2\mu}\nabla_r^2 - \frac{\hbar^2}{2M}\nabla_R^2 + \frac{i\hbar eB_{||}}{c}\left(\frac{z_e}{m_e}+\frac{z_h}{m_h}\right)\nabla_{r_y} + \frac{i\hbar eB_{||}}{Mc}\left(z_e - z_h\right)\nabla_{R_y} \\ &\quad + \frac{e^2B_{||}^2}{2c^2}\left(\frac{z_e^2}{m_e}+\frac{z_h^2}{m_h}\right) - \nabla_{ze}\frac{\hbar^2}{2m_e(z_e)}\nabla_{ze} - \nabla_{zh}\frac{\hbar^2}{2m_h(z_h)}\nabla_{zh} + V_e(z_e) \\ &\quad + V_h(z_h) - \frac{e^2}{\varepsilon\sqrt{r^2+(z_e-z_h)^2}}, \end{aligned} \tag{4.2}$$

where $\mu{=}m_em_h/M$ denotes the exciton reduced mass in the xy-plane, $\mathbf{p}{=}{-}i\hbar\nabla_r$ is the relative mass momentum in the xy-plane, $\mathbf{P}{=}{-}i\hbar\nabla_R$ is the exciton c.m. momentum in the xy-plane, $V_e(z_e)$ ($V_h(z_h)$) the confinement potential of the electron (hole) along the growth direction of the QW, e is the free-electron charge and ε is the dielectric constant. Further, the total in-plane pseudo-momentum $\mathbf{\Pi}_{||} = \hbar\mathbf{K}_{||}$ is an exact integral of motion [139] which implies that the slow motion of the c.m. is decoupled from the fast relative motion in Eq. (4.2). Therefore the exciton wavefunction can be written as

$$\Phi(\mathbf{R},\mathbf{r},z_e,z_h) \rightarrow \exp\left[i\mathbf{K}_{||}\cdot\mathbf{R}\right]\varphi(\mathbf{r},z_e,z_h). \tag{4.3}$$

Because of the strong confinement along the z-direction, we are allowed to separate the lateral motion in the xy-plane from the z motion. Further, we assume that the confinement interaction is larger than the Coulomb (*i.e.* exciton) interaction which allows us to use the adiabatic approximation

$$\varphi(\mathbf{r},z_e,z_h) = \varphi_e\left(z_e\right)\varphi_h\left(z_h\right)\exp\left[-\alpha r^2\right], \tag{4.4}$$

where $\varphi_e(z_e)$ ($\varphi_h(z_h)$) is the electron (hole) wavefunction that is the solution of Eq. (4.3) when neglecting the Coulomb interaction. The wavefunction for the relative motion of the exciton is approximated by a Gaussian, where α is a variational parameter. In the final step, we average the kinetic part and the Coulomb interaction part in the exciton Hamiltonian (see Eq. (4.3)) using the above wavefunction, and minimize the total exciton energy with respect to α, and obtain the exciton energy.

(3) For the perpendicular magnetic field direction ($\mathbf{B}_\perp // \hat{z}$) the local well width fluctuations will influence the diamagnetic shift much more. The reason being that the exciton will be trapped in such local well width fluctuations and for such a weakly confined exciton there will be a competition between the magnetic confinement and the localization due to well width fluctuations.

A local increase of the well width results into a lower zero point energy for the electron and the hole which can be viewed as an attractive potential well in the plane of the QW [143–146]. For example for h=3 ML and a local well with increase of 1 ML the difference in zero point energy for the electron (hole) is ΔV_e=40 (50) meV. The corresponding results for h=4 ML is ΔV_e=39 (36) meV. Normally, one would expect a larger difference in zero point energy for the electron than for the hole, which is the case for h=4 ML. But for the very narrow QW the electron ground state energy is close to the conduction band offset causing ΔV_e<ΔV_h, as we found for h=3 ML. We use a mean field theory in the Hartree approximation to describe our system. Due to the axial symmetry of the problem the wavefunction of the particles can be written as $\Psi(\rho,z,\theta)$=$\psi(\rho,z)e^{-il\theta}$. The electron and the heavy-hole states in the QW are obtained by solving the following 2D Schrödinger equations

$$\Big[-\nabla_{ze}\frac{\hbar^2}{2m_e(z_e)}\nabla_{ze}-\frac{\hbar^2}{2m_e}\left(\nabla^2_{\rho e}+\frac{1}{\rho_e}\nabla_{\rho e}\right)+\frac{\hbar^2}{2m_e}\frac{l_e^2}{\rho_e}-\frac{l_e}{2}\frac{\hbar eB_\perp}{m_e c}$$
$$+\frac{e^2B_\perp^2\rho_e^2}{8m_ec^2}+V_e(\rho_e,z_e)+U_{eff}(\rho_e,z_e)\Big]\psi_e(\rho_e,z_e)=E_e\psi_e(\rho_e,z_e), \quad (4.5)$$

$$\Big[-\nabla_{zh}\frac{\hbar^2}{2m_h(z_h)}\nabla_{zh}-\frac{\hbar^2}{2m_h}\left(\nabla^2_{\rho h}+\frac{1}{\rho_h}\nabla_{\rho h}\right)+\frac{\hbar^2}{2m_h}\frac{l_h^2}{\rho_h}+\frac{l_h}{2}\frac{\hbar eB_\perp}{m_h c}$$
$$+\frac{e^2B_\perp^2\rho_h^2}{8m_hc^2}+V_h(\rho_h,z_h)+U_{eff}(\rho_h,z_h)\Big]\psi_h(\rho_h,z_h)=E_h\psi_h(\rho_h,z_h), \quad (4.6)$$

where $\rho_{e(h)}$=$\sqrt{x^2_{e(h)}+y^2_{e(h)}}$, $V_{e(h)}(\rho_{e(h)},z_{e(h)})$ is the confinement potential of the electron (hole) which takes into account the QW width fluctuation, and $U_{eff}(\rho_{e(h)},z_{e(h)})$ is the effective Hartree potential felt by the electron (hole)

$$U_{eff}(\rho_{e(h)},z_{e(h)})=-\frac{e^2}{\varepsilon}\int\rho_{h(e)}d\rho_{h(e)}\int dz_{h(e)}$$
$$\int d\theta_{h(e)}\frac{|\psi_{h(e)}(\rho_{h(e)},z_{h(e)})|^2}{\sqrt{\rho_e^2+\rho_h^2-2\rho_e\rho_h\cos(\theta_e-\theta_h)+(z_e-z_h)^2}}. \quad (4.7)$$

To solve self-consistently the single-particle differential equations (4.5) and (4.6), we have to evaluate a three-fold Hartree integral which is given by Eq. (4.7). The integration over the angle θ was performed analytically and the part which contains the ρ- and z-dependence was performed numerically using the logarithmically weighted method [153]. In the final step we calculate the exciton energy as follows

$$E_{ex}=E_e+E_h+\frac{e^2}{\varepsilon}\int d\rho_e dz_e d\theta_e d\rho_h dz_h d\theta_h\frac{|\psi_e(\rho_e,z_e)|^2|\psi_h(\rho_h,z_h)|^2}{\sqrt{(\rho_e-\rho_h)^2+(z_e-z_h)^2}}, \quad (4.8)$$

where the last term also equals $(E_e^{'} + E_h^{'} - E_e - E_h)/2$, with the single particle energies $E_e^{'}$ and $E_h^{'}$ obtained from Eqs. (4.5) and (4.6) by neglecting the Hartree potential. Note, that this term defines the Coulomb interaction energy, but its value has the opposite sign (the Coulomb interaction energy is negative).

The input parameters used in our simulations for the InAs/InP material are taken from Ref. [136], except for the nonparabolicity parameter α.

4.3 EXPERIMENTAL SETUP

The samples were grown by solid-source MBE. For the QW sample, 4 ML of InAs were deposited (1 ML is 3 Å), followed without interruption by a 20 nm thick InP barrier, both at 485°C. The fast growth rate of 1 ML/s, and the absence of an interrupting between InAs and InP growth, inhibits the kinetics and thus no wires were formed. This is confirmed by the reflection high-energy electron diffraction (RHEED) signal, which showed a 2x4 pattern during InAs growth, corresponding to a 2D layer. For the QWRs sample, 1.7 ML of InAs was deposited at 0.1 ML/s and 515°C in a pulsed dynamic way (pulsed In sequence: 1s ON; 2s OFF). The deposition of InAs was interrupted immediately after the change from 2D to 3D growth was observed in the RHEED pattern. Then, the sample was kept 1 minute under As pressure and finally covered by a 20 nm thick InP layer grown at 1 ML/s. PL-measurements were performed in a He bath cryostat at 4.2 K and in a He flow cryostat (20-200 K). Excitation of the samples was achieved by a solid-state laser operating at 532 nm via a 200 m core optical fiber. The laser power was controlled between 0.6 and 600 mW by neutral density filters corresponding to power densities at the sample from 0.06 to 60 $W*cm^{-2}$. The luminescence, collected by six surrounding fibers, was analyzed in a 0.25 m spectrometer with a liquid-nitrogen cooled InGaAs detector. A magnetic field of 50 T is obtained by pulsed fields. During a 25 ms magnetic field pulse, up to 23 spectra were taken at various fields with a photon integration time of 0.2 ms each.

4.4 COMPARISON OF VERTICAL CONFINEMENT IN QUANTUM WIRES AND WELLS

The QWR structure shows three distinct PL peaks (see the thick dashed (blue) curve in Fig. 4.2). From our previous theoretical study of such quantum wires (see chapter 3) we know that they correspond to a wire height of 4-6 ML and a width of 180 Å. The temperature dependence of these three PL lines is similar to that reported by Fuster *et al.* [154] on a similar sample, revealing a unipolar electron escape towards the barrier at room temperature. We also note that in our sample the intensity of the low-energy peak originating from the 6 ML

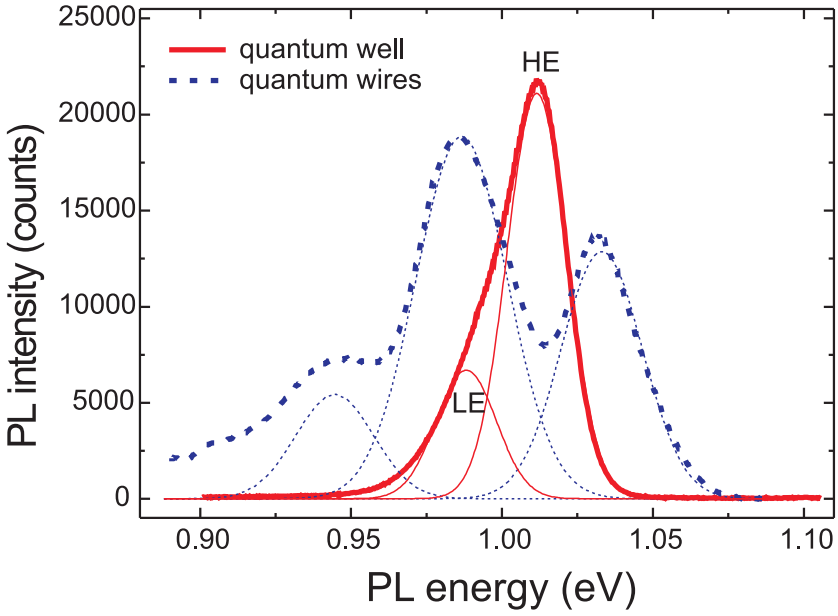

Fig. 4.2: Photoluminescence spectra of the InAs/InP quantum well and wires at 20 K. The thick full (red) and dashed (blue) curves correspond to the PL energies of the well and wires, respectively. The thin full and dashed lines are Gaussian fits to the spectrum.

thick wires increases up to 80 K evidencing the occurrence of phonon assisted tunneling or recapture of carriers that have thermally escaped from thinner wires [154].

In Fig. 4.3 we compare the theoretical results of the exciton diamagnetic shift ($\Delta E = E(B) - E(0)$) in the InAs/InP QWR, which are denoted by four curves corresponding to the wire height h=3-6 ML and width w=180 Å, with the experimental data, which are denoted by the three different symbols. The numerical calculations for the electron parabolic effective mass and the electron nonparabolic effective mass are shown (see Fig. 4.3(a) and Fig. 4.3(b)). Note that the experimental data in Fig. 4.3 differ slightly from those reported in our previous works (see chapters 2 and 3) due to different growth conditions of the QWR. But the theoretical results for the electron parabolic effective mass, when height h equals 3-5 ML, are the same as given in chapter 3. The theoretical results for the bulk (parabolic) mass of the electron in Fig. 4.3(a) only slightly differ from the one in Fig. 4.3(b). However, in the case of parabolic electron effective mass we obtained a better agreement between the theoretical result and experimental data of the same height h, as compared to the case of nonparabolic electron effective mass. The best agreement in the whole B

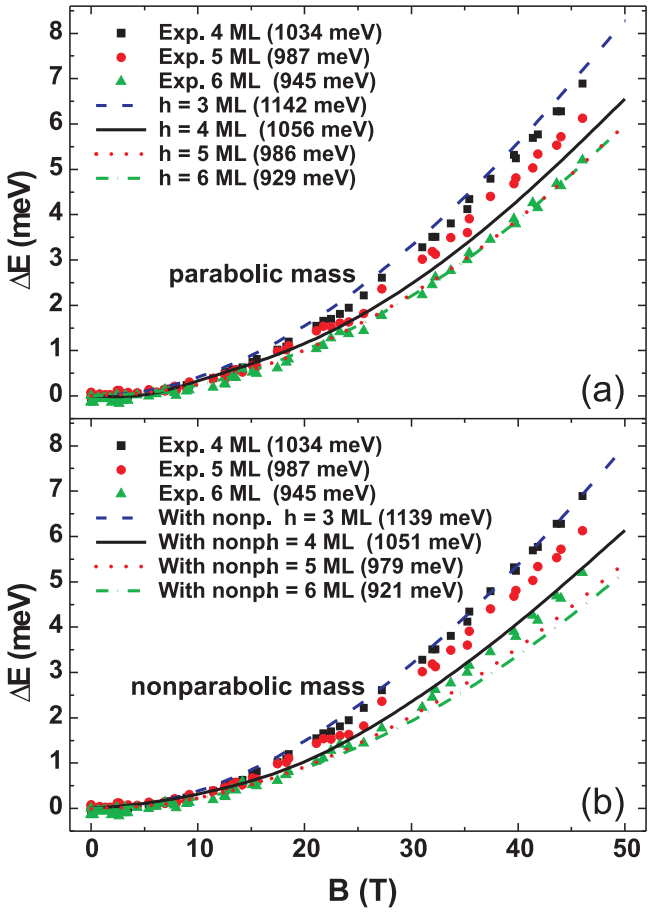

FIG. 4.3: The exciton diamagnetic shift as a function of magnetic field (**B**//[110]) for InAs/InP quantum wires. The dashed (blue), full (black), dotted (red) and short dash-dot (green) curves correspond to our numerical results with parabolic mass of the electron (a) and when the effect of band nonparabolicity is included (b) for different heights of the wire. The full squares (black), circles (red) and triangles (green) represent the experimental data for the wire height 4, 5 and 6 ML, respectively, and width equal to 180 Å. The value of the experimental and the calculated PL energies in the absence of the magnetic field are given between brackets.

region is found when h=6 ML (compare the dashed-dot (green) curve with the full triangles (green) in Fig. 4.3(a)). For the height of 4 and 5 ML we see a fair agreement in Fig. 4.3(a) between the experimental points and the theoretical curves. At 45 T a discrepancy of 1.3 meV for h=4 ML and 1.0 meV for h=5 ML is observed. The reason for these small deviations is probably due

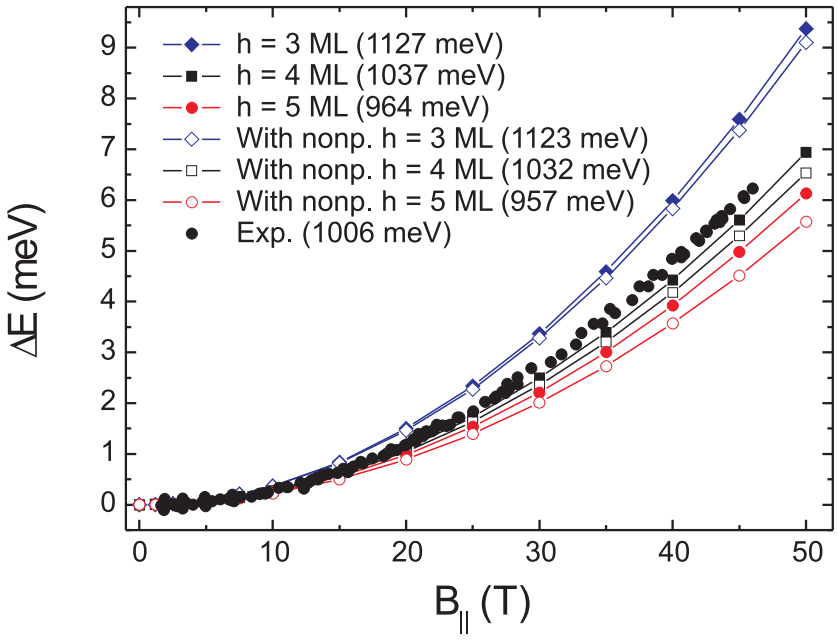

Fig. 4.4: The exciton diamagnetic shift as a function of parallel magnetic field ($\mathbf{B}_{||} \perp \hat{z}$) for InAs/InP quantum wells. The curves with the open and closed symbols correspond to the exciton diamagnetic shift with and without taking into account the effect of band nonparabolicity for the electron, respectively. The curves with the diamonds (blue), squares (black) and circles (red) correspond to the quantum well with width of 3, 4 and 5 ML, respectively. The full circles (black) correspond to the experimental data. The value of the experimental and the calculated PL energies in the absence of the magnetic field are given between brackets.

to the fact that we assume a rectangular shape of the QWR in our theoretical model, which may not be the exact experimental shape [134]. Comparing the theoretical and experimental PL energies for different heights of the wire at zero magnetic field in Fig. 4.3(b), we see a difference of about 24 meV for the wire height h=6 ML, and a smaller difference for h=4-5 ML. When we compare the computed PL energies with the experimental PL energies for the parabolic mass of the electron in Fig. 4.3(a), we found that the 5 ML computed PL energy $\mathrm{E}_{PL(5ML)}$=986 meV is closer to the experimental one $\mathrm{E}_{PL(Exp5ML)}$=987 meV, as compared to the calculated and experimental PL energies for the height of 4 ML, $\mathrm{E}_{PL(4ML)}$=1056 meV and $\mathrm{E}_{PL(Exp4ML)}$=1034 meV, and the height of 6 ML, $\mathrm{E}_{PL(6ML)}$=929 meV and $\mathrm{E}_{PL(Exp6ML)}$=945 meV.

When the magnetic field is applied along the [110] direction, the confinement properties in the direction of the wire height are investigated. The diamagnetic shift in the range of B between 0 and 50 T increases with decreasing wire height

Table 4.1: Wavefunction radii for the electron (ρ_{gr_e}), the heavy-hole ($\rho_{gr_{hh}}$) and the exciton ($\rho_{gr_{exc}}$) along the *growth* direction of the InAs/InP quantum well (z-direction) with width of 3-5 ML and the InAs/InP quantum wire ([001] direction) with height of 4-6 ML.

	ρ_{gr_e} (Å)	$\rho_{gr_{hh}}$ (Å)	$\rho_{gr_{exc}}$ (Å)
QW 3 ML	9.0	2.4	9.3
QW 4 ML	7.5	2.5	7.9
QW 5 ML	6.9	2.7	7.4
QWR 4 ML	7.7	2.6	8.1
QWR 5 ML	7.0	2.7	7.5
QWR 6 ML	6.7	3.0	7.3

for both theoretical and experimental results shown in Fig. 4.3. This indicates a larger exciton wavefunction extent for smaller wires. To illustrate this, we calculated the wavefunction radii in the InAs/InP QWR theoretically. In Table 4.1 we present a list of the wavefunction radii for the electron and heavy-hole along the [001] direction of the QWR with h=4-6 ML, where we define the particle radius as the average quadratic distance along the [001] direction of the wire $\rho_{gr} = \sqrt{< y^2 >}/2$. Note, that the electron extent ρ_{gr_e} decreases with increasing well width, while the opposite behavior is found for the hole extent $\rho_{gr_{hh}}$. The unusual behavior for the electron extent is a consequence of the electron wavefunction spill-over effect. As a result also the exciton size increases with decreasing well width (see the data for $\rho_{gr_{exc}}$ in Table 4.1).

In Fig. 4.4 we examine the exciton diamagnetic shift for the InAs/InP quantum well, when the magnetic field is applied perpendicular to the z-direction. The PL experiments show that the QW structure clearly has a main peak, high-energy (HE) peak, and a second PL peak, low-energy (LE) peak, about 20 meV below (see the full (red) curves Fig. 4.2). We compare the theoretical results for the QW with widths equal to 3, 4 and 5 ML, with the experimental data of the HE peak denoted by the full circles (the diamagnetic shift of the LE peak was not measured). Band nonparabolicity has a small effect on the results (compare the curves with open and closed symbols in Fig. 4.4). The effect of band nonparabolicity is to increase the electron effective mass. The exciton diamagnetic shift is inversely proportional to the reduced mass of the electron and heavy-hole, therefore the exciton diamagnetic shift when including the nonparabolic electron mass is smaller than the one with the bulk electron mass. Up to $B_{||}$=30 T the calculated diamagnetic shift energies (when the effect of the nonparabolicity is included) for the QW with width of 4 ML is in close agreement with the experimental data. At 45 T the discrepancy between theory and experiment is only 0.7 meV. When comparing the calculated PL energies at zero magnetic field (when including band nonparabolicity), we

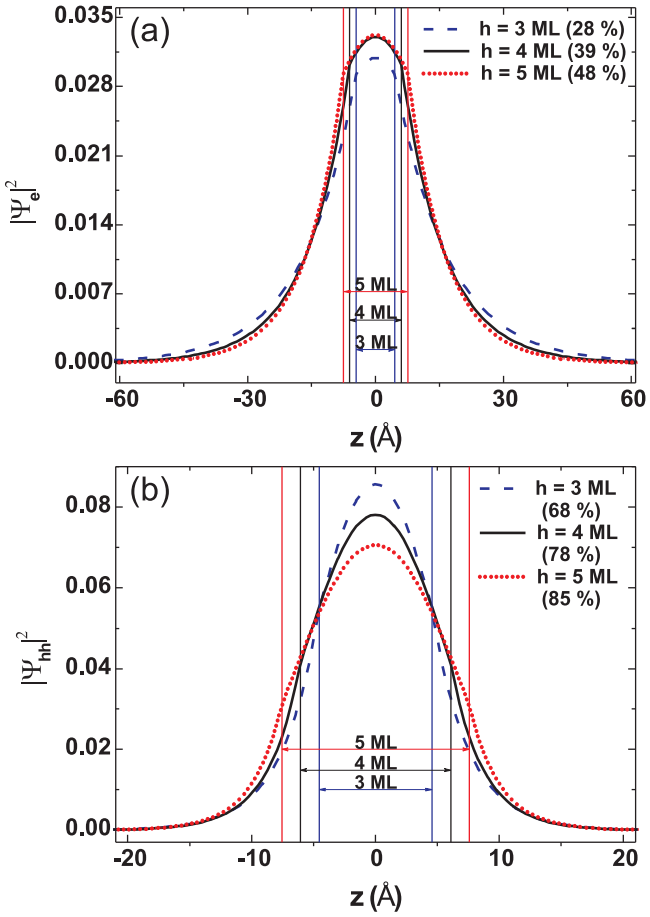

Fig. 4.5: The probability density for the electron (a) and the heavy-hole (b) along the growth direction (z-direction) in a InAs/InP quantum well with widths 3, 4 and 5 ML (the dashed (blue), full (black) and dotted (red) curves, respectively). The probability of the electron and the heavy-hole to be inside the quantum well is indicated between brackets in %.

found that the 4 ML results $E_{PL(4ML)}$=1032 is closest to the experimental PL energy $E_{PL(Exp)}$=1006 meV (we assumed a bulk band gap energy for InAs of E_g=472 meV). This is consistent with the fact that the 4 ML results gives also the best agreement for the exciton diamagnetic shift and with the intended thickness of the QW in the MBE growth. From Fig. 4.4 we see that the calculated diamagnetic shift increases with decreasing well width. The diamagnetic shift is determined by the lateral size of the wavefunction perpendicular to the

Table 4.2: The exciton reduced mass (m_0 is the vacuum electron mass) along the z-direction of the InAs/InP quantum well and quantum wire with and without including the effect of band nonparabolicity.

	μ_{par} (m_0)	μ_{nonp} (m_0)
QW 3 ML	0.042	0.051
QW 4 ML	0.036	0.047
QW 5 ML	0.033	0.044
QWR 4 ML	0.037	0.047
QWR 5 ML	0.033	0.044
QWR 6 ML	0.031	0.042

magnetic field. In the case of parallel magnetic field it reflects the exciton extent along the z-direction of the QW. We found a large wavefunction spill-over in the growth direction of the well.

Fig. 4.5 shows the density of the electron (when the effect of band nonparabolicity is included) and heavy-hole along the z-direction. Because the QW is very thin and the electron mass is at least six times smaller along the z-direction than the heavy-hole mass, the largest part of the electron density is in the barrier of the QW in contrast to the heavy-hole density, which is mostly situated in the well. The wavefunction radii for the particles along the growth direction of the QW ($\rho_{gr} = \sqrt{< z^2 >}/2$) with h=3-5 ML are listed in Table 4.1. When compare to the theoretical results of the exciton extent in the QWR with the one in the QW (see Table 4.1), we found that the extent of the electron, heavy-hole and exciton along the z-direction for the QW with h=4 and 5 ML is slightly smaller than the corresponding extent along the [001] direction for the QWR with h=4 and 5 ML. The electron and the exciton wavefunction spill-over was found in both QW and QWR, but not for the heavy-hole (see Table 4.1), which proves that the exciton extent is predominantly determined by the electron extent. We also found that along the z-direction of the QW with different h the effective mass of the exciton is different. From Table 4.2 we can see a larger exciton effective mass μ for the thinner well [155] (we also give a list of exciton effective masses for the QWR), where for the QW

$$\frac{1}{\mu} = \int dz_e dz_h |\varphi_e(z_e)|^2 |\varphi_h(z_h)|^2 \left(\frac{1}{m_e(z_e)} + \frac{1}{m_h(z_h)} \right), \qquad (4.9)$$

and for the QWR

$$\frac{1}{\mu} = \int dx_e dy_e dx_h dy_h |\Psi_e(x_e, y_e)|^2 |\Psi_h(x_h, y_h)|^2 \left(\frac{1}{m_e(x_e, y_e)} + \frac{1}{m_h(x_h, y_h)} \right). \qquad (4.10)$$

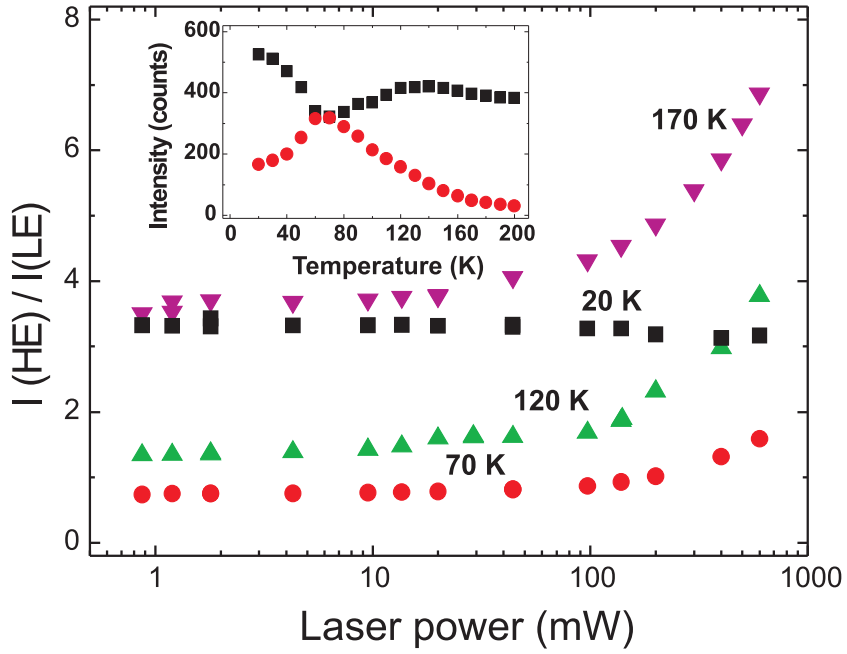

Fig. 4.6: Laser power dependence of the ratio of the intensities of the HE and LE peaks of the quantum well at the different temperatures denoted by the different symbols. At 20 K this ratio remains constant with varying laser power. With increasing temperature the laser power dependence becomes more pronounced. The inset shows the temperature dependence of the absolute intensities of the HE (squares (black)) and LE (circles (red)) peaks.

The QW shows a second PL peak about 20 meV below the main peak (Fig. 4.2). This LE peak can be attributed to a monolayer fluctuation in the QW thickness. The observation of the LE shoulder is very surprising since QW excitons can typically migrate to regions with the largest well thickness (and so, to regions of the lowest confinement energy) at helium temperature. We assume that the exciton energy state corresponding to the main PL peak (HE peak) is a local minimum originating from the predominant thickness of h=4 ML, while the LE state is attributed to 5 ML thickness fluctuations that is less abundant (Figs. 4.7(a) and 4.7(b)). The ratio of the intensities of the 4 and 5 ML peaks does not depend on the laser power at 20 K (see Fig. 4.6). Hence, we conclude that the charge carriers in the QW are trapped by thickness fluctuations and that there is no coupling between the optically active 4 ML and 5 ML fluctuations. Therefore, these states are spatially well separated. Indeed, charge carriers that are in a region of 4 ML well thickness, that is close to 5 ML fluctuation, would not significantly be optically active since such

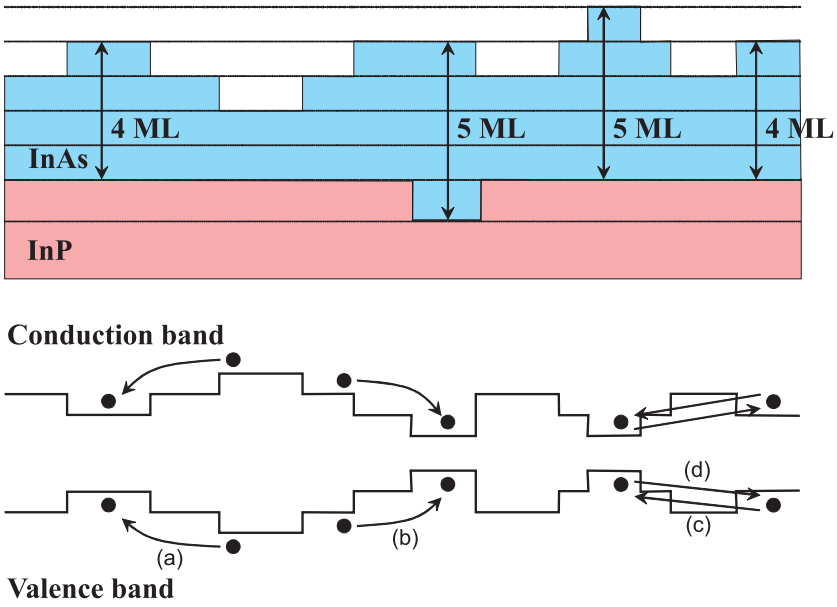

FIG. 4.7: Schematic diagram of the thickness fluctuations within the quantum well (top) and the band structure (bottom). Most excitons can freely move to the most abundant 4 ML fluctuation at all temperatures (a), and some excitons get trapped by a 5 ML fluctuation (b). At moderate temperature excitons are able to migrate from the 4 ML to the 5 ML state (c). At temperatures above 70 K, thermal redistribution causes excitons to migrate from the 5 ML to the 4 ML state (d).

charge carriers would easily migrate towards the 5 ML fluctuation. Since there is no coupling at 20 K, the ratio of the peak intensities reflects the ratio of the number of corresponding states: there are 3.3 times more optically active 4 ML states than 5 ML states. When temperature T increases, the 4 ML peak (HE peak) looses intensity in favor of the 5 ML peak (LE peak), as shown in the inset of Fig. 4.6. So, in the QW we find a phonon assisted tunneling or the recapture of carriers that have thermally escaped from the thinner regions of the QW (see Fig. 4.7(c)). For temperatures above about 70 K, the 4 ML peak regains some of its relative intensity as the laser power increases (see Fig. 4.6), indicating that the thermal redistribution rate is smaller than the rate at which the charge carriers are injected at elevated laser power. The 5 ML peak has a maximum relative intensity at 70 K, after which the thermal activation to the 4 ML fluctuations starts to dominate (Fig. 4.7(d)). At 170 K the intensity ratio is the same as at 20 K at low laser power, indicating that charges can now move around freely, and that their distribution reflects the density of states (*i.e.* the intensity ratio equals the ratio of available states). 170 K corresponds quite well with the 20 meV peak separation (k_BT=14.6 meV for temperature T=170

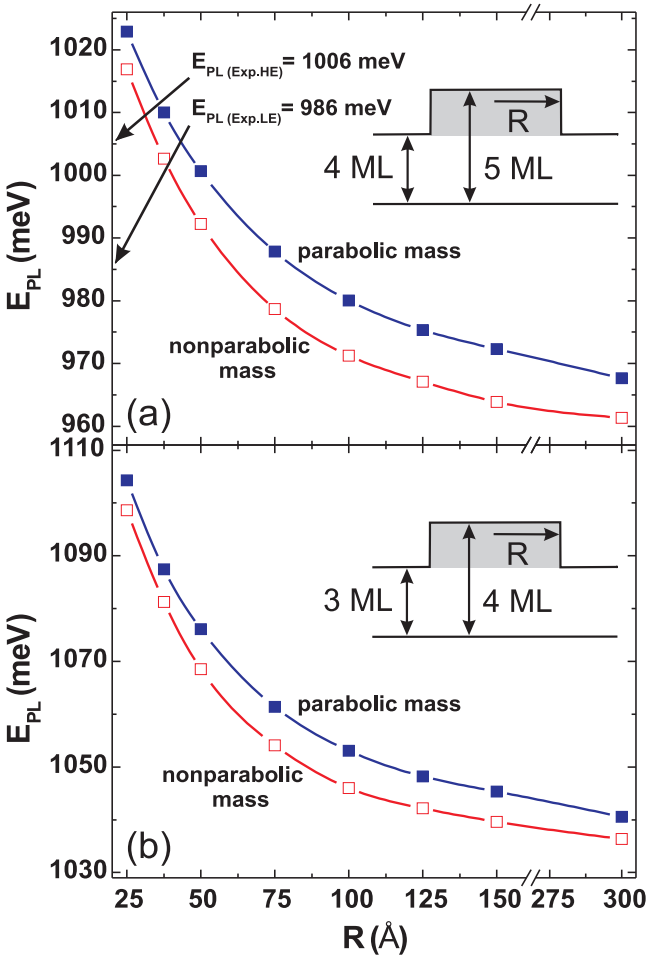

Fig. 4.8: The PL energy as a function of the fluctuation radius R for InAs/InP quantum well with width of 4 ML (a) and 3 ML (b), and fluctuation of 1 ML with the profile shown in the inset of each graph. Symbols are the calculated points and the curves are guides to the eye. The experimental PL energy of the HE and LE peaks is indicated in the inset of the graph (a).

K). We also found that the intensity of the 4 ML peak at 200 K retains 70 % of the intensity at 20 K. Because of unclarity regarding the dimensions of the well with due to thickness fluctuations, it motivated us to study the excitonic properties in the QW with local well width fluctuations.

4.5 WIDTH FLUCTUATIONS IN QUANTUM WELL

Here, we study the influence of the InAs/InP quantum well width fluctuation on the electron-heavy-hole transition (PL) energy. As was mentioned previously, the closest theoretical PL energy to the experimental PL energy of the HE peak is for a QW with width 4 ML. Therefore, theoretically we investigate the QW with width of 4 ML and a fluctuation of 1 ML (let us call it a 4-5 QW), and with width of 3 ML and fluctuation of 1 ML (let us call it a 3-4 QW), as shown in the inset in Fig. 4.8(a) and Fig. 4.8(b), respectively. We compute the PL energy for 3-4 and 4-5 QWs as a function of the fluctuation radius R and compare it with the experimental PL energies of the HE and LE peaks. Besides, we present the results using the bulk (parabolic) mass of the electron and the results when including the effect of band nonparabolicity. The best fit for the 4-5 QW is found when the fluctuation radius is between 25 and 50 Å, as we can see in Fig. 4.8(a). For larger fluctuation radii R, the PL energy of the ground state decreases, as expected. The calculated PL energies for the 3-4 QW are above the experimental PL energies of the HE and LE peaks even when the fluctuation radius is R=300 Å, which PL energy $\mathrm{E}_{PL(300\mathring{A})}$=1036 meV is close to the one of the 4 ML well $\mathrm{E}_{PL(4ML)}$=1032 meV.

In the next step, we calculated the electron-heavy-hole Coulomb interaction energy dependence on the quantum well width fluctuation radius for the 4-5 QW. In Fig. 4.9 the Coulomb energy between electron and heavy-hole in the ground state is shown. We present the results for a parabolic effective mass (the curve with full squares in Fig. 4.9) and nonparabolic electron effective mass (see the curve with open squares). The size of the Coulomb interaction energy is larger when band nonparabolicity is included, because of smaller electron effective mass. The largest absolute value of both energies decrease continuously up to R=75 Å in case of parabolic mass, and up to R=50 Å when the effect of band nonparabolicity is included. The reason for such an energy decrease at small R is the spill-over of the electron wavefunction. This is also demonstrated in the inset of Fig. 4.9, where we show that the electron density for the R=50 Å is more squeezed than the one for R=25 Å. The electron density for R=150 Å is the most prolongated in comparison to the previous two radii, as expected, because the radius of the fluctuation increases, *i.e.* the electron is less localized in the plane.

Let us examine the exciton diamagnetic shift in the InAs/InP QW with the local width fluctuations in the presence of a magnetic field parallel to the growth direction ($\mathbf{B}_{\perp}//\hat{z}$). In Figs. 4.10(a) and (b) we compare the theoretical results of the exciton diamagnetic shift for the 4-5 and 3-4 QWs with the experimental results of the HE peak (see the curves with the symbols and the full circles (black) in Fig. 4.10, respectively). We present the calculations with and without inclusion of band nonparabolicity (see the curves with the open and closed symbols in Fig. 4.10, respectively) when the QWs fluctuation radii

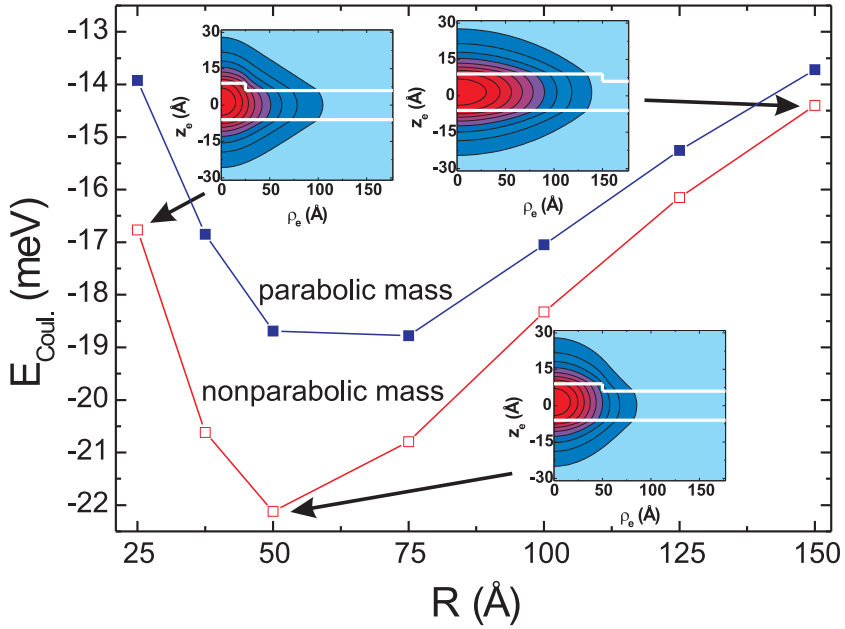

Fig. 4.9: The electron-heavy-hole Coulomb interaction energy as a function of the fluctuation radius R for InAs/InP quantum well with width of 4 ML and fluctuation of 1 ML. The insets show contour plots of the electron density for R=25, 50 and 150 Å, respectively.

are in the range of 25 and 300 Å for both the 3-4 and 4-5 QWs. Again, we observe a smaller diamagnetic shift for the case when nonparabolicity for the electron is included than in the case when it is excluded, as seen previously for parallel magnetic field (see Fig. 4.4), but now the effect is much larger. Up to 30 T we found the best agreement between theory and experiment for the 4-5 QW with well width fluctuation radius R=50 Å, while a full agreement in the whole B region is achieved for the 3-4 QW with the same well width fluctuation radius (compare the curves with the open circles (red) and experimental points in Figs. 4.10(a) and (b)). Nevertheless, for the 4-5 QW the computed PL energy is within 15 meV from the experimental PL energy of the HE peak (compare the curve with the open symbols (red) for R=50 Å and the experimental value of the PL energy in Fig. 4.8(a)), while for the 3-4 QW a difference of about 60 meV is found (compare the curve with the open symbols (red) for R=50 Å and the experimental value of the PL energy in Fig. 4.8(b)). Besides, for the radius of 300 Å the diamagnetic shift is much larger than the one for R=50, 37.5 and 25 Å. This is a consequence of the wavefunction spill-over effect for the electron. In the case of perpendicular magnetic field the discrepancy between

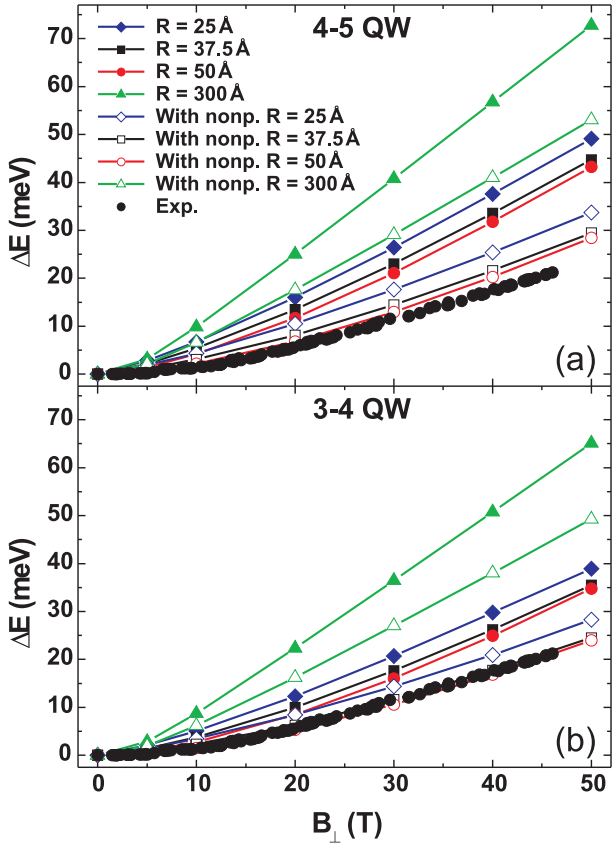

FIG. 4.10: The exciton diamagnetic shift as a function of perpendicular magnetic field ($\mathbf{B}_\perp // \hat{z}$) for InAs/InP quantum well. The curves with the open and closed symbols correspond to the exciton diamagnetic shift with and without taking into account the effect of band nonparabolicity for the electron. The curves with the diamonds (blue), squares (black), circles (red) and triangles (green) correspond to the quantum well with width of 4 ML, fluctuation width of 5 ML (a), and the fluctuation radius of 25, 37.5, 50 and 300 Å, respectively. In graph (b) the same identification of the curves is used as in graph (a), but now for the quantum well with width of 3 ML and fluctuation width of 4 ML. The full circles (black) correspond to the experimental data.

theory and experiment for the 4-5 QW is about 5 meV at 45 T, when R=50 Å. However, the exciton extent in the plane of the 4-5 QW with the radius of the fluctuation R=50 Å is 6.7 nm (6.2 nm for the 3-4 QW), which is in reasonable agreement with the exciton radius found from experiment 7.7 nm for the 4 and 5 ML QW.

4.6 CONCLUSIONS

In summary, we studied theoretically and experimentally the vertical confinement in a InAs/InP self-assembled QWR and in a InAs/InP QW. The wavefunction radii of the electron, heavy-hole and exciton along the growth direction of the QW and [001] direction of the QWR were calculated. From comparison with the qualitative measure of the vertical exciton extent obtained from the experimental data, we conclude that the exciton wavefunction spill-over effect in the 3-5 ML QWs and the 4-6 ML QWRs is large.

The exciton diamagnetic shift for QW in the presence of parallel magnetic field and for QWR in the presence of magnetic field applied along the [110] direction is calculated, reflecting in both cases the confinement properties of the wire height and the well width. We obtained the best agreement between theory and experiment for the QWR with height of h=6 ML, and also a fair agreement for QWR with h=4 and 5 ML, when using the parabolic mass of the electron. Deviation from the experiment at B=45 T is found to be less than 1.3 meV for 4 ML QWR and about 1 meV for 5 ML QWR. When comparing the PL energies and the diamagnetic shift in the QW, the best agreement is found for a 4 ML well, when including the conduction band nonparabolicity effect.

Experimental results of the laser power dependence at different temperatures for InAs/InP QW indicate that the charge carriers (excitons) are trapped by the well width fluctuations. Numerical results of the PL energy for the QW with local width fluctuations show that experimentally found HE and LE PL peaks correspond rather to the QW with width of 4 ML and the fluctuation width of 1 ML, than to the 3 ML well with the fluctuation width of 1 ML. The best agreement for the HE peak is found for the 4-5 QW when the fluctuation radius R is between 25 and 50 Å. The calculated exciton diamagnetic shift in the presence of a perpendicular magnetic field for both 3-4 and 4-5 QWs with R=37.5-50 Å, when using the nonparabolic effective mass of the electron, fit best with the experimental obtained diamagnetic shift of the HE peak.

Publications. The results in this chapter were published as:

- Y. Sidor, B. Partoens, F. M. Peeters, J. Maes, M. Hayne, D. Fuster, Y. González, L. González, and V. V. Moshchalkov, *Exciton energy in InAs/InP quantum wires and quantum wells in the presence of a magnetic field* (submitted to Phys. Rev. B).

5

Influence of the shape and size of a quantum wire on the trion binding energy

5.1 INTRODUCTION

In the previous chapters, we investigated the energy spectrum of a single exciton in a QWR. The next step is to extend this analysis to exciton complexes. In the present chapter we report our results on the stability of negative and positive trions in self-assembled rectangular and V-shaped QWRs.

Negative (X^-) and positive (X^+) trions result from the binding of an exciton (X) with an extra electron or hole, respectively. The existence of two kinds of trions was first suggested by Lampert [67]. Due to the relatively small binding energy of trions in bulk semiconductors, they can only be observed at very low temperatures (T<10 K). Recent progress in semiconductor growth techniques has made it possible to fabricate low-dimensional nanostructures. The reduced dimensionality increases considerably the binding energy of trions, and thus facilitates the formation of X^- and X^+ in semiconductor quantum wells, quantum wires, and quantum dots [68–70, 156–158]. It was shown that well width fluctuations in QWs will trap the trion and leads to a large increase of its binding energy [145, 146].

The purpose of this work is to investigate the stability of charged excitons (trions) in a QWR. Our work is motivated by the recent observation of negatively and positively charged excitons in V-shaped GaAs/$Al_{0.32}Ga_{0.68}$As QWRs [44]. We will also study the formation of the trions in self-assembled

InAs/InP QWRs which were investigated experimentally in Refs. [51] and [129]. In our model we include the true geometrical shape of the V-shaped and the rectangular wires, the influence of strain on the particle confinement potentials in the self-assembled wires, as well as the mass mismatch between the wire and the barrier materials. The 2D calculations are based on a finite element method within the single-band effective mass approximation.

In previous work on trions confined in a QWR a parabolic confinement potential was assumed [159]. Such an assumption simplifies considerably the calculations but it is not able to model effects that are specially due to the shape of the QWR. Recently, trions were also studied [160] in circular free standing wires. Effects due to the dielectric mismatch that renormalize the Coulomb inter-particle interaction are very important in this system. The latter can be neglected in the present study of embedded wires where the well and barrier material have particulary the same dielectric constant.

This chapter is organized as follows. In Sec. 5.2 we describe our theoretical model and we give details about the approximations that are used to solve it. In Sec. 5.3 we present our numerical results. Our conclusions are given in Sec. 5.4.

5.2 THEORETICAL MODEL

The InAs/InP self-assembled QWR is modelled as a 2D rectangular quantum box with height h and width w, as shown schematically in Fig. 5.1(a). We identify the crystallographic axes [110], [001], and [1$\bar{1}$0] with the x, y and z axes of the wire [8, 134, 136]. For the simulations of the V-shaped GaAs/$Al_{0.32}Ga_{0.68}$As QWR we use a profile with heights h and H, and the base length w (indicated by the white line in Fig. 5.1(b)), as suggested by the transmission electron microscopy (TEM) image of the wire in Ref. [161].

We assume that the conduction and highest valence bands are decoupled, which is a reasonable approximation for the two considered types of wires. This is expected to be a reasonable approximation because of the large direct band gap of the InAs and GaAs materials. The full Hamiltonian of a negative trion in a QWR, within the single-band effective mass approximation, is given by

$$H_{X^-} = H_{e1} + H_{e2} + H_h - \frac{e^2}{\varepsilon|\mathbf{r}_{e1} - \mathbf{r}_h|} - \frac{e^2}{\varepsilon|\mathbf{r}_{e2} - \mathbf{r}_h|} + \frac{e^2}{\varepsilon|\mathbf{r}_{e1} - \mathbf{r}_{e2}|}, \quad (5.1)$$

where *e1* and *e2* indicate the two electrons and h the hole. $H_{e1(2)}$ is the Hamiltonian of the confined first (second) electron, H_h is the hole Hamiltonian, e is the free-electron charge, and ε is the dielectric constant taken as the average value of the one of the wire and the barrier. The last three terms in the full Hamiltonian are the electron-hole and electron-electron Coulomb interactions. Note, that the Hamiltonian (5.1) is 9D. We are allowed to separate the

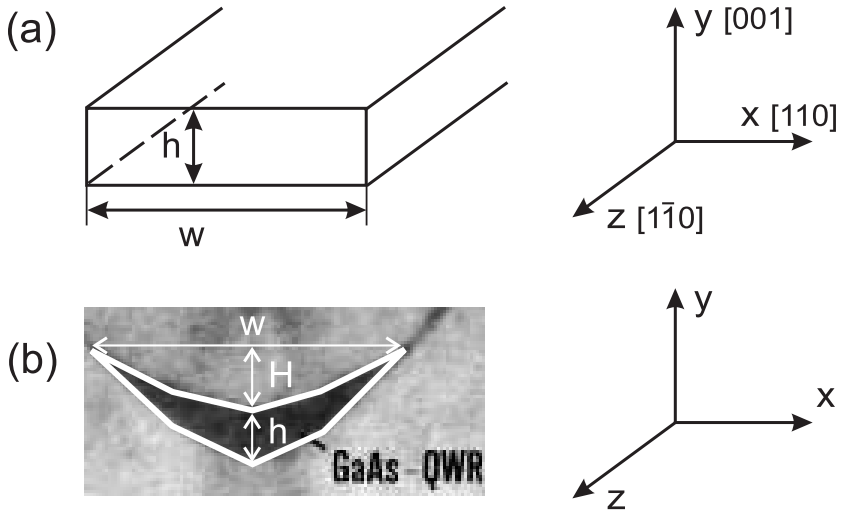

Fig. 5.1: Schematics showing of (a) our model of rectangular self-assembled InAs/InP QWR with height h and width w. (b) Geometry of V-shaped QWR with thicknesses h and H at its center, and the base length w, as suggested by TEM micrography in Ref. [161].

z-motion from the lateral motion in the xy-plane because of the strong confinement in the xy-plane while there is no confinement for the particles along the wire growth direction (z-direction). With other words, we assume that the Coulomb interaction does not effect the xy-motion of the particles, so that we can separate the electrons and hole wavefunctions. In this case the negative trion wavefunction can be written as

$$\Psi_{X^-}(\mathbf{r_{e1}}, \mathbf{r_{e2}}, \mathbf{r_h}) = \Psi_{e1}(x_{e1}, y_{e1})\Psi_{e2}(x_{e2}, y_{e2})\Psi_h(x_h, y_h)\Phi(z_{e1}, z_{e2}, z_h), \quad (5.2)$$

where $\Psi_{e1}(x_{e1}, y_{e1})$, $\Psi_{e2}(x_{e2}, y_{e2})$ and $\Psi_h(x_h, y_h)$ are the electrons and hole wavefunctions in the lateral directions, respectively, and $\Phi(z_{e1}, z_{e2}, z_h)$ is the wavefunction of the negative trion along the wire direction. Next, we averaged the 9D Schrödinger equation over the over the single particle wavefunctions Ψ_{e1}, Ψ_{e2} and Ψ_h in the confinement directions x and y and we are left with a differential equation describing the z-motion of the 3 particles. Then, we introduce the relative coordinates between the electrons and hole $z_{1(2)} = z_h - z_{e1(2)}$ and the center-of mass coordinate (c.m.) $Z{=}(m^*_{e1}z_{e1}{+}m^*_{e2}z_{e2}{+}m^*_h z_h)/(2m^*_{e1}{+}m^*_h)$. The center-of mass momentum $K_{\text{c.m.}}$ is an exact integral of motion, which allows us to decouple the slow motion of the center-of mass from the fast relative motion

$$\Phi(z_{e1}, z_{e2}, z_h) = \phi_{X^-}(z_1, z_2)\exp\left(iK_{\text{c.m.}}Z\right), \quad (5.3)$$

and to obtain the effective 2D Schrödinger equation for the relative motion of the negative trion

$$\Big[-\frac{\hbar^2}{2\mu_z}(\nabla_{z_1}^2+\nabla_{z_2}^2)-\frac{1}{m_h^*}\nabla_{z_1}\nabla_{z_2}+U_{eff}^{(e1-e2)}(z_1-z_2)-U_{eff}^{(e1-h)}(z_1)$$
$$-U_{eff}^{(e2-h)}(z_2)\Big]\phi_{X^-}(z_1,z_2)=E_{X^-}\phi_{X^-}(z_1,z_2), \tag{5.4}$$

where $\mu_{z_1}=\mu_{z_2}$ is the reduced mass of the first electron and hole ($h1$) or the second electron and hole ($h2$) in the z-direction, which is equal to the reduced mass of a neutral exciton μ_z (see Eq. (3.22) in chapter 3) because we assume that two electrons $e1$ and $e2$ are identical, and E_{X^-} and $\phi_{X^-}(z_{h1},z_{h2})$ are the total energy and the relative wavefunction of the negative trion, respectively. The procedure of calculating the effective potentials $U_{eff}(z_{h1}-z_{h2})$, $U_{eff}(z_{h1})$ and $U_{eff}(z_{h2})$ is the same as for the single exciton which was discussed in Sec. 3.2 of chapter 3. Thus, the problem is reduced to solve a 2D differential equation. The latter was realized numerically by using the finite element method.

Similarly, we obtain the corresponding equation for the relative motion of the X^+

$$\Big[-\frac{\hbar^2}{2\mu_z}(\nabla_{z_1}^2+\nabla_{z_2}^2)-\frac{1}{m_e^*}\nabla_{z_1}\nabla_{z_2}+U_{eff}^{(h1-h2)}(z_1-z_2)-U_{eff}^{(e-h1)}(z_1)$$
$$-U_{eff}^{(e-h2)}(z_2)\Big]\phi_{X^+}(z_1,z_2)=E_{X^+}\phi_{X^+}(z_1,z_2), \tag{5.5}$$

where E_{X^+} is the total energy of the positive trion. Note, that in this case the definition for the relative positions of the first and the second hole with respect to the electron position, namely $z_1=z_{h1}-z_e$ and $z_2=z_{h2}-z_e$, and for the center-of mass coordinates $Z=(m_e^*z_e+m_{h1}^*z_{h1}+m_{h2}^*z_{h2})/(m_e^*+2m_{h1}^*)$ are different from those for the X^-.

The input parameters used in our calculations are given in Table 5.1. The values of the parameters have been taken from Ref. [98], or indicated otherwise. We include strain effects and conduction band nonparabolicity following our earlier theoretical approaches of Refs. [136, 178]. The numerical calculations are based on the finite element technique on a variable size grid.

5.3 NUMERICAL RESULTS AND DISCUSSIONS

First we present results on the stability of trions in self-assembled rectangular InAs/InP QWRs. The possibility of observing the negative (positive) trion depends on its stability against dissociation into an exciton and a free electron (hole). Therefore, we calculate the binding energies $E_{X^-}^B$ and $E_{X^+}^B$ for both negative and positive trions, which is defined as the difference between the

Table 5.1: Input material parameters for InAs/InP and GaAs/$Al_{0.32}Ga_{0.68}As$ QWR's used in the calculations: lattice constant a_0, band gap E_g, electron mass m_e (Refs. [130–132]), Luttinger parameters γ_1 and γ_2, nonparabolicity parameters α (Refs. [150–152]), the hydrostatic deformation potential for the conduction band a_c, the deformation potentials of the valence band a_v, b and d, strain coefficients C_{11} and C_{12}, and dielectric constant ε. For $Al_xGa_{1-x}As$ material parameters, the first-order interpolation formula is used: parameter($Al_xGa_{1-x}As$)= parameter(GaAs)$\pm x$(parameter(GaAs)-parameter(AlAs)).

Parameter	InAs	InP	GaAs	$Al_{0.32}Ga_{0.68}As$
a_0 (Å)	6.058	5.869	- -	- -
E_g (eV)	0.417	1.424	1.519	1.918
m_e (m_0)	0.023	0.077	0.067	0.094
γ_1	20	5.08	6.98	5.95
γ_2	8.5	1.6	2.06	1.66
α (eV^{-1})	1.4	- -	0.64	- -
a_c (eV)	-5.08	- -	- -	- -
a_v (eV)	1	- -	- -	- -
b (eV)	-1.8	- -	- -	- -
d (eV)	-3.6	- -	- -	- -
C_{11} (GPa)	83.29	- -	- -	- -
C_{12} (GPa)	45.26	- -	- -	- -
ε	15.15	12.5	12.9	12.0

exciton binding energy and the trion total energy E_{X^-} and E_{X^+}, respectively. For InAs/InP QWR with height h=15 Å and width w=180 Å we obtained earlier [136] the exciton binding energy E_X^B=13.79 meV. From our present calculation we found the total energies $E_{X^-}^B$=15.36 meV and $E_{X^+}^B$=16.54 meV which results in the binding energy of 1.57 meV for X^- and 2.75 meV for X^+. At present there are no experimental results on $X^\pm$ in this system to compare with. Besides, we conclude that the observed binding energy for X^+ is nearly two times larger than the one for X^-.

In Figs. 5.2 and 5.3 we show the trion wavefunction of the ground and the first excited state for InAs/InP QWR with height h=15 Å and width w=180 Å. As we can see from Fig. 5.2(b), the antisymmetric wavefunction of the first excited state of X^- is unbound, because for such a large computational grid of 2000×2000 Å the wavefunction is nonzero only near the axis and vanishes only at the edges of the grid. When we increase the dimensions of the grid, the situation does not change. Nevertheless, the wavefunction of the first excited state of the positive trion is well confined inside the QWR with respect to the z_{h1} and z_{h2} axes (see Fig. 5.3(b)). From this we conclude that the X^- has

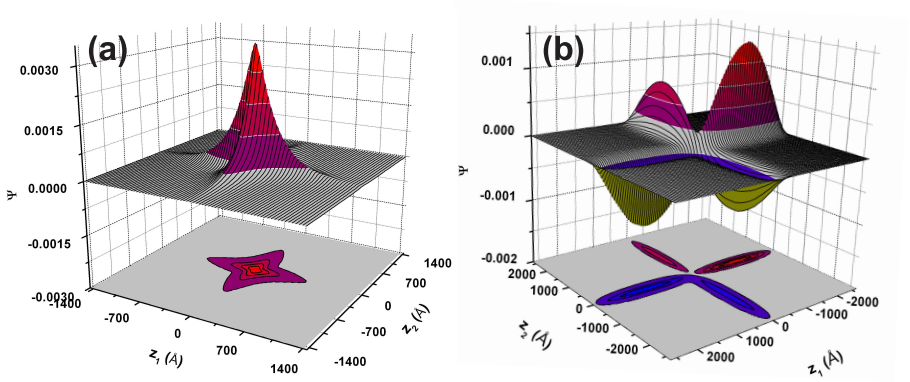

FIG. 5.2: The wavefunction for relative motion of the ground (a) and the first excited (b) state for a negative trion X^- in a self-assembled InAs/InP QWR with height h=15 Å and width w=180 Å.

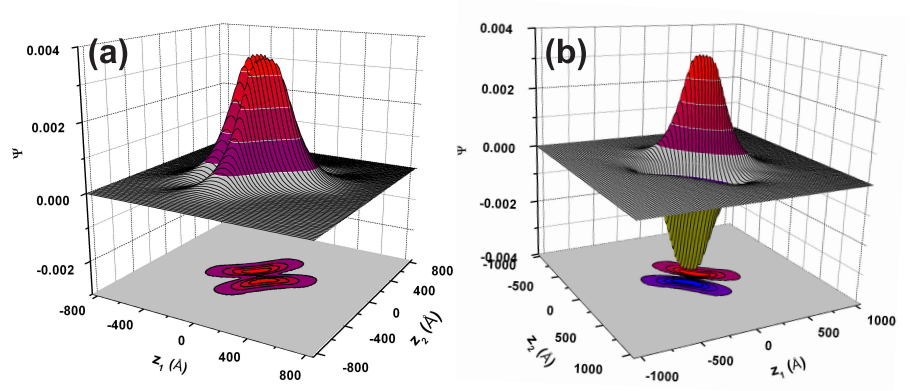

FIG. 5.3: The same as Fig. 5.2 but now for the positive trion X^+.

only one bound state for the chosen parameters of the QWR. Notice from the contour plots that the ground state wavefunction has two fold symmetry and is symmetric with respect to the lines z_1=z_2 and z_1=$-z_2$. The X^- ground state is more spread out than the X^+ and the latter is almost zero along $z_1 = z_2$ which implies that in the X^+ ground state the probability to find both holes at the same spatial position is almost zero, while this is not the case for the two electrons in case of the X^-. The wavefunction of the first excited $X^\pm$ state is symmetric with respect to z_1=$-z_2$ and anti-symmetric with respect to z_1=z_2 where the wavefunction exhibits a node. The X^+ excited state is clearly bound with binding energy 2.61 meV.

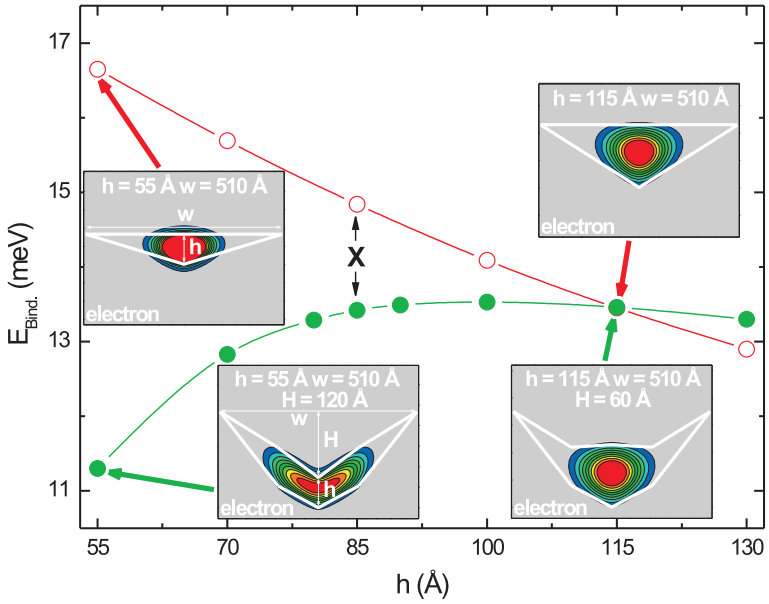

Fig. 5.4: The exciton binding energy as a function of the height h of the GaAs/GaAs/$Al_{0.32}Ga_{0.68}As$ QWR with w=510 Å. The curves with the open (red) and closed (green) circles correspond to the theoretical results when using a triangular and V-shape of the wire, respectively, as shown in the insets. The insets show the contour plots of the electron wavefunctions when h is 55 and 114 Å.

Next, we examine the exciton binding energy for a more complicated confinement geometry as realized in the V-grooved GaAs/$Al_{0.32}Ga_{0.68}As$ QWR. In Ref. [44] the thickness of the V-shaped QWR, measured at its center, was determined to be 70 Å for a thick QWR sample. In order to investigate the dependence of the exciton energy on the height we varied the GaAs/$Al_{0.32}Ga_{0.68}As$ QWR height h in the range between 55-130 Å. We used the potential profile (indicated by the white line in Fig. 5.1(b)) as directly taken from Ref. [161], where the thickness was h=88 Å, which is rather close to the one of the thick QWR (h=70 Å). The variation of the height h (and consequently thickness H) for fixed width of 510 Å was realized by rescaling the profile shown in Fig. 5.1(b). In Fig. 5.4 we compare the effect of the shape of the confinement potential by showing the results for a V-shaped GaAs/$Al_{0.32}Ga_{0.68}As$ QWR

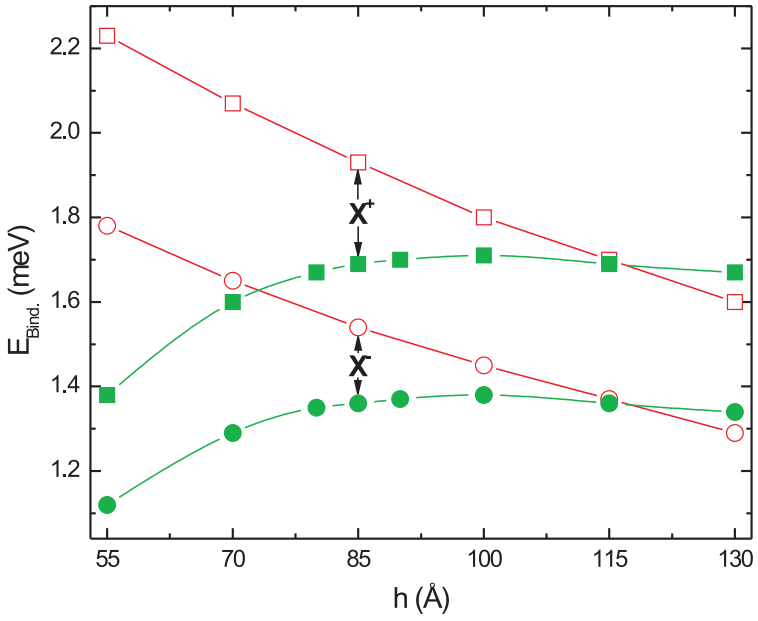

FIG. 5.5: The same as Fig. 5.4 but now for the positive trion X^+ and the negative trion X^-.

(see the curve with the full circles (green) in Fig. 5.4) with the one of a triangular shape of the GaAs/$Al_{0.32}Ga_{0.68}$As QWR (see the curve with the open circles (red) in Fig. 5.4). The exciton binding energy decreases as the height h becomes larger when using the triangular shape of the wire. Such behavior of the exciton binding energy can be easily explained, since the electron (as well as the heavy-hole with the larger effective mass) is well confined inside the wire and its wavefunction becomes larger in size as the height of the wire h increases, as shown in the top two graphs in the inset of Fig. 5.4. However, when we consider the V-shaped GaAs/$Al_{0.32}Ga_{0.68}$As QWR, we found the opposite behavior for the exciton binding energy up to h=100 Å, and beyond that point the binding energy decreases slightly when h approaches the value of 130 Å. The reason is that for the smaller wire with fixed width w, the electron (the heavy-hole) wavefunction is more strongly confined along the height direction, but less squeezed along the width direction (see the bottom two graphs in the inset of Fig. 5.4), which results in a decrease of the exciton binding energy.

Table 5.2: The numerical (theory) and experimental (exp.) binding energy of the negative trion $E^B_{X^-}$ and the positive trion $E^B_{X^+}$ for thick and thin QWR samples.

	$E^B_{X^-}$	$E^B_{X^+}$
Thin (theory)	2.25	2.85
Thin (exp.)	4.6	3.0
Thick (theory)	1.29	1.6
Thick (exp.)	2.8	- -

Further, we discuss the formation of X^- and X^+ in the GaAs/$Al_{0.32}Ga_{0.68}$As QWR. In Fig. 5.5 we show the binding energy of the positive and negative trions as a function of the height h of the GaAs/$Al_{0.32}Ga_{0.68}$As QWR with width w=510 Å. Similar to the binding energy for the exciton, we observe different behaviors for the binding energy for X^- and X^+ depending on the shape of the wire. The binding energy of both negative and positive trions diminishes for the larger wires in case of considering the triangular-shaped wire, and the enhancement of the binding energy of X^- and X^+ is observed in the range of the height between 55-100 Å when we assume the V-shaped GaAs/$Al_{0.32}Ga_{0.68}$As QWR. Moreover, in Fig. 5.5 we can see that the binding energy for X^+ is larger than the one for X^-, which means that the positive trion is more stable than the negative trion in GaAs/$Al_{0.32}Ga_{0.68}$As QWR. In Ref. [44] the binding energy of the positive trion X^+ was determined as 3 meV for the thin QWR sample (there were no data for the thick wire sample). For the simulations of the thin QWR we used a similar geometry as shown in Fig. 5.1(b), with a thickness of 30 Å and width of 204 Å, which was approximated by rescaling of the profile in this figure. When comparing the calculated binding energies of X^+, we found that the thin wire results $E^B_{X^+}$=2.85 meV is in good agreement to the above mentioned experimental binding energy, as listed in Table 5.2. However, for X^- we obtained in the case of the thin (thick) QWR a binding energy of 2.25 meV (1.29 meV), respectively, which is about two times larger than the experimental one 4.6 meV (2.8) (see Table 5.2). A possible reason for the enhanced X^- binding energy is that the X^- is probably localized along the unconfined wire direction as a consequence of width and/or height fluctuations. Such fluctuations have been shown to enhance the X^- binding energy with about a factor of two in quantum wells [145, 146]. The effect of such fluctuations on X^- is much more pronounced than on X^+ because electrons are lighter, therefore they will be more strongly influenced by such local fluctuations than holes. But this can not explain the discrepancy in the trend that experimentally X^- has a larger binding energy than X^+ which is opposite to that found theoretically in our calculation. This is still an unsolved problem.

5.4 CONCLUSIONS

We calculated and analyzed trions in a QWR. Our numerical results predict the formation of negative and positive trions in self-assembled InAs/InP QWRs. We theoretically confirm the stability of both trions $X^{\pm}$ in V-shaped $GaAs/Al_{0.32}Ga_{0.68}As$ wires and compared the binding energy with those measured experimentally. We found a strong dependence of the $X^{\pm}$ binding energy on the shape and the size of the QWR. The experimentally found larger binding energy for the X^{-} than for the X^{+} is not confirmed by our theoretical calculations and needs further investigation.

Publications. The results in this chapter are being prepared for a publication:

- Y. Sidor, B. Partoens, and F. M. Peeters, *Influence of the shape and size of a quantum wire on the trion binding energy* (in preparation).

6

Excitons in coupled InAs/InP self-assembled quantum wires

6.1 INTRODUCTION

Since the early 1970's, after the proposal of Esaki and Tsu [1], multiple coupled quantum well structures have been intensively investigated theoretically and experimentally [162]. Early theoretical works on coupled quantum wells were used in the study of conduction [163, 164] and phonon tunneling in superlattices [165].

Technological progress in the growth technique of low-dimensional nacrostructures has shifted the research to the optical properties of coupled quantum wires (CQWRs). For example, Kern *et al.* [166] experimentally and theoretically proved that the coupling of the confined plasmons in $Ga_xIn_{1-x}As$ quantum wires is much more enhanced with respect to the one in coupled quantum wells. Later, Weman *et al.* [167] reported a strong exciton binding energy enhancement in very narrow $GaAs/Al_xGa_{1-x}As$ cylindrical quantum wire arrays as compared to quantum wells. The binding energy of the exciton was determined from the experimental excitonic transitions and compared to calculated values. In another experimental and theoretical work done by Weman *et al.* [168] the electron coupling and tunneling in double V-grooved $GaAs/Al_xGa_{1-x}As$ QWRs was reported. Recently, the interest has shifted towards the study of the electrical and the optical properties in coupled (and also stacked) *self-assembled* quantum wires (see, for example, Refs. [16, 169, 170]).

A further reduction of the dimensionality of nanostructures was realized through the growth of quantum dots. Coupled self-assembled quantum dots have been the subject of several scientific works [171–176]. Pryor [171] calculated within the eight-band $\mathbf{k}\cdot\mathbf{p}$ model the transition between a quantum wire and vertically coupled quantum dots.

In the present work we investigate InAs/InP quantum wires which are promising candidates for aplications in telecommunications, because they emit at the wavelengths 1.3 and 1.55 μm. It was demonstrated [8] that the growth conditions of the InP buffer layer controls the surface rearrangement of the strained InAs layer that is grown on top. Therefore, it is possible to obtain either quantum dot or quantum wire structures for identical InAs coverage and growth conditions. Recently, optical properties of InAs/InP self-assembled quantum wires were studied experimentally [51, 177]. The wires are oriented along the $[1\bar{1}0]$ direction and periodically arranged along the [110] direction with period 18 nm [177]. Their PL spectrum consists of four peaks that is believed to correspond to different heights of the wires.

The main goal of the present work is the investigation of exciton coupling in self-assembled InAs/InP quantum wires studied experimentally in Ref. [177]. We consider rectangular self-assembled InAs/InP CQWRs. Since self-assembled InAs/InP CQWRs are formed by the Stranski-Krastanow growth mode, effects due to strain must be included [136]. The calculations are performed within the single-band effective mass approximation and based on a 2D finite element technique, where the mass mismatch between the barrier and the wire is included. We examine the dependence of the single particle energies and the behavior of the electron and hole density on the distance between two vertically and two horizontally coupled quantum wires, the Coulomb interaction energy and the exciton energy on the small distance between two vertically coupled quantum wires. We also calculate the PL transition energies in these structures as a function of the height of the wires and compare them with available experimental data. From this comparison we are able to deduce the height of the coupled wires.

6.2 MODEL HAMILTONIAN

The experimentally grown InAs/InP quantum wires are oriented along the $[1\bar{1}0]$ direction and periodically arranged along the [110] direction, with period 180 Å [177]. The average height and the width of the wires were determined from XTEM measurements. We consider two 2D rectangular quantum boxes at a distance d from each other, each with height h and width w, as illustrated in Fig. 6.1. The rectangular shape of the wires approximates the experimentally measured shape. For self-assembled InAs/InP quantum wires we have typically $w \gg h$. Therefore we consider the situation of two horizontal coupled wires

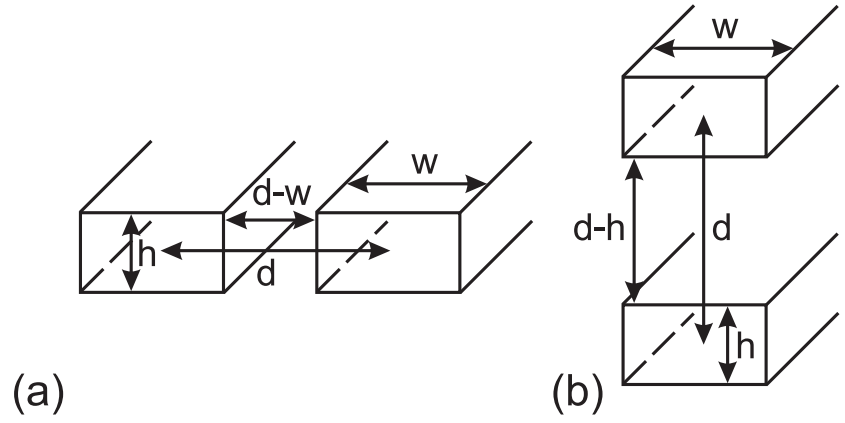

Fig. 6.1: Theoretical model of horizontally coupled (a) and vertically coupled (b) rectangular quantum wires with height h, width w, and distance d between the wires.

placed along the wire width direction ([110] direction) as corresponding to the experimental situation [177] (see Fig. 6.1(a)), and two vertically coupled wires directed along the height direction (see Fig. 6.1(b)).

The full Hamiltonian for an exciton in such CQWRs consists of the single electron part H_e, the single hole part H_h and the Coulomb interaction term between the electron-hole pair

$$H = H_e + H_h - \frac{e^2}{\varepsilon|\mathbf{r}|}, \tag{6.1}$$

where e is the free-electron charge, $\mathbf{r}=\mathbf{r_e} - \mathbf{r_h}$ denotes the relative distance between the electron (e) and the hole (h) and ε is the dielectric constant taken as the average value of the wire and the barrier (see chapter 3). According to the effective-mass theory the Schrödinger equation for the exciton can be written as

$$H\Psi(\mathbf{r_e}, \mathbf{r_h}) = E\Psi(\mathbf{r_e}, \mathbf{r_h}). \tag{6.2}$$

We assume that the conduction band and the valence band are decoupled, which is a reasonable approximation for the considered wires. The minimum of the conduction band and the maximum of the valence band are localized around the Γ-point of the wire. Along the wire growth direction (here taken to be the z-direction) there is no confinement for the particles in the wires, while in the xy-plane the electron and hole are strongly confined. For this reason we are allowed to separate the z-motion from the xy-motion. Further, we assume the Coulomb interaction term as a perturbation, so that we can separate the

electron and hole wavefunctions. Next, we introduce the relative coordinates z=z_e-z_h and the center-of mass (CM) coordinates Z=$(m_e z_e$+$m_h z_h)/M$ which allows us to write the solution to Eq. (6.2) as

$$\Psi(\mathbf{r_e}, \mathbf{r_h}) = \Psi_e(x_e, y_e)\Psi_h(x_h, y_h)\varphi(z)\exp(iK_{\mathrm{CM}}Z), \tag{6.3}$$

where K_{CM} is the momentum of the center-of mass and M=m_e+m_h is the total mass. To calculate the electron and hole energies, densities and the Coulomb interaction between the particles we first solve, within the single-band effective mass approximation, the single-particle 2D Schrödinger equation in the xy-plane

$$H_e\Psi_e(x_e, y_e) = E_e\Psi_e(x_e, y_e), \tag{6.4}$$

$$H_h\Psi_h(x_h, y_h) = E_h\Psi_h(x_h, y_h), \tag{6.5}$$

and subsequently an effective one-dimensional equation for the motion in the z-direction where the Coulomb interaction is included perturbatively

$$\left[-\frac{\hbar^2}{2\mu_z}\nabla_z^2 + \frac{\hbar^2 K_{CM}^2}{2M} + U_{eff}(z)\right]\varphi(z) = E_C\varphi(z), \tag{6.6}$$

where μ_z denotes the reduced mass of the exciton along the wire axis, $U_{eff}(z)$ is the effective potential and E_C is the Coulomb energy.

We consider both heavy-hole and light-hole states. Different effective masses of the particles are assumed inside and outside the CQWRS. The single-particle 2D Hamiltonian for the electron, and the two different holes (h) in the presence of strain are given by

$$\begin{aligned} H_e &= -\nabla_{xe}\frac{\hbar^2}{2m_e^*(x,y)}\nabla_{xe} - \nabla_{ye}\frac{\hbar^2}{2m_e^*(x,y)}\nabla_{ye} \\ &\quad + E_{ce}(x,y) + a_c\varepsilon_{hyd}(x,y), \end{aligned} \tag{6.7}$$

$$H_h = -\nabla_x\frac{\hbar^2}{2m_h^*(x,y)}\nabla_{xh} - \nabla_{yh}\frac{\hbar^2}{2m_h^*(x,y)}\nabla_{yh} + V_{vh}(x,y), \tag{6.8}$$

where $m_e^*(x,y)$ is the effective mass of the electron, $E_{ce}(x,y)$ is the unstrained conduction band offset, a_c is the hydrostatic deformation potential for the conduction band, $\varepsilon_{hyd}(x,y)$ is the hydrostatic strain, $m_h^*(x,y)$ is the effective mass of the hole, $V_{vh}(x,y)$ denotes the confinement potential of the hole due to the band offsets and strain. The heavy-hole and light-hole confinement potentials are obtained from the Pikus-Bir strain Hamiltonian by its value in

Table 6.1: Material parameters for InAs/InP CQWRs used in the calculations: lattice constant a_0, band gap E_g, electron mass m_e, Luttinger parameters γ_1 and γ_2 (Ref. [98]), the hydrostatic deformation potential for the conduction band a_c, the deformation potentials of the valence band a_v, b and d, strain coefficients C_{11} and C_{12} and dielectric constant ε.

Parameter	InAs	InP
a_0 (Å)	6.058	5.869
E_g (eV)	0.417	1.424
m_e (m_0)	0.023	0.077
γ_1	20	5.08
γ_2	8.5	1.6
a_c (eV)	-5.08	- -
a_v (eV)	1	- -
b (eV)	-1.8	- -
d (eV)	-3.6	- -
C_{11} (GPa)	83.29	- -
C_{12} (GPa)	45.26	- -
ε	15.15	12.5

the center of the wire (see for more details chapter 3 and Ref. [136]). The effect of heavy-hole-light-hole mixing is assumed to be negligible. From our previous study on InAs/InP quantum wire [136] we know that it leads to an insignificant correction to the exciton energy even in the presence of a magnetic field.

The input parameters (see Table 6.1) used for our simulations are taken from chapter 3, except for the mass of the heavy-hole and the light-hole, which is taken the same in each direction [178]

$$\frac{m_0}{m^*_{hh}} = \gamma_1 - 2\gamma_2, \tag{6.9}$$

$$\frac{m_0}{m^*_{lh}} = \gamma_1 + 2\gamma_2, \tag{6.10}$$

where γ_1 and γ_2 are Luttinger parameters (see Ref. [98]), and m_0 is the vacuum electron mass. The numerical calculations are based on the finite element technique on a variable size grid.

6.3 COMPARISON WITH EXPERIMENT

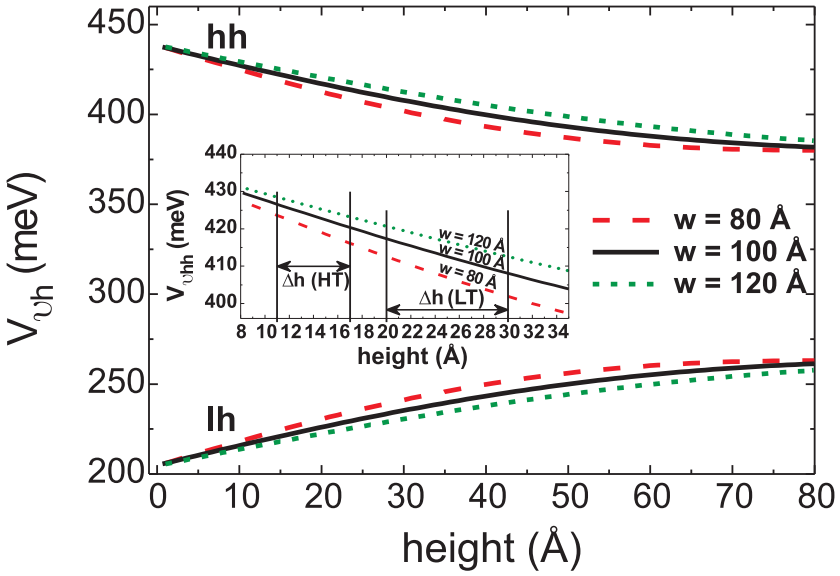

FIG. 6.2: The top of the holes (h) potentials calculated from the strain Hamiltonian at x=0 and y=0 as function of the height of InAs/InP self-assembled CQWRs. The dashed (red), full (black), and dotted (green) curves correspond to the heavy-hole and the light-hole potentials of the CQWRs with width w=80 Å, w=100 Å and w=120 Å, respectively. The inset shows the heavy-hole band offsets for the High T (HT) and Low T (LT) samples (see Ref. [177]).

In Ref. [177] the photoluminescence carrier recombination in InAs/InP self-assembled wires was reported. The PL spectra of two adjacent emission peaks of the High T (HT) and Low T (LT) samples were investigated. The HT and LT samples were grown at different substrate temperature and correspond to CQWRs with different heights. The observed energy distance between these two peaks for both the HT and LT samples correspond to 1 ML (1 ML=3 Å) height fluctuation. The average geometric values of the CQWRs were measured by XTEM [177].

In order to compare our calculations with the experimental data for the HT and LT samples we consider the model of two horizontally CQWRs, as mentioned in previous section of this chapter. We used the heavy- and light-hole band offsets depicted by the dashed, full, and dotted curves in the inset of Fig. 6.2. The different curves correspond to different widths of the CQWRs for both heavy- and light-holes. Strain splits the heavy- and light-hole bands by a value which depends on the matrix elements of the Pikus-Bir-Hamiltonian which depend on the dimension of the quantum wire (see chapter 3). From Fig. 6.2 we notice that the heavy-hole curves are above the light-hole curves in

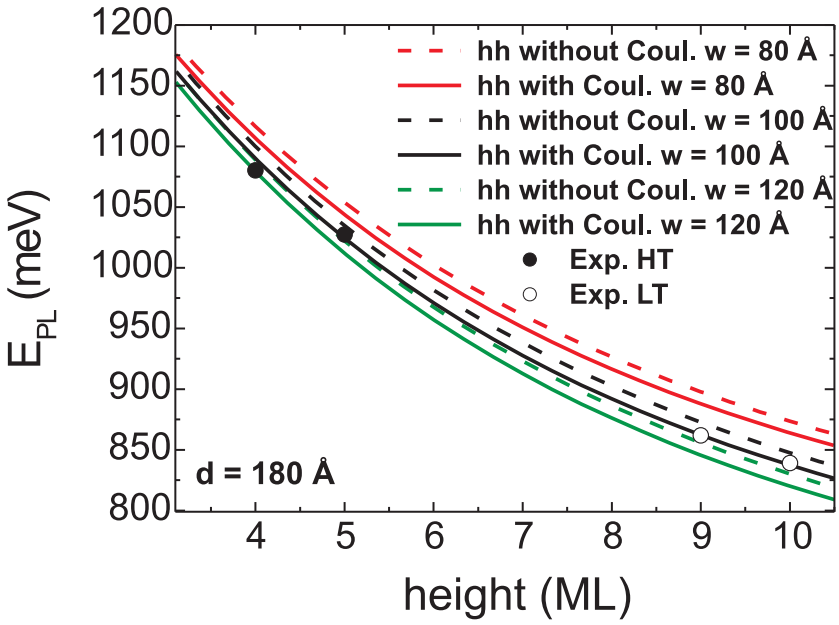

Fig. 6.3: PL peak energies as a function of the InAs/InP CQWRs height. The full and dashed lines are the theoretical calculations for the heavy-hole excitons with and without taking into account the Coulomb interaction, respectively, for the InAs/InP CQWRs with width w=80 Å (red curves), w=100 Å (black curves) and w=120 Å (green curves). The full and open circles correspond to the experimental data for HT and LT samples, respectively.

the whole range of heights up to 80 Å and for three different widths: w=80 Å, w=100 Å and w=120 Å. Therefore, we conclude that the heavy-hole state is the ground state, as in the case of a strained quantum well. Further, in Fig. 6.3, we compare the calculated PL peak energies as a function of the height of the InAs/InP CQWRs for three different widths with the experimental PL energies of the HT and LT samples (indicated by the symbols in Fig. 6.3). The distance between the quantum wires is fixed to d=180 Å. We are allowed to move the experimental points along the height direction with a step of 1 ML to find the optimal agreement with the theoretical curves. The results for the Coulomb interaction included (when both electron and heavy-hole are in the ground state) fit best the experimental points (see full curves in Fig. 6.3), when the two peaks of the HT sample correspond to wire heights of 4 and 5 ML, and the two peaks of the LT sample correspond to heights of 9 and 10 ML. These height values of 4 and 5 ML, and the values of 9 and 10 ML agree with those from XTEM measurements, where the average value of the height for the HT

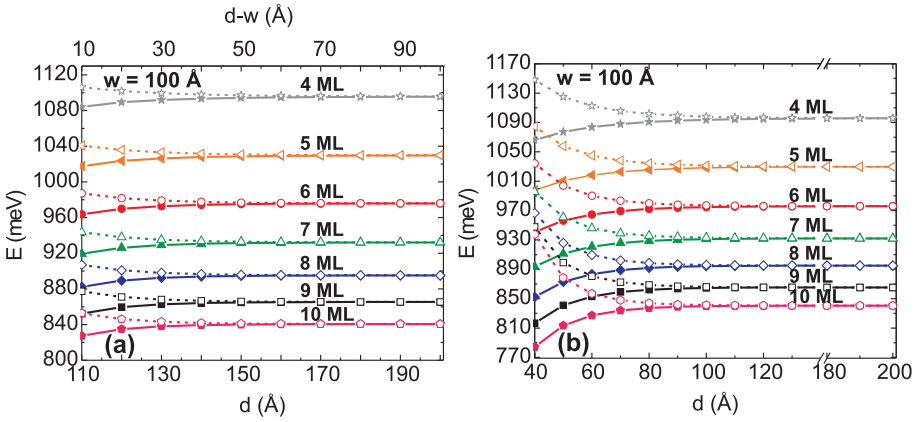

FIG. 6.4: The heavy-hole exciton ground and the first excited state energies as a function of distance d in InAs/InP horizontally (a) and vertically (b) CQWRs. The top scale, $d-w$, in the graph (a) is the distance between the edges of two horizontally CQWRs (see Fig. 6.1(a)). The full curves with the closed symbols and dashed curves with the open symbols correspond to the ground and the first excited state energies of the exciton, respectively. The curves with the stars (grey), rotated triangles (orange), circles (red), triangles (green), diamonds (blue), squares (black) and pentagons (pink) correspond to the CQWRs with the height of 4 to 10 ML (1 ML is 3 Å) in steps of 1 ML and width of 100 Å, respectively.

was found to be h=14±3 Å, for the LT h=25±5 Å, and the average width was found to be w=100±20 Å.

6.4 INTER-WIRE COUPLING: A THEORETICAL INVESTIGATION

Here we investigate the coupling for two wires when placed along the wire width and the wire height direction, *i.e.* the horizontally and vertically CQWRs (see Fig. 6.1). In Fig. 6.4 we examine the dependence of the energy of the ground and the first excited state of the heavy-hole exciton as a function of the distance between the wires. We study this dependence when the height of the wires vary from 4 up to 10 ML (the width of the wires is fixed to 100 Å), which is an experimental range of heights, as known from a previous PL study in chapter 2 (see also Ref. [134]). Figure 6.4(a) shows the results for the horizontally CQWRs where heavy-hole exciton ground state energy slightly decreases as the interdistance becomes smaller, while the first exciton excited state energy slowly increases, as expected. For large interdistances the energy levels become twofold degenerate. The energy of the bonding state (the ground state) decreases and the energy of the anti-bonding state (the first excited state) increases due to the lifting of the degeneracy of the two-fold

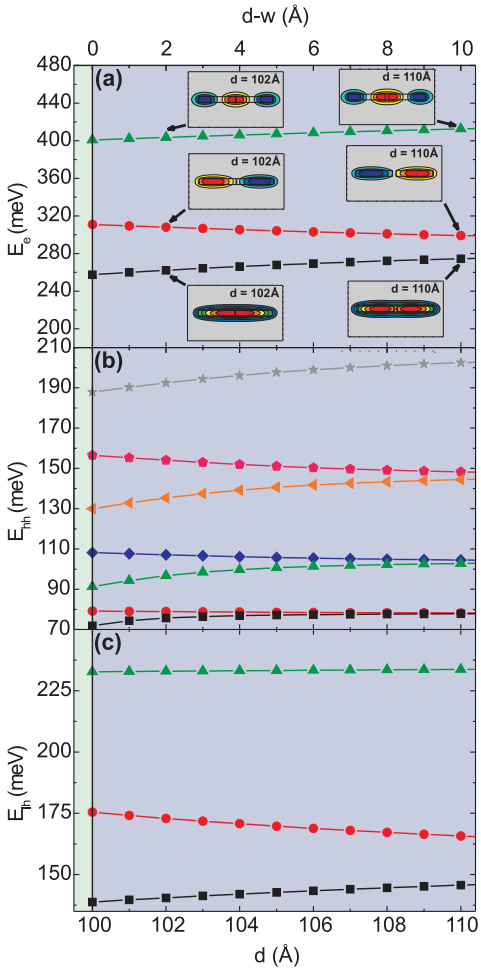

Fig. 6.5: The energy for the electron (a) ground state and the next two excited states, the heavy-hole (b) ground state and the next six excited states and the light-hole (c) ground state and the next two excited states as a function of distance d between the wires in InAs/InP horizontally CQWRs with height h=27 Å and width w=100 Å. The top scale, $d-w$, in the graphs (a), (b) and (c) is the distance between the edges of two horizontally CQWRs (see Fig. 6.1(a)). The insets in the graph (a) show the contour plots of the electron wavefunctions for d equal to 102 and 110 Å.

ground state. It is also clear that there is no evidence of coupling in InAs/InP self-assembled wires when the interdistance between the two wires is 180 Å and therefore the results presented in Fig. 6.3 are identical to those for a single (*i.e.* uncoupled) quantum wire. Coupling sets in when d becomes roughly smaller

than 160 Å. Similar to the horizontally CQWRs, in vertically CQWRs the heavy-hole exciton ground state (first excited state) energies decrease (increase) as d diminishes (see Fig. 6.4(b)). Here coupling is found when d is smaller than 120 Å, and a stronger dependence at small values of d for the exciton ground and the first excited states is noticed.

In Figs. 6.5 and 6.6 we examine the dependence of the energy for the individual particles at smaller inter-wire distance d, up to the moment when two wires in the coupled wire touch each other which occurs for d=100 Å in case of the horizontally CQWRs and when d=27 Å (we consider the height h to be 9 ML=27 Å in Figs. 6.5 and 6.6) for the vertically CQWRs (see the left vertical straight lines at $d - w$ and $d - h$ equal to 0 Å in Figs. 6.5 and 6.6, respectively). Let us consider first the single particles for the horizontally CQWRs (see Figs. 6.5(a) - 6.5(c)). For all particles (electron, heavy- and light-hole) we observe a continuous energy splitting until d reaches 100 Å ($d - w$=0 Å), and the wavefunctions simply merge into the wavefunction of a single wire (compare the wavefunctions for the electron ground and excited state energies in the inset of Fig. 6.5(a), when d is equal to 102 and 110 Å). Besides, we can see that the energy splitting between the bonding state and the anti-bonding state is larger for the electron and the light-hole (see Figs. 6.5(a) and 6.5(c)) as compared to the heavy-hole states (see Fig. 6.5(b)). The larger sensitivity of the electron and the light-hole to the variation of the inter-wire distance is because of their lighter effective mass which is about 10 times less in the wire and at least 5 times less in the barrier than the heavy-hole effective mass.

Interesting new effects arise when we consider vertically coupled InAs/InP quantum wires. Again, the electron ground state wavefunction merges together (compare the electron ground state wavefunction in Fig. 6.6(a), when d equals to 40, 37 and 30 Å). Meanwhile, the ground state energy of the electron decreases with decreasing d, as we have previously shown in Fig. 6.4(b). For the first excited state energy of the electron, when the distance between the wires becomes smaller (see the curve (red) with the circles in Fig. 6.6(a)), the electron first excited state energy increases, as it is shown in Fig. 6.4(b) up to a certain value of d between 37 and 38 Å (see the right vertical straight line in Fig. 6.6a)). Starting from this value and up to d equal to h, it is energetically more favorable for the electron to jump to another state, whose energy decreases (see the curve (green) with the triangles in Fig. 6.6(a)). Also the symmetry of the electron wavefunction of the first two excited states in the transverse directions of the wires have a different behavior with variation of the inter-wire distance. For this reason there is a crossing between the excited states for the electron in the vertically coupled wires, contrary to the horizontally coupled wires where the electron wavefunction symmetry of the excited states remains the same with the varying d (see Fig. 6.5(a) and Fig. 6.6(a)). Furthermore, in the inset of Fig. 6.6(a), where the contour plots of the electron wavefunctions are shown, before and after the crossing the symmetry with respect to the nodal line changes for the first excited state and in the opposite

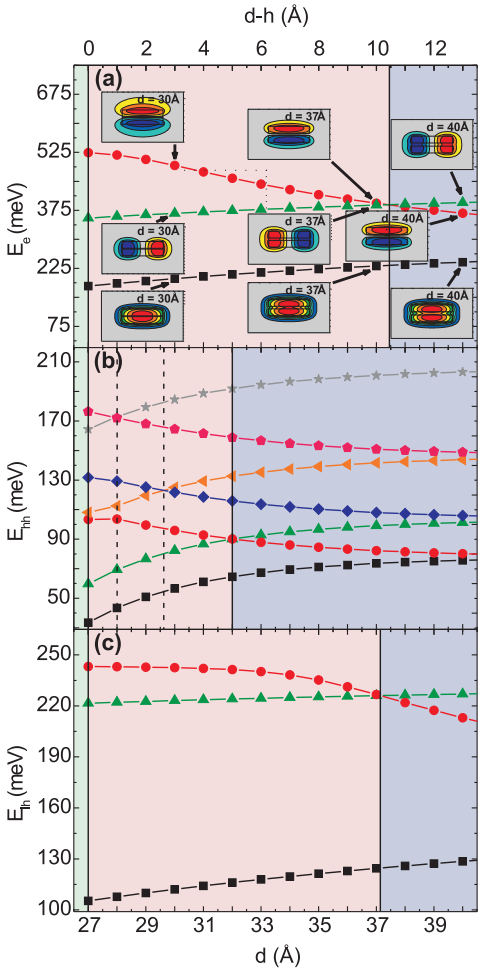

Fig. 6.6: The same as Fig. 6.5 but now for vertically CQWRs. The top scale, $d-h$, in the graphs (a), (b) and (c) is the distance between the edges of two vertically CQWRs (see Fig. 6.1(b)). The insets in the graph (a) show the contour plots of the electron wavefunctions when d is 40 Å, 37 Å and 30 Å.

way for the second excited state. Note that when d is between 27 and roughly 38 Å, the wavefunction for the first two excited states has the same character as for a rectangular single wire. A similar crossing for the heavy-hole (see the right vertical straight line in Fig. 6.6(b) when d equals 32 Å) and for the light-hole (see the right vertical straight line in Fig. 6.6(c) when d is roughly 37 Å) between the first and second excited states is observed. Besides, for the heavy-hole we found crossings between the fourth and fifth (see the dashed

vertical line between 29 and 30 Å) as well as between the sixth and seventh (see the dashed vertical line placed at d=28 Å) heavy-hole excited states. The electron and the light-hole have only three bound states. Note that for electron and holes in InAs/InP vertically CQWRs three regions can be distinguished:

(1) coupled region where the wavefunctions of the lowest levels behave as for a single rectangular wire. But energetically they are already in the coupled regime because the levels are all split (see the middle region in Figs. 6.6(a) and 6.6(c));

(2) coupled region where the energies and the densities of the lowest levels behave as for the coupled wires (see the right region in Figs. 6.6(a) and 6.6(c));

(3) decoupled region, where all levels are twofold degenerate (when d is large).

Next, we investigate the electron-hole Coulomb interaction energy dependence on the distance d between two vertically CQWRs. In order to calculate the Coulomb energy of the first (second) excited state we solve the 1D Schrödinger equation for the relative exciton motion in the z-direction (see Eq. (6.6)) with the effective potential of the first (second) excited state

$$U_{eff1(2)}(z) = \int dx_e dy_e dx_h dy_h |\Psi_{1(2)e}|^2 |\Psi_{1(2)h}|^2 \times \left(-\frac{e^2}{\varepsilon|\mathbf{r}_e - \mathbf{r}_h|}\right), \tag{6.11}$$

where $\Psi_{1(2)}$ is the electron and hole wavefunction of the first (second) excited state. In Fig. 6.7 the Coulomb energies between the electron and heavy-hole both in the first excited state (see the curve with the triangles in Fig. 6.7) and in the second excited state (see the curve with the circles in Fig. 6.7) are shown. We found abrupt jumps for these two energies at the crossing of the first two excited states for the electron at d=37.4 Å and the heavy-hole d=32 Å. Both energies decrease continuously up to the crossing of the excited states of the electron (see the right vertical line at 37.4 Å in Fig. 6.7), meanwhile the absolute value of the Coulomb energy E_1 is larger than the absolute value of the Coulomb energy E_2 of the second excited state. After this crossing up to d=32 Å the situation is opposite, *i.e.*, $|E_2|>|E_1|$ even when the symmetry of the heavy-hole wavefunctions of the first two excited states does not change (it changes at d=32 Å). This means a larger electron contribution to the Coulomb interaction energy of the excited states in comparison to the heavy-hole one. When the crossing point of the heavy-hole excited states is reached (see the left vertical line), the second abrupt jump in the Coulomb energy is observed. However, because of the spill-over of the electron wavefunction of the second excited state (there is no spill-over effect observed for the heavy-hole excited states), the absolute value of the Coulomb energy E_2 decreases after this crossing. Therefore, the Coulomb energy E_2 becomes smaller in absolute value than the value of E_1 for d<30 Å. Close and at the crossing points, *i.e.* d=32 Å and 37.4 Å, there

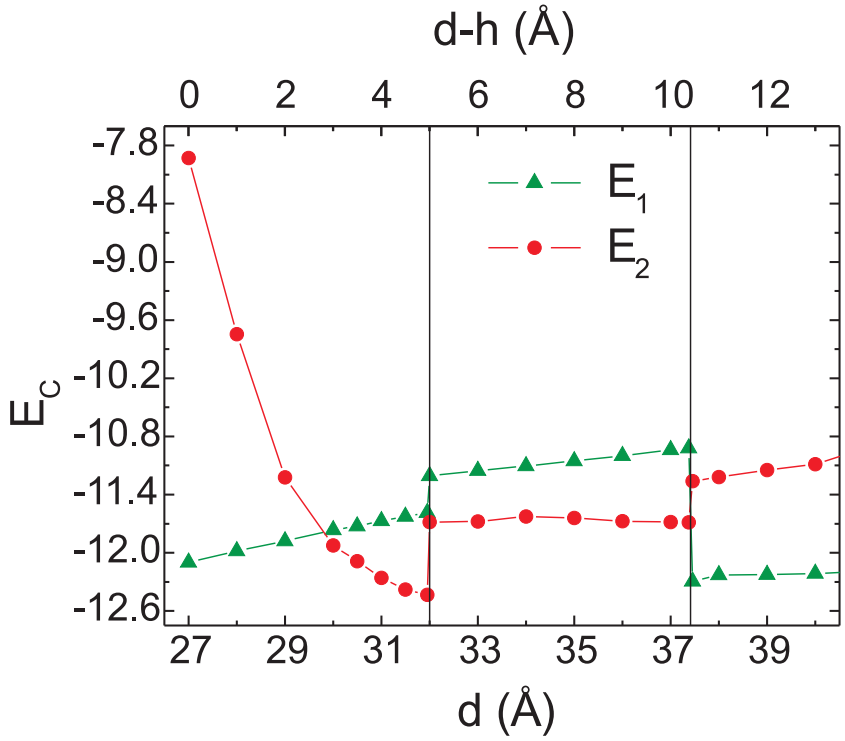

Fig. 6.7: The electron-heavy-hole Coulomb interaction energy as a function of distance d between the wires in InAs/InP vertically CQWRs with height h=27 Å and width w=100 Å. The curves with the triangles (green) and circles (red) correspond to the Coulomb interaction energy between the particles in the first and second excited state, respectively. The top scale, $d-h$, in the graphs is the distance between the edges of two vertically CQWRs (see Fig. 6.1(b)).

will be a strong Coulomb interaction induced mixing of the energy levels which should be included. For this reason we took the electron (hole) wavefunction as a linear combination of the first and the second excited state wavefunction

$$\Psi_{e(h)} = (a\Psi_{1e(h)} + \Psi_{2e(h)})/\sqrt{1+|a|^2}, \tag{6.12}$$

where 'a' is a weighting parameter which is taken as a variational coefficient that minimizes the total exciton energy. In Fig. 6.8 we plot the exciton energy dependence of the first two excited states on the inter-wire distance d between two vertically aligned CQWRs. The results of the two different methods are presented: by solving the single-particle Schrödinger equations; and by using the variational technique. In the first one, as was already mentioned in Sect. II, the wavefunction in the xy-plane for the first (second) excited state of the

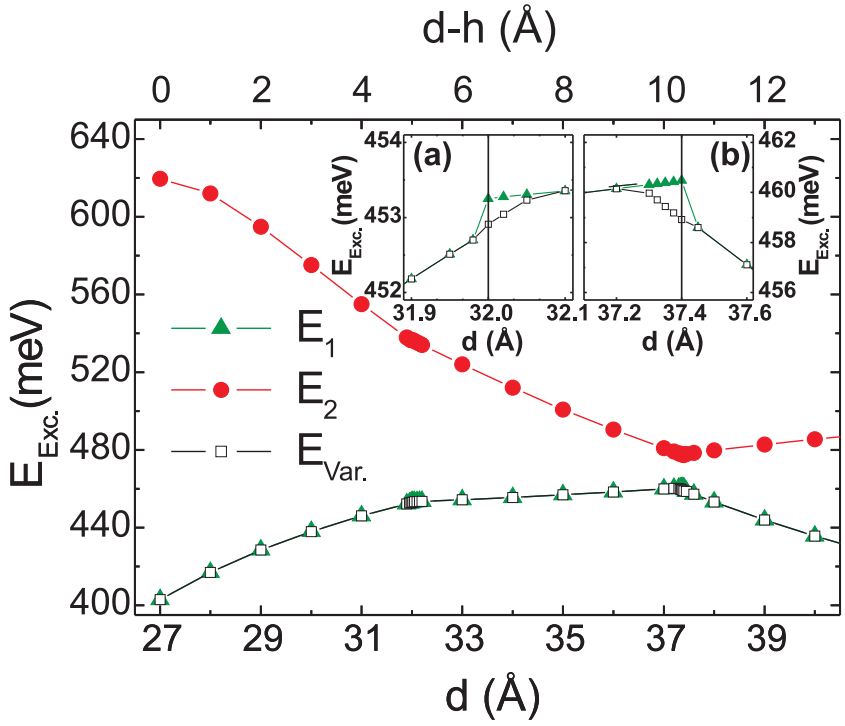

FIG. 6.8: The heavy-hole exciton energy as a function of distance d between the wires in InAs/InP vertically CQWRs with height h=27 Å and width w=100 Å. The curves with the full triangles (green) and full circles (red) correspond to the exciton first and second excited state energies, respectively. The curve with the open squares (black) correspond to our variational calculation. The top scale, $d-h$, in the graphs is the distance between the edges of the two vertically CQWRs. The inset shows the exciton energy near the crossing of the first and the second excited states for heavy-hole (a) and electron (b)(see Figs. 6.6(a) and 6.6(b)).

exciton is assumed as the product of the wavefunction of the electron and the heavy-hole in the first (second) excited state. Then, the total exciton energy of the first (second) excited state equals $E_{Exc.,1(2)}$=$E_{e,1(2)}$+$E_{hh,1(2)}$+$E_{c,1(2)}$. In the second approach, the total exciton wavefunction in the xy-direction is taken as

$$\Psi(x_e, y_e, x_h, y_h, a, b) = \Psi_e(x_e, y_e, a)\Psi_h(x_h, y_h, b), \tag{6.13}$$

using the new wavefunctions (see Eq. (6.12)). Then, we average the kinetic part and the Coulomb interaction part in the exciton Hamiltonian (see Eq. (6.1)). After this averaging we obtain the 1D Schrödinger equation for the relative exciton motion in the z-direction, where the single particle energies E_e

$+ E_{hh}$ are now replaced by $|a|^2E_{e,1}+E_{e,2}+|b|^2E_{hh,1}+E_{hh,2}$ and the effective potential becomes now

$$U_{eff}(z,a,b) = N\int dx_e dy_e dx_h dy_{hh}(|a|^2|b|^2|\Psi_{1e}|^2|\Psi_{1h}|^2 + |a|^2|\Psi_{1e}|^2|\Psi_{2h}|^2 + |b|^2|\Psi_{2e}|^2|\Psi_{1h}|^2 + |\Psi_{2e}|^2|\Psi_{2h}|^2) \times \left(-\frac{e^2}{\varepsilon|\mathbf{r}_e-\mathbf{r}_h|}\right), \quad (6.14)$$

where $N = 1/((1+|a|^2)(1+|b|^2))$. By numerically integrating this equation and by minimizing the total energy we obtain the exciton energy. From Fig. 6.8 we notice an anti-crossing for the exciton excited state energies at d=37.4 Å, where the crossing of the first two excited states for the electron was found. However, at the point d=32 Å both energies slightly change their behavior. The slope of the curves of these exciton energies change insignificantly (see the curves E_1 and E_2 near d=32 Å in Fig. 6.8). Hence, the crossing of the electron first and the second excited state energies leads to the anti-crossing of the exciton first and the second excited state energies, but the crossing of the heavy-hole first two excited states does not affect much the exciton excited state energies. Moreover, we see full agreement in the whole inter-wire region d between the energy calculated by the variational method and between the first excited state energy of the exciton. It is expected, since we always get the first excited state energy of the exciton after minimization of the electron and heavy-hole terms with the first and second excited state energies, and the terms with the Coulomb interaction energy. However, near the crossing of the excited states of the electron and the heavy-hole, the exciton first excited state energy differs by less than 2 meV from the one calculated from the variational technique (see the insets (a) and (b) of Fig. 6.8). At the crossing points there are abrupt jumps for the curve E_1, resulting from the jump in the Coulomb interaction energy for the first excited state (see Fig. 6.7), while continuous behavior is found for the variational calculation results (see the curve with the open squares in the insets of Fig. 6.8). This is because near these crossings the difference between the energies of the excited states of the electron and the heavy-hole becomes smaller than the difference between the Coulomb interaction energies of the excited states.

6.5 CONCLUSIONS

We investigated the coupling in InAs/InP horizontally and vertically CQWRs. The calculation are performed within the single-band effective mass approximation. The strain effect on the band offsets, the mass mismatch in the barrier and the wire, and the Coulomb interaction between the electron-hole pair are included. We found that the heavy-hole state is the ground state.

The PL energy for horizontally coupled InAs/InP wires was calculated as function of the wire height at fixed width. From comparison with the observed PL energies we derive the height of the quantum wire which is in good agreement with those from the experimental XTEM measurements. No inter-wire coupling of the exciton in the experimentally grown InAs/InP self-assembled quantum wires with period d=180 Å was found. Such coupling effects is predicted to show up when the distance d between the wires is smaller than 160 Å.

Numerical results for InAs/InP horizontally coupled system show one coupling regime for all inter-wire distances between the wires. However, for vertically CQWRs a crossing between the excited states for the particles is predicted when the distance between the wires approaches the value of the wires heights. Due to this crossing two coupling regimes for InAs/InP vertically CQWRs are found. In the first coupling regime the electron, heavy- and light-hole densities for the lowest levels have the same behavior as in a single square wire, while in the second coupling regime both the energies and densities for the lowest levels act as in ordinary coupled wires.

Anti-crossing for exciton excited state energies in vertically CQWRs is predicted for the inter-wire distance where the crossing of the first and the second excited states for the electron is found. Exciton excited state energies are slightly affected when the symmetry of the wavefunction of heavy-hole excited states in vertically CQWRs changes. In a PL experiment the heavy-hole exciton line is bright while the corresponding one for the light-hole is dark due to a selection rule. Therefore, we did not present results for the light-hole exciton.

Publications. The results in this chapter were published as:

- Y. Sidor, B. Partoens, F. M. Peeters, T. Ben, A. Ponce, D. L. Sales, S. I. Molina, D. Fuster, L. González, and Y. González, *Excitons in coupled InAs/InP self-assembled quantum wires*, Phys. Rev. B **75**, 125120 (2007).
- The paper Phys. Rev. B **75**, 125120 (2007) was also selected for the April 9, 2007 issue of Virtual Journal of Nanoscale Science & Technology.

7

High-field magneto-excitons in unstrained $GaAs/Al_xGa_{1-x}As$ quantum dots

7.1 INTRODUCTION

Excitonic properties in quantum nanostructures have been intensively investigated over the past decade because of the high potential for applications and fundamental physics [1, 3, 6]. Among these nanostructures, quantum dots are three-dimensional wells that can trap electrons and holes resulting in quantized energy levels. The density of states is δ function-like, and the wavefunction of the particles is localized inside the dot. Therefore, excitons play an important role for the optical properties in such QDs. To explore these QD properties, optical spectroscopy experiments in the presence of an external magnetic field is a good probing tool [179, 180].

Semiconductor QDs can be grown by many methods, but in most cases are based on lithography and self-organization techniques. Self-assembled QDs formed through the Stranski-Krastanow growth mode, among the various 0D systems investigated so far, are the most well studied QDs. They can be fabricated with high uniformity and in a single layer (or in arrays of vertically aligned stacks). The optical properties of self-assembled QDs in the presence of an external magnetic field have been studied theoretically and experimentally by several groups. Early experimental work on InAs self-assembled QDs by Zhu *et al.* [181] and also by several other groups [113, 179, 182, 183] observed the excitonic properties of different self-assembled dots in the presence

of parallel and perpendicular magnetic fields. One should mention the interesting experimental and theoretical work done by Bayer *et al.* [184], where self-assembled dots were investigated in magnetic fields of varying orientations. Theoretical approaches, based on a harmonic oscillator confinement potential and perturbation theory (see for example Ref. [185]) have been presented in order to calculate the diamagnetic shift of the exciton ground state energy and to compare with the experimental data. Excited states in the dot were studied previously (see for example Refs. [114, 116, 186, 187]), both experimentally and theoretically by Raymond *et al.* [188] and in another experimental work by Pulizzi *et al.* [189]. In the work by Raymond *et al.* valence band mixing was included within the eight-band $\mathbf{k}\cdot\mathbf{p}$ model, coupled via the Bir-Pikus Hamiltonian to the strain of the dot calculated using classical elasticity theory. Very recently, experimental and theoretical results within the single band effective mass approximation including strain were presented in the absence of an external magnetic field, where the dot structure was taken directly from the experiment (possibly full 3D calculations). The ground state photoluminescence energy of the InAs/AlAs and InAs/GaAs QDs was calculated [190].

GaAs/AlGaAs QDs cannot be created by Stranski-Krastanov growth because of the almost perfect match of lattice parameters. Nevertheless, this system offers several advantages compared to others: the grown material is ideally unstrained, and sharp interfaces with reduced intermixing can be obtained; they can be designed to emit light in the optimum spectral range of sensitive Si-based detectors. A new experimental method was presented recently to obtain GaAs/AlGaAs quantum dots via multistep (hierarchical) self-assembly. First a template of InAs/GaAs islands was created, which are "converted" into nanoholes on a GaAs surface by GaAs overgrowth followed by in situ etching. Self-assembled nanoholes are then transferred to an $Al_xGa_{1-x}As$ surface, filled with GaAs, and overgrown with $Al_yGa_{1-y}As$ ($x > y$). In this case the quantum dot morphology is given by the shape of the $Al_xGa_{1-x}As$ nanoholes [191]. This allows the electronic properties of the QDs to be calculated without the complication of uncertain composition and strain profiles [191–193]. The GaAs QDs are characterized by widely tunable emission energy, narrow inhomogeneous broadening (of the order of 8-20 meV depending on the growth parameters) and large separation between QD emission and continuum (up to $\sim$200 meV). Single-QD spectroscopy on such QDs show resolution-limited sharp lines [191], single-photon emission up to 77 K and bright emission up to room temperature.

In this chapter we focus our attention on the energy spectrum of single excitons in the presence of an applied magnetic field for such GaAs/$Al_xGa_{1-x}As$ QDs [191]. We perform calculations within the single band effective mass approximation but including band nonparabolicity in first order approximation. The real experimental shape of the dot with a quantum well on the top and asymmetrical AlGaAs barriers is considered. The calculations are based on a full 3D finite element scheme. We study the exciton energy shift for the ground

and the excited states of the QD in magnetic fields up to 50 T of varying orientation.

The chapter is organized in the following way. In Sec. 7.2 we briefly describe the method and the QD model used in our calculations. In Sec. 7.3 we discuss the Coulomb interaction energies and the wavefunction extensions of the particles in the presence of a magnetic field. Finally in Sec. 7.4, we present results of the influence of a magnetic field on the excitonic spectrum in GaAs/Al_xGa_{1-x}As QDs, comparing theoretical and experimental data.

7.2 THEORETICAL FORMALISM AND MODEL

The geometry of the quantum dot was taken directly from scanning tunneling microscopy (STM) measurements. The profile of the 3D dot is illustrated in Fig. 7.1. On top of the GaAs dot-well system, an $Al_{0.35}Ga_{0.65}As$ barrier was deposited, while on the bottom $Al_{0.45}Ga_{0.55}As$. Therefore, this structure is slightly non-symmetric due to the different barriers. Figure 7.1 also shows the height (h) distribution in the 2D lateral profile of the dot with the base widths w_x and w_y. According to it, the dot is more elongated along the y-direction, and the height distribution is not uniform with respect to the center of the xy-plane.

The conduction and the valence bands are centered around the Γ-valley of GaAs and $Al_xGa_{1-x}As$. Within the single band effective-mass theory, in order to describe electron and hole states of the dots, we solve the Schrödinger equations

$$H\Psi(\mathbf{r_e}, \mathbf{r_h}) = E\Psi(\mathbf{r_e}, \mathbf{r_h}), \tag{7.1}$$

with the Hamiltonian

$$H = H_e + H_h + U(\mathbf{r_e} - \mathbf{r_h}), \tag{7.2}$$

where $H_{e(h)}$ denotes the single electron (hole) Hamiltonian, $U(\mathbf{r_e} - \mathbf{r_h})$ is the Coulomb interaction between the electron and the hole

$$U(\mathbf{r_e} - \mathbf{r_h}) = -\frac{e^2}{\varepsilon|\mathbf{r_e} - \mathbf{r_h}|}, \tag{7.3}$$

where e is the charge of the electron, and ε is the static dielectric constant taken as the value of GaAs, because of the very small difference of ε inside and outside the dot (see Table 7.1).

In the presence of a magnetic field the momentum is replaced by the expression $\mathbf{p} \to \mathbf{p} - \frac{q}{c}\mathbf{A}$, so that the kinetic operator for the particles becomes

$$T = \left(\mathbf{p} - \frac{q}{c}\mathbf{A}\right)\frac{1}{2m^*}\left(\mathbf{p} - \frac{q}{c}\mathbf{A}\right), \tag{7.4}$$

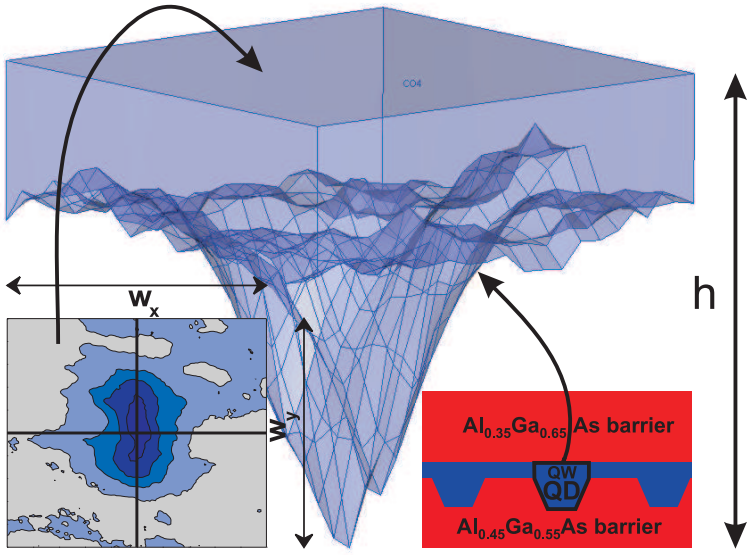

FIG. 7.1: Geometry of the GaAs/Al$_x$Ga$_{1-x}$As QD, as measured by STM topography. The height h=6.45 nm and base widths along x- and y-directions w_x=56 nm and w_y=72 nm, respectively (x-direction corresponds to the [1-10] crystal direction of GaAs). On the top of the dot a thin QW layer is deposited (for details see Ref. [191]).

where q is the charge of the particle, m^* is the spatial dependent mass of the particle and $\mathbf{A}$ is the vector potential. Let us consider the case, when the magnetic field is applied along an arbitrary direction. We choose the symmetric gauge

$$\begin{aligned}\mathbf{A} &= -\frac{1}{2}\mathbf{r}\times\mathbf{B} \\ &= \frac{1}{2}((B_y z - B_z y)\hat{x} + (B_z x - B_x z)\hat{y} + (B_x y - B_y x)\hat{z}),\end{aligned}$$

where B_x, B_y and B_z are the components of the magnetic field along x-, y- and z-directions, respectively, given by

$$\begin{aligned}B &= (B_x, B_y, B_z) \\ &= B\,(\cos(\varphi)\sin(\theta), \sin(\varphi)\sin(\theta), \cos(\theta))\,,\end{aligned} \tag{7.5}$$

where ($0 \le \theta \le \pi$, $0 \le \varphi \le 2\pi$). Inclusion of the magnetic field leads to fifteen additional diamagnetic terms in the kinetic term, in addition to $\mathbf{p}(1/(2m^*))\mathbf{p}$.

From them, twelve are linear with respect to B_i, r_i and ∇_i (i=x, y and z; here and further we will use r_x=x, r_y=y and r_z=z), and three other are quadratic

$$C \sum_{i(j,k)=x}^{y,z} \frac{(B_i r_j - B_j r_i)^2}{m_k^*}, \tag{7.6}$$

where the constant $C = q^2/(8c^2)$, and m_k^* are the position dependent components of the effective mass tensor.

In the QD structure the subband energy due to the z-confinement is typically of the order of 100 meV. Therefore, the anisotropy and the corrections due to the conduction band nonparabolicity are important [194]. The electron Hamiltonian is

$$\begin{aligned} H_e(r_e) &= -\nabla_{xe}\frac{\hbar^2}{2m^*_{\|e}(\mathbf{r}_e)}\nabla_{xe} - \nabla_{ye}\frac{\hbar^2}{2m^*_{\|e}(\mathbf{r}_e)}\nabla_{ye} \\ &\quad -\nabla_{ze}\frac{\hbar^2}{2m^*_{\perp e}(\mathbf{r}_e)}\nabla_{ze} + V_e(\mathbf{r}_e) + V_{eB}(\mathbf{r}_e), \end{aligned} \tag{7.7}$$

where $V_e(r_e)$ is the conduction band offset and we took the asymmetry of the AlGaAs barriers and the geometry of the dot into account (see Fig. 7.1). $V_{eB}(r_e)$ denotes the aforementioned electron diamagnetic terms, $m^*_{\|e}$ and $m^*_{\perp e}$ are the perpendicular and parallel effective masses of the electron, which we obtain from the first order nonparabolicity approximation [150]

$$m^*_{\perp e} = m^*_e(1 + \alpha E), \tag{7.8}$$

$$m^*_{\|e} = m^*_e(1 + (2\alpha + \beta)E), \tag{7.9}$$

where m^*_e is the bulk electron masses of the material, α and β are the nonparabolicity parameters (see Table 7.1), and E is the ground state energy of the electron obtained by solving the single particle Schrödinger equation using the bulk masses of the electron. The parallel mass determines the electron energy in the xy-plane, and the perpendicular mass determines the quantization energy of the electrons in the z-direction.

We consider both the heavy- and the light-hole states in our calculation. The strain is not included because the QD structure is unstained due to the experimental growth conditions [191]. The single particle Hamiltonian for both holes (h) is

$$\begin{aligned} H_h(r_h) &= -\nabla_{xh}\frac{\hbar^2}{2m^*_h(\mathbf{r}_h)}\nabla_{xh} - \nabla_{yh}\frac{\hbar^2}{2m^*_h(\mathbf{r}_h)}\nabla_{yh} \\ &\quad -\nabla_{zh}\frac{\hbar^2}{2m^*_h(\mathbf{r}_h)}\nabla_{zh} + V_h(\mathbf{r}_h) + V_{hB}(\mathbf{r}_h), \end{aligned} \tag{7.10}$$

Table 7.1: Material parameters used in the calculations: band gap E_g, electron mass m_e (Ref. [126]), Luttinger parameters γ_1 and γ_1, nonparabolicity parameters α and β (Ref. [150]), and dielectric constant ε (Ref. [131]). For $Al_xGa_{1-x}As$ material parameters, the first-order interpolation formula is used: parameter($Al_xGa_{1-x}As$)=parameter(GaAs)$\pm x$(parameter(GaAs)-parameter(AlAs)).

Parameter	GaAs	$Al_{0.35}Ga_{0.65}As$	$Al_{0.45}Ga_{0.55}As$
E_g (eV)	1.519	1.956	2.080
m_e (m_0)	0.067	0.096	0.104
γ_1	6.98	5.85	5.53
γ_2	2.06	1.63	1.50
α (eV^{-1})	0.64	–	–
β (eV^{-1})	0.70	–	–
ε	12.9	11.9	11.6

where m_h^* is the effective masses of the hole, $V_h(r_h)$ is the valence band confinement offset of the hole, $V_{hB}(r_h)$ denotes the hole diamagnetic terms. Note that this single particle Hamiltonian is not just the diagonal part of the four-band **k·p** Hamiltonian. The mass in each direction is the same and corresponds to the curvature of the hole bands around the Γ point, *i.e.*, for the heavy-hole and the light-hole, respectively

$$\frac{m_0}{m_{hh}^*} = \gamma_1 - 2\gamma_2, \tag{7.11}$$

$$\frac{m_0}{m_{lh}^*} = \gamma_1 + 2\gamma_2, \tag{7.12}$$

where γ_1 and γ_1 are Luttinger parameters (see Table 7.1), and m_0 is the vacuum electron mass.

To include the Coulomb interaction between the electron and the hole in the QD, we calculate the Hartree potential $\varphi(r)$ by solving the 3D Poisson equation:

$$\varepsilon\nabla^2\varphi(\mathbf{r}) = -4\pi\rho(\mathbf{r}), \tag{7.13}$$

where $\rho(\mathbf{r})$ is the particle density, previously calculated from Eq. (7.1). The potential $\varphi(\mathbf{r})$ is the one felt by the hole, *i.e.*, in mathematical terms it means $\varphi(\mathbf{r}_h) \approx \int d\mathbf{r}_e \rho(r_e)/|\mathbf{r}_e - \mathbf{r}_h|$. To solve the Poisson equation, often one uses zero as the boundary condition, which is a good approximation when a large

enough grid is used. The regular asymptotic boundary condition to the Poisson equation is proportional to $1/r$. Note, because the dot profile is not symmetric, consequently the density of the electron is not symmetric, and therefore the exact asymptotic boundary condition for the last equation becomes

$$\varphi(\mathbf{r}_e) = \frac{q}{\varepsilon|\mathbf{r}_e - \mathbf{r}_{0e}|}, \tag{7.14}$$

where $\mathbf{r}_{0e} = \int \mathbf{r}_e \rho(\mathbf{r}_e) d\mathbf{r}_e$ is the average value of the coordinates of the electron, and q is the electron charge. The Coulomb energy, which accounts for the interaction between the electron-hole pair, is obtained by performing 3D integration over the hole coordinates

$$E_C = \int \varphi(\mathbf{r}_h)\rho(\mathbf{r}_h) d\mathbf{r}_h, \tag{7.15}$$

where $\rho(r_h)$ is the hole density. Note, that by solving the Poisson equation we circumvent the direct 6D integration over electron and hole space, and we avoid the 1/r singularity problem for r $\rightarrow$ 0.

The full 3D calculations with the real shape of the dot in the presence of the magnetic field, as well as the Poisson equation are performed using the finite element method on a variable size grid. The input parameters used in the simulations are presented in Table 7.1. Most of the parameters have been taken from Ref. [98], otherwise indicated.

7.3 EXTENT OF THE PARTICLES AND THE COULOMB ENERGIES

In this section we discuss the electron-hole interaction and the wavefunction extensions of the particles in the presence of a magnetic field. *One should stress, that there are no fitting parameters in all our calculations.*

The mass of the heavy-hole inside the dot, is equal to $0.35m_0$, and is four times larger than the mass of the light-hole $0.09m_0$ (see Eq. (7.11), Eq. (7.12) and Table 7.1). As a result, the wavefunction radii in the xy-plane of the heavy-hole for zero magnetic field $\mathbf{B}$ are smaller than for the light-hole, as can be seen from Fig. 7.2. However, one can notice that the electron extent is smaller than for the light-hole. The reason is that, although the electron mass is a bit lighter than the one of the light-hole, the conduction band offset is roughly 1.5 times larger than the offset for the light-hole. Let us comment on the behavior of the particle radii in the case when the magnetic field is applied along the z-direction. The magnetic field influences the particle motion in the plane perpendicular to the applied direction. When the magnetic field is applied along the z-direction (influence on the xy-plane), the 2D radii in the xy-plane are strongly squeezed for all particles (see full curves in Fig. 7.2), and

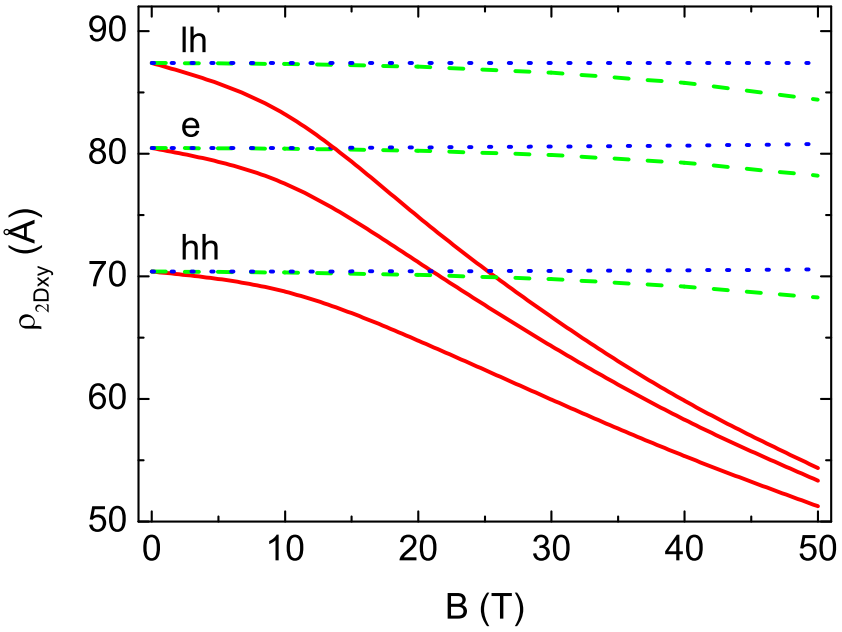

FIG. 7.2: The extent of the electron (e), the heavy-hole and the light-hole in the xy-plane, as a function of the magnetic field $\mathbf{B}$ for GaAs/Al$_x$Ga$_{1-x}$As QD. The dashed (green), dotted (blue), and full (red) curves correspond to the radii, when the magnetic field is applied along the x-, y-, and z-direction, respectively.

it leads to a decrease of at least 30 % (even more for the light-hole). This large change is due to the flatness of the dot, with a lateral dimension about 10 times larger than its height. This is the reason why the magnetic field applied along the x- and y-directions has a less pronounced effect on the electron and holes 2D extension (see dashed and dotted curves in Fig. 7.2, respectively). The dot is slightly larger in the y-direction which explains the small difference between the dashed and dotted curves in Fig. 7.2.

Radii along the z-direction are significantly smaller than those in the plane, as depicted in Fig. 7.3. The electron radius is smaller than the one for the light-hole, because of the difference of conduction and valence band offsets. When the magnetic field is applied along the z-direction, the wavefunction is squeezed in the plane of the dot, as was already observed, but at the same time it will become elongated in the z-direction (full curves in Fig. 7.3), because the total particle probability is a constant. This is similar to squeezing a balloon in two directions. In the case of the magnetic field applied along the x- and

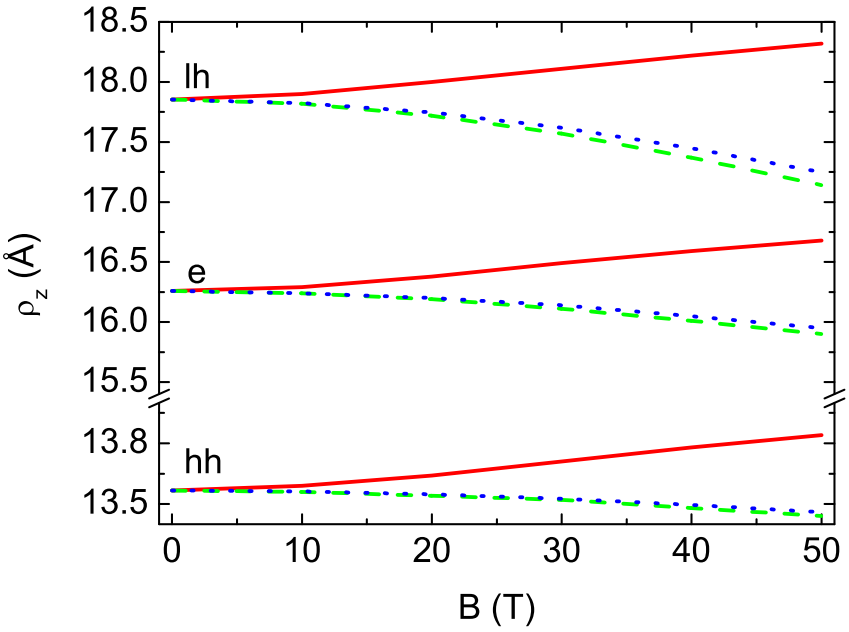

Fig. 7.3: The same as Fig. 7.2 but now in the z-direction.

y-directions (dashed and dotted curves in Fig. 7.3, respectively), the particle radii slightly decrease with increasing magnetic field due to the squeezing of the wavefunction in, respectively, the yz- and xz-plane.

The dependence of the electron-hole Coulomb interaction on the external magnetic field is shown in Fig. 7.4. As was mentioned in Sect. 7.2, one can use different boundary conditions for the Poisson equation. In the inset of Fig. 7.4 we show that by using the boundary condition described by Eq. (7.14) and the one with zero boundary conditions may influence the Coulomb interaction energy slightly. The absolute value of the Coulomb interaction is inversely proportional to the relative distance between the electron and the hole. The radii for all the particles in the xy-plane are much larger than that along the z-direction. Therefore, the interaction between the electron and the hole is predominantly determined by the behavior of the particle radii in the xy-plane (compare Figs. 7.2, 7.3 and 7.4), *i.e.*, for the magnetic field applied along the z-direction an increase of the absolute value of the Coulomb energy for both electron-heavy-hole and electron-light-hole pairs is observed. Only a very small increase with applied magnetic field along the plane of the dot (see the dashed and dotted curves with circles and squares in Fig. 7.4) is seen.

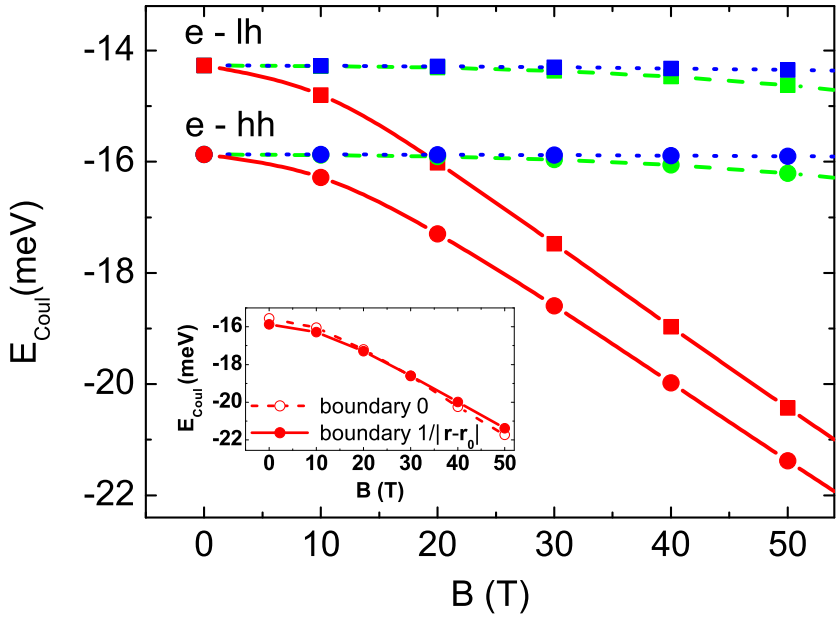

FIG. 7.4: The electron-hole Coulomb interaction energy as a function of magnetic field for GaAs/Al$_x$Ga$_{1-x}$As QD. The dashed (green), dotted (blue), and full (red) curves with the circles correspond to the heavy-hole-electron Coulomb energies, for the magnetic field applied along the x-, y-, and z-direction, respectively. The curves with the squares represent the light-hole-electron Coulomb interaction energies. The inset shows the Coulomb energy, as a function of magnetic field applied along the z-direction. The dashed (full) curves with the open (closed) circles correspond to the two different boundary conditions of the Poisson equation.

7.4 MAGNETO-EXCITON TRANSITIONS AND COMPARISON BETWEEN THEORY AND EXPERIMENT

In this section we investigate the exciton diamagnetic shift of the dot. We perform our simulations for both heavy- and light-hole states and compare them with the experimental data. The experimental data are obtained by photoluminescence measurements in pulsed magnetic fields up to 50 Tesla (see Fig. 7.5). The experiments were carried out in a He^4-bath cryostat at 4.2 K, using an argon-ion laser at a wavelength of 514 nm to excite the electrons. The PL was analysed by a spectrometer and an intensified charged-coupled-device detector, using an integration time of 0.5 ms. The peak positions of

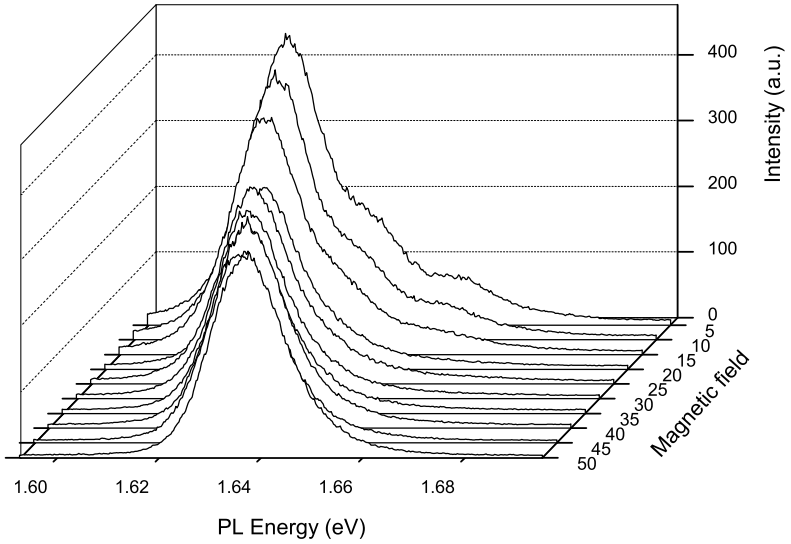

Fig. 7.5: Photoluminescence spectra as a function of magnetic field applied parallel to the z-direction. The peak positions of ground and excited states are obtained by gaussian fits.

the PL spectrum are obtained by gaussian fits to the experimental spectra. The measured PL ground state energy versus field dependence can be fitted with an excitonic model, using three parameters: the zero field PL energy, exciton wavefunction radius and the exciton mass. The exciton radius in the xy-plane obtained with the fitting procedure from the experimental data of 7.6 nm is in good agreement with the calculated electron radius as described in the previous section. A detailed description of the experimental set-up and analysing method can be found in Ref. [180].

In Fig. 7.6 we examine the diamagnetic shift of the ground state exciton energy, with and without taking into account the Coulomb interaction, when the magnetic field is applied along the z-direction. From Fig. 7.6 we can immediately notice the importance of including the Coulomb interaction energy (compare full and dashed curves). The resulting diamagnetic shift is inversely proportional to the reduced mass of the electron and hole. The heavy-hole mass is four times larger in the xy-plane of the dot than the light-hole. Consequently, the resulting heavy-hole diamagnetic shift is smaller than the light-hole diamagnetic shift, when the magnetic field is applied along the growth direction ($\mathbf{B}//\hat{z}$). Up to 35 T the calculated diamagnetic shift energies for the

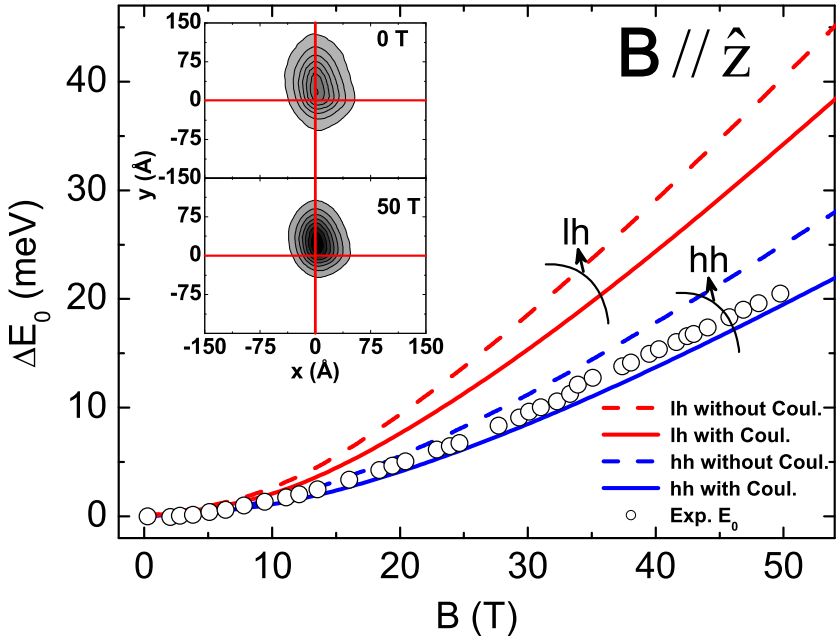

FIG. 7.6: The diamagnetic shift of the exciton ground state energy, as a function of a magnetic field along the z-direction for GaAs/Al$_x$Ga$_{1-x}$As QD. The full and dashed curves correspond to the heavy-hole and the light-hole excitons with and without taking into account the Coulomb interaction. The inset shows the contour plot of the electron density at magnetic field 0 and 50 T.

heavy-hole states are in very good agreement with the experimental data. At 50 T the disagreement between theory and experiment is less than 1 meV. If we exclude the nonparabolicity of the electron mass the disagreement between the theoretical heavy-hole exciton and the experiment at 50 T is 3 meV. In the inset of Fig. 7.6 we show a contourplot of the electron density which illustrates the asymmetry of the electron density regarding the xy-center. The zero magnetic field PL energies for the heavy-hole state is E_{PLhh}=1614 meV, which compares to the experimental PL energy $E_{PLExp.}$=1620 meV, while for the light-hole we found E_{PLlh}=1652 meV. We neglected the Zeeman effect in our calculations, since even at the highest magnetic field it gives only a small contribution. Taking the g_{ex}-factor for the exciton equal to 0.51 [195], the Zeeman splitting energy between the states with the spin up and down is only $g_{ex}\mu_B B \approx 1.5$ meV at 50 T, where μ_B is the Bohr magneton.

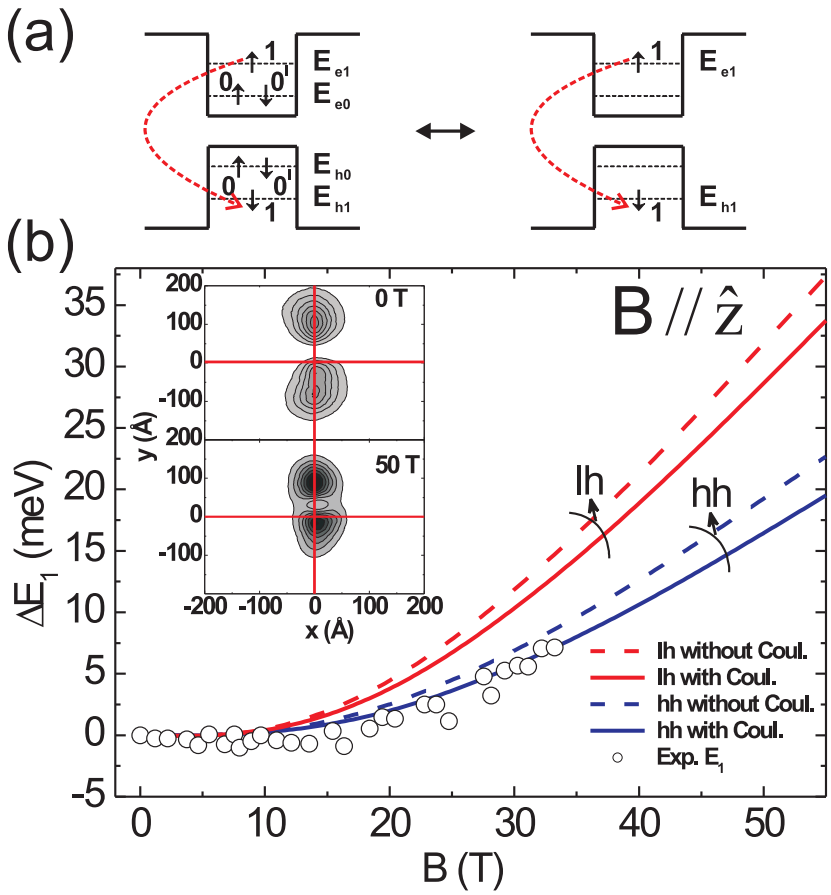

Fig. 7.7: (a) Schematic of the excitonic levels for the first excited state. (b) The diamagnetic shift of the first excited exciton state, as a function of magnetic field applied along the z-direction for GaAs/Al_xGa_{1-x}As QD. The full and dashed curves correspond to the heavy-hole and the light-hole excitons with and without taking into account the Coulomb interaction. The inset shows the contour plot of the electron density of the first excited state at magnetic field 0 and 50 T.

Figure 7.7(b) shows the exciton diamagnetic shift of the first excited state in the presence of a magnetic field applied along the z-direction. In the experiment, the PL intensity of the first, and particulary the second, excited states is quenched with magnetic field, such that experimental data is only available up to 35 and 10 T for the first and second excited states respectively.

Our calculations demonstrate that there is an enhancement of the electron-hole wavefunction overlap with magnetic field (not shown). Thus, since the intensity of the ground state PL also becomes slightly less intense with magnetic field, this implies that electron-hole pair capture by the dots is suppressed at high fields. Theoretically, we investigate both heavy- and light-hole exciton states with and without taking into account the electron-hole interaction. In the whole magnetic field region of available experimental data, up to 35 T, we again see a quantitative agreement with the heavy-hole diamagnetic shift when including the Coulomb interaction. Comparing the PL energies, the heavy-hole state is also closer to the experimental PL energy $E_{PLExp.}$=1638 meV, E_{PLhh}=1630 meV and E_{PLlh}=1673 meV. Furthermore, if we compare the heavy-hole PL energy difference between the first excited state and the ground state $\triangle E_{PLhh(1,0)}$=16 meV with the experimental values $\triangle E_{PLExp.(1,0)}$=18 meV, it gives further support to our claim that the heavy-hole exciton is the ground state. In the inset of Fig. 7.7(b) we illustrate the electron densities of the first excited state for a magnetic field of 0 and 50 T.

The exciton energy was calculated, as $E_{ex,i}=E_{e,i}+E_{h,i}-E_{C(ei,hi)}$, where i=0 refers to the ground state, i=1 to the first excited state, and so on; and $E_{C(ei,hi)}$ is the Coulomb interaction between the electron-hole (heavy- and light-holes) pair in the i-th state. Knowing this exciton energy, we calculate the exciton diamagnetic shift energy $\triangle E_i$. One should stress, that we assume the recombination between electron and hole of the same quantum state, namely, electron and hole are either both in the ground state or in the first or second excited state, which is experimentally and theoretically justified [186–189] on the basis of selection rules. Moreover, we consider the possibility of multiexcitonic transitions. Let us compare two situations (1) each particle is in the first excited state (see the right graph in Fig. 7.7(a)), which corresponds to the first excited state of the exciton, and (2) the two identical particles (electron or hole) with spin up and down are in the ground state and one in the first excited state (see the left graph in Fig. 7.7(a)), which corresponds to the ground state of the three exciton-line. In the first case we have for the diamagnetic shift for the excited exciton the following terms $\triangle E_{e1} + \triangle E_{h1} - E_{C(e1,h1)}$. In the second case, instead of $-E_{C(e1,h,1)}$ appears $2E_{C(e0,e1)} + 2E_{C(h0,h1)} - 2E_{C(e0,h1)} - 2E_{C(e1,h0)} - E_{C(e1,h1)}$. Here $E_{C(e0,e1)}$ is the electron correlation energy of the ground and first excited states, $E_{C(h0,h1)}$ is the hole correlation energy, and the rest are the Coulomb interaction energies between the ground and first excited states of the particles. We computed the aforementioned correlation and Coulomb interaction energies for the heavy-hole state, as an example, in order to estimate the distinction. However, we found that the difference between the first excited state of the single exciton transition and the ground state of the three exciton-line transition is very small. It is less than 1 meV at zero magnetic field, and about 1 meV at 50 T. The same situation arises if we compare the ground state of the exciton (electron and hole are in the ground state) and the

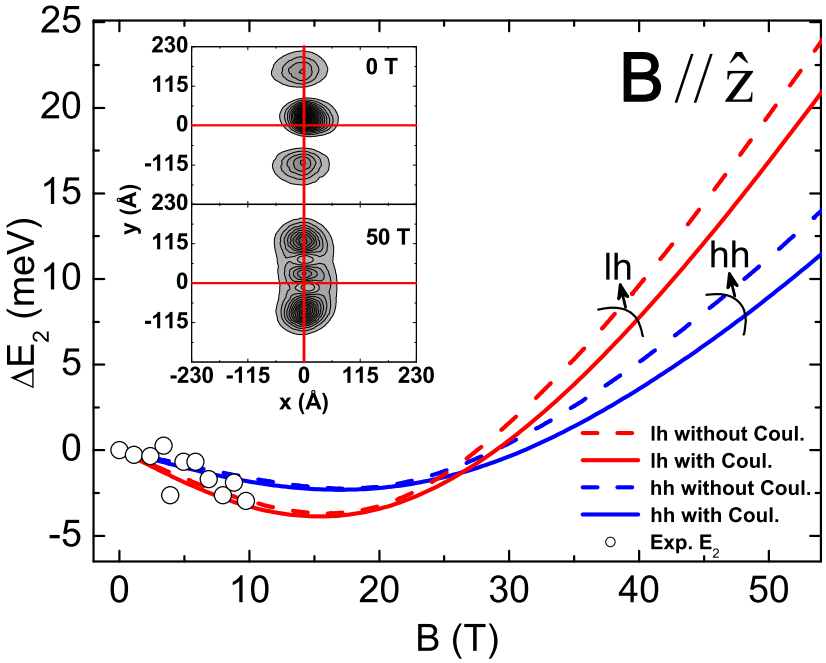

Fig. 7.8: The same as Fig. 7.6 but now for the second excited state.

ground state of the two exciton-line (two electrons and holes are in the ground state). The difference is also less than 1 meV at magnetic field 0 and 50 T.

Comparison between our theoretical simulations for the exciton diamagnetic shift of the second excited state and available experimental data are shown in Fig. 7.8. Since there are only experimental data for magnetic fields up to 10 T, it is difficult to judge, whether heavy- or light-hole exciton states are in good agreement with the experiment (see curves for the heavy-hole and the light-hole with and without Coulomb interaction). Comparing the PL energies, the heavy-hole state is closer to the experimental PL energy $E_{PLExp.}$=1650 meV, E_{PLhh}=1644 meV and E_{PLlh}=1692 meV. When we compare the heavy-hole PL energy difference between the second excited state and the first excited state with the experimental data, we found that $\triangle E_{PLhh(2,1)}$=14 meV and $\triangle E_{PLExp.(2,1)}$=12 meV, which is another justification that the experimental results correspond with heavy-hole excitons. However, for both hole states we observe a negative diamagnetic shift, with increasing magnetic field for B<15 T, which agrees with the experimental data (see open circles). Let us remember, that including the magnetic field causes an extra parabolic confinement, as

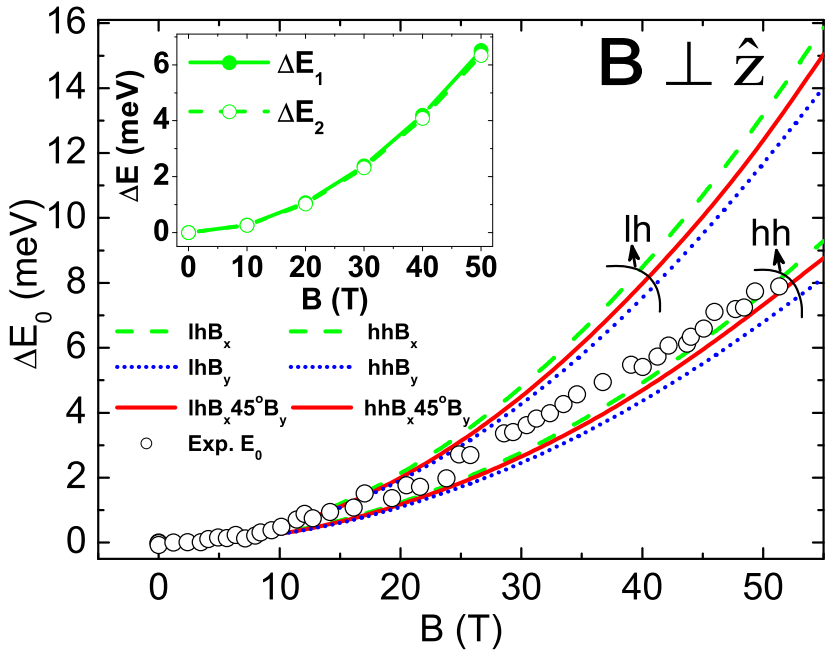

Fig. 7.9: The diamagnetic shift of the exciton ground state, as a function of magnetic field. The dashed (green) and dotted (blue) curves correspond to the heavy-hole and the light-hole excitons, when the magnetic field is applied along the x- and y-direction, respectively. The full (red) curves correspond to the case, when the magnetic field is applied along 45° between xy-direction. The inset shows the heavy-hole exciton diamagnetic shift of the first (E_1) and second (E_2) excited state, when the magnetic field is applied along the x-direction.

described by Eq. (7.7). The well known Fock-Darwin spectrum at small values of the magnetic field, where the 2D harmonic oscillator is considered, shows a small negative dependence of the first excited state energy, which is more pronounced after the crossing of the second and third excited state energies. However, the negative excitonic diamagnetic shift is seen for the second excited state both in the theoretical and experimental results (compare Figs. 7.7 and 7.8). In the inset of Fig. 7.8 the change of the electron density for the second excited state for the magnetic fields of 0 and 50 T is plotted.

We also investigate the exciton diamagnetic shift of the QD in the presence of a magnetic field perpendicular to the z-direction ($\mathbf{B}\perp\hat{z}$). As an example we consider the exciton diamagnetic shift, when the magnetic field is applied along the x-, y-direction, and directed 45° between the xy-direction (see Fig. 7.9).

The Coulomb interaction energy, as was already discussed in Fig. 7.4, has a negligible effect on the magnetic field dependence. For magnetic fields up to 40 T the experimental points are between the heavy- and light-hole curves, and for high magnetic field a good agreement between the experimental points and the theoretical heavy-hole diamagnetic shift is obtained. Within the single band model it is not possible to take into account the coupling between the heavy-hole and the light-hole, which is the most likely reason for the discrepancy at magnetic fields up to 40 T. Note, that there is a large distinction in the diamagnetic field between heavy- and light-hole states. The difference for the magnetic field applied along the x-, y-direction, or 45° between xy-direction is small. The inset of Fig. 7.9 shows the heavy-hole exciton diamagnetic shifts (the light-hole excitons have the same behavior) for the two lowest excited states. The dot confinement is more important than the magnetic confinement at small magnetic field. Hence, we do not observe a negative diamagnetic shift behavior for both excited states.

7.5 CONCLUSIONS

In summary, the excitonic properties in the presence of a magnetic field in unstrained GaAs/$Al_xGa_{1-x}As$ QDs were investigated theoretically and experimentally. In our 3D calculations, within the single band effective mass approximation, we include the effect of band nonparabolicity of the conduction band, the real shape of the QD with the thin well layer on top and asymmetrical barrier materials, as well as heavy- and light-hole states. By solving the Poisson equation with the correct boundary conditions, the Coulomb interaction energy between electron and hole was calculated.

The magnetic field dependence of the electron-hole Coulomb interaction energy, when the magnetic field is applied along x-, y- and z-direction, follows closely the dependencies of the particle radii (*i.e.* size) in the xy-plane of the dot. Radii along the z-direction are significantly smaller due to the flatness of the dot, and with increasing magnetic field along the z-direction the particles wavefunction radii become elongated in the z-direction.

The diamagnetic shift for the exciton ground state and the two first excited states in the presence of a magnetic field applied along x-, y-, and z-direction in the QD are calculated. A good agreement between the experimental results and the calculated heavy-hole exciton is found. By comparing the PL energies, the heavy-hole state is found to be the ground state, and its value is close to the experimental data.

Publications. The results in this chapter were published as:

- Y. Sidor, B. Partoens, F. M. Peeters, N. Schildermans, M. Hayne, V. V. Moshchalkov, A. Rastelli, and O. G. Schmidt, *High-field magnetoexcitons in unstrained GaAs/$Al_xGa_{1-x}As$ quantum dots*, Phys. Rev. B **73**, 155334 (2006).

- The paper Phys. Rev. B **73**, 155334 (2006) was also selected for the May 15, 2006 issue of Virtual Journal of Nanoscale Science & Technology.

Summary

In the present thesis I investigated the excitonic properties in QWRs and related systems, *i.e.* QWs and QDs. The study of excitons in these low-dimensional systems provides valuable information about their characteristics. In particularly, self-assembled InAs/InP QWRs have been experimentally obtained recently, and a further research was needed to study the charge confinement, the dimensions, the uniformity in size, the optical transitions and the coupling in such wires. Our theoretical investigation of excitons helps to determine these characteristics. Therefore, the main attention of this work was given to the excitonic properties in self-assembled InAs/InP QWRs. Additionally, I investigated excitons in V-shaped GaAs/AlGaAs QWRs, the magnetic field dependence of the properties of the neutral excitons in InAs/InP QWs and GaAs/AlGaAs QDs, and the charged excitons in the aforementioned V-shaped and self-assembled wires.

In the first chapter a general introduction to QWRs is given. Possible applications as for example in lasers are discussed, and their different growth techniques are discussed. The effect of strain on the confinement of excitons is discussed, together with the effect of a magnetic field. The single-band effective mass approach that is used throughout this work is introduced.

In the second chapter, I studied the charge confinement in self-assembled InAs/InP QWRs. I compared our simulations with available magneto-PL experimental measurements from the groups in K. U. Leuven and Instituto de Microelectrónica de Madrid. The theoretical results were obtained using the adiabatic theory within the single-band effective mass approximation, taking

into account the strain in the samples. Both experimentally and theoretically we found that for a wire thickness of up to 8 monolayers, the electron spill-over is inversely related to the wire height. These effects are due to the large zero point energy of the electron. As the wire becomes thicker, the decrease in confinement energy is reflected in a reduction of the electron wavefunction extent.

In chapter 3 of the thesis, I investigated the exciton properties of a QWR in the presence of a magnetic field. I studied the diamagnetic shift, the influence of the electron-hole Coulomb interaction, the electronic properties and the photoluminescence peak energies for magnetic fields applied along and perpendicular to the InAs/InP self-assembled rectangular QWR and GaAs/$Al_{0.4}Ga_{0.6}$As V-shaped QWR. I showed that the Coulomb interaction energy between the electron-hole pair has a relatively small value for the considered flat self-assembled QWRs and a very small change is observed, as the wire height increases. For the V-shaped wire the Coulomb energy between the particles depends more strongly on the dimensions of the wire. I compared the theoretical results on the PL peak energies with the experimental PL measurements in the self-assembled QWRs. A good agreement was found between them in the region of the height of the wire from 4 to 13 ML, when the width is fixed and taken equal to 180 Å. Further, I performed numerical simulations of the diamagnetic shift for InAs/InP self-assembled QWRs. A small deviation from the experiment at high magnetic field is found for both perpendicular and parallel magnetic fields. The results for the diamagnetic shift for the GaAs/$Al_{0.4}Ga_{0.6}$As QWRs show very good agreement between the experimental data and the theoretical curves, where the shape of the wire was assumed to be triangular.

In the next chapter, I presented the results on the charge confinement in a InAs/InP self-assembled QWR and in a InAs/InP QW incorporating local width fluctuations. The vertical confinement is investigated theoretically and experimentally through the study of the exciton diamagnetic shift. From the comparison of the theoretically calculated wavefunction radius with the qualitative measure of the vertical exciton extent obtained from the experimental data, I conclude that the exciton wavefunction spill-over effect in both wires and wells is large. Experimental results of the laser power dependence at different temperatures for InAs/InP QW indicated that the charge carriers are trapped by the well width fluctuations. Therefore, for the calculations in the narrow QW I included a local circular well width fluctuation of 1 ML with radius R. The numerical results of the PL energy for the QW with local width fluctuations showed that the experimentally found high-energy and low-energy PL peaks corresponding to the QW with width of 4 ML and the fluctuation width of 1 ML when the fluctuation radius R is between 25 and 50 Å. The calculated exciton diamagnetic shift in the presence of a perpendicular magnetic field for R=37.5-50 Å agree most closely with the diamagnetic shift of the high-energy peak.

In chapter 5, I studied and analyzed trions in a QWR. The numerical results predict the formation of negative and positive trions in self-assembled InAs/InP QWRs. I theoretically confirm the stability of both trions in V-shaped GaAs/$Al_{0.32}Ga_{0.68}$As wires and compared the binding energy with those measured experimentally. A strong dependence of the $X^{\pm}$ binding energy on the shape and the size of the QWR was found.

In chapter 6, I considered vertically and horizontally coupled InAs/InP self-assembled QWRs. I investigated the optical transitions in such coupled systems. From a comparison with the experimentally observed PL energies, I derived the height of the QWR which is in good agreement with those from the experimental XTEM measurements. No interwire coupling of the exciton in the experimentally grown InAs/InP self-assembled QWRs with period of 180 Å was found. Such coupling effects are predicted to show up when the distance between the wires is smaller than 160 Å. Numerical results for the InAs/InP horizontally coupled system show one coupling regime for all interwire distances. However, for vertically CQWRs, a crossing between the excited states for the particles is predicted when the distance between the wires approaches the value of the wire heights. Due to this crossing, two coupling regimes for InAs/InP vertically CQWRs were found. In the first coupling regime, the electron, heavy-, and light-hole densities for the lowest levels have the same behavior as in a single square wire, while in the second coupling regime, both the energies and densities for the lowest levels act as in ordinary coupled wires. Furthermore, an anticrossing of the energy of excited states was found for vertically coupled wires signaling a change of symmetry of the exciton wave function. This crossing is the signature of two different coupling regimes.

In the last chapter of the thesis I investigated the excitonic properties in the presence of a magnetic field in unstrained GaAs/Al_xGa_{1-x}As QDs. In my 3D calculations, within the single-band effective mass approximation I include the real experimentally measured shape of the QD with the thin well layer on top and asymmetrical barrier materials. I found that the magnetic field dependence of the electron-hole Coulomb interaction energy, when the magnetic field is applied along the x-, y-, and z-direction, follows closely the dependencies of the particle radii (*i.e.*, size) in the xy-plane of the dot. Radii along the z-direction are significantly smaller due to the flatness of the dot, and with increasing magnetic field along the z-direction the particles wavefunction radii become elongated in the z-direction. I also calculated the diamagnetic shift for the exciton ground state and the two first excited states in the presence of a magnetic field applied along the x-, y-, and z-direction in the QD. A good agreement between the experimental results and the calculated heavy-hole exciton is found. By comparing the PL energies, the heavy-hole state is found to be the ground state, and its value is close to the experimental data of the group of Max-Planck-Institut für Festkörperforschung (Stuttgart).

Samenvatting

In deze thesis heb ik de eigenschappen oderzocht van excitonen in kwantumdraden (QWRs) en gerelateerde systemen, kwantumputten (QWs) en kwantumpunten (QDs). De studie van excitonen in deze laag-dimensionele systemen levert waardevolle informatie op over hun karakeristieke eigenschappen. Recent is men er bijvoorbeeld in geslaagd om experimenteel zelf-georganiseerde InAs/InP QWRs te vervaardigen, om eigenschappen van deze draden als ladingslocalizatie, afmetinegn, uniformiteit van de grootte, optische transities en koppeling tussen deze draden verder te onderzoeken. Onze theoretische studie van excitonen draagt ertoe bij om deze karakteristieke eigenschappen te bepalen. Het grootste deel van dit werk handelt over de eigenschappen van excitonen in zelf-georganiseerde InAs/InP QWRs. Verder onderzocht ik excitonen in V-vormige GaAs/AlGaAs QWRs, de invloed van een magneetveld op de eigenschappen van neutrale excitonen in InAs/InP QWs en GaAs/AlGaAs QDs, en geladen excitonen in de hierboven vermeldde V-vormige en zelf-georganiseerde QWRs.

In het eerste hoofdstuk wordt een algemene inleiding tot QWRs gegeven. Mogelijke toepassingen zoals bijvoorbeeld in lasers worden besproken, alsook de verschillende groeitechnieken voor QWRs. Het effect van strain op de localizatie van excitonen wordt besproken samen met de invloed van een magneetveld. De enkele-band effectieve massa benadering die doorheen het verdere werk gebruikt wordt, wordt hier geïntroduceerd.

In het tweede hoofdstuk wordt de ladingslocalizatie in zelf-georganiseerde InAs QWRs onderzocht. De resultaten van onze simulaties worden vergelijken met experimentele magneto-fotoluminiscentie metingen van groepen uit de K. U. Leuven en Instituto de Microelectrónica de Madrid. De theoretische resultaten werden verkregen door gebruik te maken van de adiabatische theorie in de enkele-band effectieve massa benadering, rekening houdend met de strain van de samples. Zowel experimenteel als theoretisch vonden we dat voor een draad met een dikte tot acht lagen, de elektron spill-over omgekeerd evenredig is met de hoogte van de draad. Dit effect kan men wijten aan de grote nulpunts-energie van de elektronen. Als de dikte van de draad toeneemt, zal de bindingsenergie afnemen en dit weerspiegelt zich in een kleinere uitgebreidheid van de golffunctie van het elektron.

In hoofdstuk 3 van de thesis behandelt de exciton-eigenschappen van een QWR in een magneetveld. Ik heb de diamagnetische shift bestudeerd, het effect van de elektron-holte Coulombinteractie, de elektronische eigenschappen en de fotoluminiscentie (PL) piek energieën, zowel voor magneetvelden parallel als loodrecht op een InAs/InP zelf-geassembleerde rechthoekige QWR en een GaAs/$Al_{0.4}Ga_{0.6}$As V-vorm QWR. Er werd aangetoond dat de Coulomb interactie-energie een relatief lage waarde heeft voor de bestudeerde platte zelf-georganiseerde QWRs en slechts een zeer kleine wijziging wordt geobserveerd als de hoogte van de draad toeneemt. Voor de V-vorm draad hangt de Coulomb energie tussen de deeltjes echter sterker af van de dimensies van de draad. Het theoretisch berekende PL spectrum werd ook vergeleken met de experimentele PL resultaten voor de zelf-geassembleerde QWRs. Er is een goede overeenkomst tussen beiden in het gebied waar de hoogte van de draad tussen 4 en 13 ML is en de vaste breedte 180 Å bedraagt. Verder werd de diamagnetische shift voor InAs/InP zelf-geassembleerde QWRs numeriek gesimuleerd. Hier treedt een kleine afwijking t.o.v. de experimentele resultaten op bij grote magneetvelden, zowel voor het parallelle als het loodrechte veld. Het theoretische resultaat van de diamagnetische shift bij GaAs/$Al_{0.4}Ga_{0.6}$As QWRs met driehoekige vorm komt zeer goed overeen met de experimentele data.

In het volgend hoofdstuk worden de resultaten voor ladingsopsluiting in een InAs/InP zelf-georganiseerde QWR getoond en in een InAs/InP QW, rekening houdend met lokale fluctuaties in de breedte. De verticale opsluiting werd theoretisch en experimenteel onderzocht via de studie van de diamagnetische shift van het exciton. Uit de vergelijking van theoretisch berekende golffuncties met experimentele metingen van de verticale uitgebreidheid van het exciton, kunnen we besluiten dat het spill-over effect van de excitongolffunctie in beide draden groot is. Experimentele resultaten van het temperatuursafhankelijke laservermogen bij de InAs/InP QW tonen aan dat de landingsdragers gelokaliseerd worden door de lokale breedtefluctuaties. Daarom werd in de berekeningen voor een smalle QW rekening gehouden met een lokale breedtefluctuatie van 1 ML in de vorm van een cirkelvormige put met straal R. De numerieke resultaten van de PL energie voor de QW met lokale breedtefluctuaties tonen

dat de experimenteel gevonden hoge- en lage-energie pieken in het PL spectrum corresponderen met een QW van 4 ML breed en een fluctuatie van 1 ML, als de straal R tussen 25 en 50 Å is. De berekende diamagnetische shift van het exciton in een loodrecht magneetveld voor $R = 37.5 - 50$ Å komt het best overeen met de diamagnetische shift van de hoge-energie piek.

In hoofdstuk 5 worden trionen in een QWR bestudeerd en geanalyseerd. De numerieke resultaten voorspellen de vorming van negatieve en positieve trionen in zelf-geassembleerde InAs/InP QWRs. Theoretisch bevestig ik de stabiliteit van beide trionen in V-vormige GaAs/$Al_{0.32}Ga_{0.68}$ draden. Een vergelijking met de experimenteel waargenomen bindingsenergieën wordt gegeven. We vonden dat de $X^{\pm}$ bindingsenergie sterk afhankelijk is van de vorm en de grootte van de QWR.

In hoofdstuk 6 worden vertikaal en horizontaal gekoppelde InAs/InP zelfgeassembleerde QWRs beschouwd. Ik onderzocht de optische overgangen in deze gekoppelde systemen. Door vergelijking met de experimenteel geobserveerde PL energieën, kon de hoogte van de QWR afgeleid worden, in goede overeenstemming met deze van de experimentele XTEM metingen. Er werd geen interdraadkoppeling van het exciton gevonden in de experimenteel gegroeide InAs/InP zelf-geassembleerde QWRs met een periode van 180 Å. Het optreden van deze koppelingseffecten wordt voorspeld wanneer de afstand tussen de draden kleiner is dan 160 Å. Numerieke resultaten voor het InAs/InP horizontaal gekoppelde systeem vertonen één koppelingsregime voor alle interdraadafstanden. Voor vertikale gekoppelde QWRs daarentegen, wordt een crossing voorspeld tussen de geëxciteerde toestanden van de deeltjes als de afstand tussen de draden de waarde van de hoogte van de draden nadert. Twee koppelingsregimes voor InAs/InP vertikale gekoppelde QWRs werden gevonden die toe te schrijven zijn aan deze crossing. In het eerste koppelingsregime hebben de elektron-, zware- en lichte-gaten-dichtheden van de laagste niveaus hetzelfde gedrag als in een enkele vierkante draad, terwijl in het tweede koppelingsregime zowel de energieën als de dichtheden van de laagste niveaus zich gedragen als in gebruikelijke gekoppelde draden. Verder werd er ook een anticrossing van de energie van de geexciteerde toestanden bij vertikaal gekoppelde draden gevonden, wat een signaal is van een symmetrieverandering van de golffunctie van het exciton. Deze crossing is de signatuur van twee verschillende koppelingsregimes.

In het laatste hoofdstuk worden de eigenschappen van het exciton in de aanwezigheid van een een magneetveld in onvervormde GaAs/$Al_xGa_{1-x}As$ QDs onderzocht. In mijn 3D berekeningen, binnen de enkele-band effectieve massa benadering, maak ik gebruik van de experimenteel gemeten vorm van de QD met dunne laag op de put en asymmetrische barrièrematerialen. Ik vond dat de magneetveldafhankelijkheid van de electron-hole Coulomb interactieënergie, wanneer het veld aangelegd is volgens de x-, y- en z-richting, zeer nauw de afhankelijkheden van de deeltjesradii (*i.e.*, grootte) volgt in het xy-vlak van de dot. Radii volgens de z-richting zijn significant kleiner als gevolg van de platheid van de dot. Wanneer men het magneetveld volgens de z-richting laat

toenemen, worden de radii van de golffuncties van de deeltjes uitgerekt in de z-richting. Ook de diamagnetische shift van de exciton grondtoestand en de eerste twee geëxciteerde toestanden werden onderzocht in de aanwezigheid van een magneetveld aangelegd volgens de x-, y- en z- richting in de QD. Er werd een goede overeenkomst tussen de experimentele resultaten en de berekende heavy-hole excitonen gevonden. Door vergelijking van de PL energieën, bleek de heavy-hole toestand de grondtoestand te zijn. Zijn waarde ligt zeer dicht bij de experimentele data van de groep van het Max-Planck-Institut für Festkörperforschung (Stuttgart).

References

1. L. Esaki and R. Tsu, IBM J. Res. Dev. **14**, 61 (1970).
2. Zh. I. Alferov, Rev. Mod. Phys **73**, 767 (2001).
3. Y. Arakawa and H. Sakaki, Appl. Phys. Lett. **40**, 939 (1982).
4. E. Kapon, D. M. Hwang, and R. Bhat, Phys. Rev. Lett. **63**, 430 (1989).
5. W. Wegscheider, L. N. Pfeiffer, M. M. Dignam, A. Pinczuk, K. W. West, S. L. McCall, and R. Hull, Phys. Rev. Lett. **71**, 4071 (1993).
6. D. Bimberg, M. Grundmann, and N. N. Ledentsov, *Quantum Dot Heterostructures* (John Wiley & Sons, Chichester, 1999).
7. R. Waser, *Nanoelectronics and Information Technology: Advanced Electronic Materials and Novel Devices* (Wiley-VCH, Weinheim, 2003).
8. L. González, J. M. García, R. García, F. Briones, J. Martínez-Pastor, and C. Ballesteros, Appl. Phys. Lett. **76**, 1104 (2000).
9. J. M. García, L. González, M. U. González, J. P. Silveira, Y. González, and F. Briones, J. Crystal Growth **227**, 975 (2001).
10. F. Suárez, D. Fuster, L. González, Y. González, J. M. García, and M. L. Dotor, Appl. Phys. Lett. **89**, 091123 (2006).

11. Y. Hayamizu, M. Yoshita, S. Watanabe, and H. Akiyama, L. N. Pfeiffer, and K. W. West, Appl. Phys. Lett. **81**, 4937 (2002).

12. C. C. Eugster, J. A. del Alamo, M. J. Rooks, and M. R. Melloch, Appl. Phys. Lett. **64**, 3157 (1994).

13. S. F. Fischer, G. Apetrii, U. Kunze, D. Schuh, and G. Abstreiter, Nature Physics **2**, 91 (2006).

14. C. H. Bennett and D. P. DiVincenzo, Nature (London) **404**, 247 (2000).

15. A. Bertoni, P. Bordone, R. Brunetti, C. Jacoboni, and S. Reggiani, Phys. Rev. Lett. **84**, 5912 (2000).

16. K. F. Karlsson, H. Weman, M.-A. Dupertuis, K. Leifer, A. Rudra, and E. Kapon, Phys. Rev. B **70**, 045302 (2004).

17. X. Duan , Y. Huang, Y. Cui, and C. M. Lieber, Nano Lett. **2**, 101 (2002).

18. Y. Cui and C. M. Lieber, Science **291**, 851 (2001).

19. X. Duan, Y. Huang, and C. M. Lieber, Nano Lett. **2**, 487 (2002).

20. Y. Cui, Q. Wei, H. Park, and C. M. Lieber, Science **293**, 1289 (2001).

21. H. J. Fan, P. Werner, and M. Zacharias, Small **2**, 700 (2006).

22. P. M. Petroff, A. C. Gossard, R. A. Logan, and W. Wiegmann, Appl. Phys. Lett. **41**, 635 (1982).

23. K. Kash, A. Scherer, J. M. Worklock, H. G. Craighead, and M. C. Tamargo, Appl. Phys. Lett. **49**, 1043 (1986).

24. L. Pfeiffer, K. W. West, H. L. Strömer, J. P. Eisenstein, K. W. Baldwin, D. Gershoni, and J. Spector, Appl. Phys. Lett. **56**, 1697 (1990).

25. X.-L. Wang and V. Voliotis, J. Appl. Phys. **99**, 121301 (2006).

26. Y. C. Chang, L. L. Chang, and L. Esaki, Appl. Phys. Lett. **47**, 1324 (1985).

27. A. R. Goñi, L. N. Pfeiffer, K. W. West, A. Pinczuk, H. U. Baranger, and H. L. Störmer, Appl. Phys. Lett. **61**, 1956 (1992).

28. W. Wegscheider, L. N. Pfeiffer, K. W. West, and R. E. Leibenguth, Appl. Phys. Lett. **65**, 2510 (1994).

29. H. Akiyama, T. Someya, and H. Sakaki, Phys. Rev. B **53**, 16160 (1996).

30. T. Someya, H. Akiyama, and H. Sakaki, J. Appl. Phys. **79**, 2522 (1996).

31. R. D. Grober, T. D. Harris, J. K. Trautman, E. Betzig, W. Wegscheider, L. N. Pfeiffer, and K. W. West, Appl. Phys. Lett. **64**, 1421 (1994)

32. T. Someya, H. Akiyama, and H. Sakaki, Phys. Rev. Lett. **74**, 3664 (1995).

33. J. Hasen, L. N. Pfeiffer, A. Pinczuk, H. U. Baranger, K. W. West, and B. S. Dennis, Superl. Microstruct. **22**, 359 (1997).

34. H. Akiyama, J. Phys.: Condens. Matter **10**, 3095 (1998).

35. Y. Takahashi, Y. Hayamizu, H. Itoh, M. Yoshita, H. Akiyama, L. Pfeiffer, and K. West, Appl. Phys. Lett. **86**, 243101 (2005).

36. Y. Takahashi, Y. Hayamizu, H. Itoh, M. Yoshita, and H. Akiyama, Appl. Phys. Lett. **87**, 223119 (2005).

37. E. Kapon, M. C. Tamargo, and D. M. Hwang, Appl. Phys. Lett. **50**, 347 (1987).

38. R. Bhat, E. Kapon, D. M. Hwang, M. A. Koza, and C. P. Yun, J. Cryst. Growth **93**, 850 (1988).

39. Y. Nagamune, Y. Arakawa, S. Tsukamoto, M. Nishioka, S. Sasaki, and N. Miura, Phys. Rev. Lett. **69**, 2963 (1992).

40. E. Kapon, K. Kash, E. M. Jr. Clausen, D. M. Hwang, and E. Colas, Appl. Phys. Lett. **60**, 477 (1992).

41. Y. Nagamune, H. Watabe, F. Sogawa, and Y. Arakawa, Appl. Phys. Lett. **67**, 1535 (1995).

42. R. Ambigapathy, I. Bar-Joseph, D. Y. Oberli, S. Haacke, M. J. Brasil, F. Reinhardt, E. Kapon, and B. Deveaud, Phys. Rev. Lett. **78**, 3579 (1997).

43. G. Biasiol, A. Gustafsson, K. Leifer, and E. Kapon, Phys. Rev. B **65**, 205306 (2002).

44. T. Otterburg, D. Y. Oberli, M.-A. Dupertuis, N. Moret, E. Pelucchi, B. Dwir, K. Leifer, and E. Kapon, Phys. Rev. B **71**, 033301 (2005).

45. E. Levy, A. Tsukernik, M. Karpovski, A. Palevski, B. Dwir, E. Pelucchi, A. Rudra, E. Kapon, and Y. Oreg, Phys. Rev. Lett. **97**, 196802 (2006).

46. E. M. Stellini, K. Y. Cheng, P. J. Pearah, A. C. Chen, A. M. Moy, and K. C. Hsieh, Appl. Phys. Lett. **62**, 458 (1993).

47. K. Y. Cheng, K. C. Hsieh, and J. N. Baillargeon, Appl. Phys. Lett. **60**, 2892 (1992).

48. S. T. Chou, K. Y. Cheng, L. J. Chou, and K. C. Hsieh, Appl. Phys. Lett. **66**, 2220 (1995).

49. A. M. Moy, A. C. Chen, K. Y. Cheng, L. J. Chou, and K. C. Hsieh, J. Crystal Growth **175/176**, 819 (1997).

50. P. J. Pearah, A. C. Chen, A. M. Moy, K. C. Hsieh, and K. Y. Cheng, IEEE J. Quantum Electron. **30**, 608 (1994).

51. B. Alén, J. Martínez-Pastor, A. García-Cristobal, L. González, and J. M. García, Appl. Phys. Lett. **78**, 4025 (2001).

52. D. Fuster, M. U. González, L. González, Y. González, T. Ben, A. Ponce, and S. I. Molina, Appl. Phys. Lett. **84**, 4723 (2004).

53. D. Fuster, M. U. González, L. González, Y. González, T. Ben, A. Ponce, S. I. Molina, and J. Martínez-Pastor, Appl. Phys. Lett. **85**, 1424 (2004).

54. B. Alén, D. Fuster, Y. González, L. González, and J. Martínez-Pastor, Appl. Phys. Lett. **89**, 233126 (2006).

55. S. I. Molina, private communication (2006).

56. N. V. Ashcroft and N. D. Mermin, *Solid State Physics* (Holt, Rinehart and Winston, New York, 1976).

57. J. R. Chelikowsky and M. L. Cohen, Phys. Rev. B **14**, 556 (1976).

58. J. Bardeen, J. Chem. Phys. **6**, 367 (1938).

59. F. Seitz, *The Modern Theory of Solids* (McGraw-Hill Book Company, Inc., New York, 1940).

60. J. M. Luttinger and W. Kohn, Phys. Rev. **97**, 869 (1955).

61. J. M. Luttinger, Phys. Rev. **102**, 1030 (1956).

62. E. O. Kane, J. Chem Phys. Solids **1**, 249 (1957).

63. G. E. Pikus and G. L. Bir, Sov. Phys.-Solid State **1**, 1502 (1959).

64. B. Foreman, Phys. Rev. B. **48**, 4964 (1993).

65. M. A. Dupertuis, F. Vouilloz, D. Y. Oberli, H. Weman, and E. Kapon, Physica E **2**, 940 (1998).

66. O. Stier, *Electronic and Optical Properties of Quantum Dots and Wires*, Vol. 7 of *Berlin Studies in Solid State Physics* (Wissenschaft und Technik Verlag, Berlin, 2001).

67. M. A. Lampert, Phys. Rev. Lett. **1**, 450 (1958).

68. K. Kheng, R. T. Cox, Merle Y. d'Aubigné, Franck Bassani, K. Saminadayar, and S. Tatarenko, Phys. Rev. Lett. **71**, 1752 (1993).

69. J. Bellessa, V. Voliotis, R. Grousson, X. L. Wang, M. Ogura, and H. Matsuhata, Appl. Phys. Lett. **71**, 2481 (1997).

70. A. Hartmann, Y. Ducommun, E. Kapon, U. Hohenester, and E. Molinari, Phys. Rev. Lett. **84**, 5648 (2000).

71. C. Y.-P. Chao and S. L. Chuang, Phys. Rev. B **46**, 4110 (1992).

72. M. Grundmann, 0. Stier, and D. Bimberg, Phys. Rev. B **50**, 14187 (1994).

73. J. Downes and D. A. Faux, J. Appl. Phys. **77**, 2444 (1995).

74. A. Shik, *Quantum Wells: Physics and Electronics of Two Dimensional Systems* (World Scientific, Singapore, 1997).

75. J. R. Madureira, M. Z. Maialle, and M. H. Degani, Phys. Rev. B **66**, 075332 (2002).

76. X.-T. An and J.-J. Liua, J. Appl. Phys. **99**, 123713 (2006).

77. H. Sakaki, Jpn. J. Appl. Phys. **19**, L735 (1980).

78. G. W. Bryant, Phys. Rev. B **29**, 6632 (1984).

79. G. Fishman, Phys. Rev. B **36**, 7448 (1987).

80. D. Chattopadhyay and A. Bhattacharyya, Phys. Rev. B **37**, 7105 (1988).

81. P. Vasilopoulos, P. Warmenbol, F. M. Peeters, and J. T. Devreese, Phys. Rev. B **40**, 1810 (1989).

82. P. Vasilopoulos and F. M. Peeters, Phys. Rev. B **40**, 10079 (1989).

83. Y. Arakawa, Y. Yamauchi, and J. N. Schulman, Phys. Rev. B **43**, 4732 (1991).

84. D. S. Citrin and Y. Chang, IEEE J. Quantum Electron. **29**, 97 (1993).

85. T. Tadić and Z. Ikonić, Phys. Rev. B **50**, 7680 (1994).

86. R. Rinaldi, R. Cingolani, M. Lepore, M. Ferrara, I. M. Catalano, F. Rossi, L. Rota, E. Molinari, P. Lugli, U. Marti, D. Martin, F. Morier-Gemoud, P. Ruterana, and F. K. Reinhart, Phys. Rev. Lett. **73**, 2899 (1994).

87. M. H. Degani and O. Hipólito, Phys. Rev. B **35**, R9345 (1987).

88. J. Hasen, L. N. Pfeiffer, A. Pinczuk, S. He, K. W. West, and B. S. Dennis, Nature (London) **390**, 54 (1997).

89. G. A. Baraff and D. Gershoni, Phys. Rev. B **43**, 4011 (1991).

90. G. Goldoni, F. Rossi, E. Molinari, and A. Fasolino, Phys. Rev. B **55**, 7110 (1997).

91. T. Sogawa, H. Ando, S. Ando, and H. Kanbe, Phys. Rev. B **56**, 1958 (1997).

92. O. Stier and D. Bimberg, Phys. Rev. B **55**, 7726 (1997).

93. M. Notomi, S. Nojima, M. Okamoto, H. Iwamura, T. Tamamura, J. Hammersberg, and H. Weman, Phys. Rev. B **52**, 11073 (1995).

94. F. V. Kyrychenko and J. Kossut, Phys. Rev. B **61**, 4449 (2000).

95. G. W. Bryant and Y. B. Band, Phys. Rev. B **63**, 115304 (2001).

96. J. C. Silva, A. Chaves, J. A. K. Freire, V. N. Freire, and G. A. Farias, Phys. Rev. B **74**, 085317 (2006).

97. M. U. González, J. M. García, L. González, J. P. Silveira, Y. González, J. D. Gómez, and F. Briones, Appl. Surf. Sci. **188**, 188 (2002).

98. I. Vurgaftman, J. R. Meyer, and L. R. Ram-Mohan, J. Appl. Phys. **89**, 5815 (2001).

99. J. M. Worlock, F. M. Peeters, H. M. Cox, and P. C. Morais, Phys. Rev. B **44**, 8923 (1991).

100. K. Oettinger, Al. L. Efros, B. K. Meyer, C. Woelk, and H. Brugger, Phys. Rev. B **52**, R5531 (1995).

101. G. Creci and G. Weber, Semicond. Sci. Technol. **14**, 690 (1999).

102. L. Vescan, T. Stoica, and B. Holländer, Mater. Sci. Eng., B **89**, 49 (2002).

103. S. N. Walck and T. L. Reinecke, Phys. Rev. B **57**, 9088 (1998).

104. A. Balandin and S. Bandyopadhyay, Phys. Rev. B **52**, 8312 (1995).

105. A. Thilagam, Physica B **262**, 390 (1999).

106. H. M. Cox, D. E. Aspnes, S. J. Allen, P. Bastos, D. M. Hwang, S. Mahajan, M. A. Shahid, and P. C. Morais, Appl. Phys. Lett. **57**, 611 (1990).

107. K. Kash, R. Bhat, D. D. Mahoney, P. S. D. Lin, A. Scherer, J. M. Worlock, B. P. Van der Gaag, M. Koza, and P. Grabbe, Appl. Phys. Lett. **55**, 681 (1989).

108. A. P. Roth, P. Finnie, S. Charbonneau, C. Lacelle, C. Gurini, J. Fraser, M. Buchanan, and Y. Feng, Microelectron. J. **28**, 909 (1997).

109. S. Raymond, S. Studenikin, S.-J. Cheng, M. Pioro-Ladrire, M. Ciorga, P. J. Poole, and M. D. Robertson, Semicond. Sci. Technol. **18**, 385 (2003).

110. R. P. Schneider Jr. and B. W. Wessels, J. Appl. Phys. **70**, 405 (1991).

111. F. Guffarth, R. Heitz, A. Schliwa, K. Ptschke, and D. Bimberg, Physica E (Amsterdam) **21**, 326 (2004).

112. J. Maes, M. Hayne, M. Henini, F. Pulizzi, A. Patanè, L. Eaves, and V. V. Moshchalkov, Physica B **346347**, 428 (2004).

113. M. Hayne, R. Provoost, M. K. Zundel, Y. M. Manz, K. Eberl, and V. V. Moshchalkov, Phys. Rev. B **62**, 10324 (2000).

114. K. L. Janssens, F. M. Peeters, and V. A. Schweigert, Phys. Rev. B **63**, 205311 (2001).

115. E. Alphandéry, R. J. Nicholas, N. J. Mason, S. G. Lyapin, and P. C. Klipstein, Phys. Rev. B **65**, 115322 (2002).

116. O. Stier, M. Grundmann, and D. Bimberg, Phys. Rev. B **59**, 5688 (1999).

117. H. Temkin, G. J. Dolan, M. B. Panish, and S. N. G. Chu, Appl. Phys. Lett. **50**, 413 (1987).

118. H. Akiyama, T. Someya, M. Yoshita, and T. Sasaki, H. Sakaki, Phys. Rev. B **57**, 3765 (1998).

119. H. Akiyama, and M. Yoshita, L. N. Pfeiffer, K. W. West, and A. Pinczuk, Appl. Phys. Lett. **82**, 379 (2003).

120. T. Arakawa, Y. Kato, F. Sogawa, and Y. Arakawa, Appl. Phys. Lett. **70**, 646 (1997).

121. G. Goldoni, F. Rossi, E. Molinari, A. Fasolino, R. Rinaldi, and R. Cingolani, Appl. Phys. Lett. **69**, 2965 (1996).

122. F. Rossi and E. Molinari, Phys. Rev. Lett. **76**, 3642 (1996).

123. K. Chang and J. B. Xia, Phys. Rev. B **58**, 2031 (1998).

124. F. Rossi and E. Molinari, Phys. Rev. B **53**, 16 462 (1996).

125. S. Glutsch, and F. Bechstedt, W. Wegscheider, and G. Schedelbeck, Phys. Rev. B **56**, 4108 (1997).

126. S. N. Walck, T. L. Reinecke, and P. A. Knipp, Phys. Rev. B **56**, 9235 (1997).

127. K. Chang and J. B. Xia, Phys. Rev. B **58**, 2031 (1998).

128. H. R. Gutiérrez, M. A. Gotta, and M. M. G. de Carvalho, Appl. Phys. Lett. **79**, 3854 (2001).

129. B. Alén, and J. Martínez-Pastor, L. González, J. M. García, S. I. Molina, A. Ponce, and R. García, Phys. Rev. B **65**, 241301(R) (2002).

130. M. Grundmann, O. Stier, and D. Bimberg, Phys. Rev. B **52**, 11969 (1995).

131. J. Singh, *Semiconductor Devices: Basic Principles* (John Wiley & Sons, 2001).

132. F. B. Pedersen and Y.-C. Chang, Phys. Rev. B **55**, 4580 (1997).

133. D. A. Faux, J. R. Downes, and E. P. O'Reilly, J. Appl. Phys. **80**, 2515 (1996).

134. J. Maes, M. Hayne, Y. Sidor, B. Partoens, F. M. Peeters, Y. González, L. González, D. Fuster, J. M. García, and V. V. Moshchalkov, Phys. Rev. B **70**, 155311 (2004).

135. H. Yu, J. Li, R. A. Loomis, L.-W. Wang, and W. E. Buhro, Nature Materials **2**, 517 (2003).

136. Y. Sidor, B. Partoens, and F. M. Peeters, Phys. Rev. B **71**, 165323 (2005).

137. M. Fritze, I. E. Perakis, A. Getter, W. Knox, K. W. Goossen, J. E. Cunningham, and S. A. Jackson, Phys. Rev. Lett. **76**, 106 (1996).

138. K. Chang and F. M. Peeters, Phys. Rev. B **63**, 153307 (2001).

139. B. R. Johnson, J. O. Hirschfelder, and K.-H. Yang, Rev. Mod. Phys. **55**, 109 (1983).

140. K. J. Nash, M. S. Skolnick, P. A. Claxton, and J. S. Roberts, Phys. Rev. B **39**, 10943 (1989).

141. F. M. Peeters and J. E. Golub, Phys. Rev. B **43**, 5159 (1991).

142. A. B. Dzyubenko and A. L. Yablonskii, Phys. Rev. B **53**, 16355 (1996).

143. G. Eytan, Y. Yayon, M. Rappaport, H. Shtrikman, and I. Bar-Joseph, Phys. Rev. Lett. **81**, 1666 (1998).

144. J. G. Tischler, A. S. Bracker, D. Gammon, and D. Park, Phys. Rev. B **66**, 081310(R) (2002).

145. A. V. Filinov, C. Riva, F. M. Peeters, Y. E. Lozovik, and M. Bonitz, Phys. Rev. B **70**, 035323 (2004).

146. A. S. Bracker, E. A. Stinaff, D. Gammon, M. E. Ware, J. G. Tischler, D. Park, D. Gershoni, A. V. Filinov, M. Bonitz, F. M. Peeters, and C. Riva, Phys. Rev. B **72**, 035332 (2005).

147. D. Fuster, L. González, Y. González, M. U. González, and J. Martínez-Pastor, J. Appl. Phys. **98**, 033502 (2005).

148. P. Caroff, C. Paranthoen, C. Platz, O. Dehaese, H. Folliot, N. Bertru, C. Labbé, R. Piron, E. Homeyer, A. Le Corre, and S. Loualiche, Appl. Phys. Lett. **87**, 243107 (2005).

149. G. L. Bir and G. E. Pikus, *Symmetry and Strain-Induced Effects in Semiconductors* (Wiley, New York, 1974).

150. U. Ekenberg, Phys. Rev. B **40**, 7714 (1989).

151. A. Krotkus and Z. Dobrovolskis, *Electrical Conductivity of Narrow-Gap Semiconductors* (Vilnus, Mokslas, 1988).

152. M. Levinshtein, S. Rumyantsev, and M. Shur, *Handbook Series on Semiconductor Parameters*, Vol. 1 (World Scientific, London, 1996).

153. K. L. Janssens, B. Partoens, and F. M. Peeters, Phys. Rev. B **64**, 155324 (2001).

154. D. Fuster, J. Martínez-Pastor, L. González, and Y. González, Phys. Rev. B **71**, 205329 (2005).

155. C. Wetzel, R. Winkler, M. Drechsler, B. K. Meyer, U. Rössler, J. Scriba, J. P. Kotthaus, V. Härle, and F. Scholz, Phys. Rev. B **53**, 1038 (1996).

156. C. Riva, F. M. Peeters, K. Varga. Phys. Rev. B **61**, 13873 (2000).

157. C. Riva, F. M. Peeters, and K. Varga, Phys. Rev. B **63**, 115302 (2001).

158. F. M. Peeters, C. Riva, and K. Varga, Physica B **300**, 139 (2001).

159. B. Szafran, T. Chwiej, F. M. Peeters, S. Bednarek, and J. Adamowski, Phys. Rev. B **71**, 235305 (2005).

160. A. F. Slachmuylders, B. Partoens, W. Magnus, and F. M. Peeters, Phys. Rev. B **76**, 075405 (2007).

161. F. Vouilloz, D. Y. Oberli, M.-A. Dupertuis, A. Gustafsson, F. Reinhardt, and E. Kapon, Phys. Rev. Lett. **78**, 1580 (1997).

162. See, for example, IEEE J. Quantum Electron. **QE-22**, 1609 (1986).

163. R. Tsu and G. Döhler, Phys. Rev. B **12**, 680 (1975).

164. S. L. Chuang and B. Do, J. Appl. Phys. **62**, 1290 (1987).

165. T. Weil and B. Vinter, J. Appl. Phys. **60**, 3227 (1986).

166. K. Kern, D. Heitmann, R. R. Gerhardts, P. Grambow, Y. H. Zhang, and K. Ploog, Phys. Rev. B **44**, 1139 (1991).

167. H. Weman, M. Potemski, M. E. Lazzouni, M. S. Miller, and J. L. Merz, Phys. Rev. B **53**, 6959 (1996).

168. H. Weman, D. Y. Oberli, M. A. Dupertuis, F. Reinhardt, A. Gustafsson, and E. Kapon, Phys. Rev. B **58**, 1150 (1998).

169. H. X. Li, J. Wu, Z. G. Wang, and T. Daniels-Race, Appl. Phys. Lett. **75**, 1173 (1999).

170. W. Ma, R. Nötzel, A. Trampert, M. Ramsteiner, H. Zhu, H.-P. Schönherr, and K. H. Ploog, Appl. Phys. Lett. **78**, 1297 (2001).

171. C. Pryor, Phys. Rev. Lett. **80**, 3579 (1998).

172. B. Szafran, S. Bednarek, and J. Adamowski, Phys. Rev. B **64**, 125301 (2001).

173. I. Shtrichman, C. Metzner, B. D. Gerardot, W. V. Schoenfeld, and P. M. Petroff, Phys. Rev. B **65**, 081303(R) (2002).

174. K. L. Janssens, B. Partoens, and F. M. Peeters, Phys. Rev. B **66**, 075314 (2002).

175. Y. B. Lyanda-Geller, T. L. Reinecke, and M. Bayer, Phys. Rev. B **69**, 161308(R) (2004).

176. J.-L. Zhu, W. Chu, Z. Dai, and D. Xu, Phys. Rev. B **72**, 165346 (2005).

177. D. Fuster, L. González, Y. González, J. Martínez-Pastor, T. Ben, A. Ponce, and S. I. Molina, Eur. Phys. J. B **40**, 433 (2004).

178. Y. Sidor, B. Partoens, F. M. Peeters, N. Schildermans, M. Hayne, V. V. Moshchalkov, A. Rastelli, and O. G. Schmidt, Phys. Rev. B **73**, 155334 (2006).

179. S. Smith, A. Mascarenhas, and J. M. Olson, Phys. Rev. B **68**, 153202 (2003).

180. M. Hayne, J. Maes, S. Bersier, M. Henini, L. Müller-Kirsch, R. Heitz, D. Bimberg, and V. V. Moshchalkov, Physica B **346-347**, 421 (2004).

181. H. J. Zhu, M. Ramsteiner, K. H. Ploog, R. Zhang, R. Tsui, K. Shiralagi, and H. Goronkin, Phys. Rev. B **62**, R16314 (2000).

182. M. Sugisaki, H.-W. Ren, S. V. Nair, K. Nishi, and Y. Masumoto, Phys. Rev. B **66**, 235309 (2002).

183. M. Hayne, O. Razinkova, S. Bersier, R. Heitz, L. Müller-Kirsch, M. Geller, D. Bimberg, and V. V. Moshchalkov, Phys. Rev. B **70**, R081302 (2004).

184. M. Bayer, O. Stern, A. Kuther, and A. Forchel, Phys. Rev. B **61**, 7273 (2000).

185. D. Reuter, P. Kailuweit, A. D. Wieck, U. Zeitler, O. Wibbelhoff, C. Meier, A. Lorke, and J. C. Maan, Phys. Rev. Lett. **94**, 026808 (2005).

186. S. Raymond, X. Guo, J. L. Merz, and S. Fafard, Phys. Rev. B **59**, 7624 (1999).

187. M. Bayer, O. Stern, P. Hawrylak, S. Fafard, and A. Forchel, Nature (London) **405**, 923 (2000).

188. S. Raymond, S. Studenikin, A. Sachrajda, Z. Wasilewski, S. J. Cheng, W. Sheng, P. Hawrylak, A. Babinski, M. Potemski, G. Ortner, and M. Bayer, Phys. Rev. Lett. **92**, 187402 (2004).

189. F. Pulizzi, D. Walker, A. Patané, L. Eaves, M. Henini, D. Granados, J. M. Garcia, V. V. Rudenkov, P. C. M. Christianen, J. C. Maan, P. Offermans, P. M. Koenraad, and G. Hill, Phys. Rev. B **72**, 085309 (2005).

190. P. Offermans, P. M. Koenraad, J. H. Wolter, K. Pierz, M. Roy, and P. A. Maksym, Phys. Rev. B **72**, 165332 (2005).

191. A. Rastelli, S. Stufler, A. Schliwa, R. Songmuang, C. Manzano, G. Costantini, K. Kern, A. Zrenner, D. Bimberg, and O. G. Schmidt, Phys. Rev. Lett. **92**, 166104 (2004).

192. A. Rastelli, R. Songmuang, O. G. Schmidt, Physica E **23**, 384 (2004).

193. S. S. Li, K. Chang, J. B. Xia, Phys. Rev. B **71**, 155301 (2005).

194. N. Schildermans, M. Hayne, V. V. Moshchalkov, A. Rastelli, and O. G. Schmidt, Phys. Rev. B **72**, 115312 (2005).

195. K. Nishibayashi, T. Okuno, Y. Masumoto, and H.-W. Ren, Phys. Rev. B **68**, 035333 (2003).

Curriculum Vitae

Yosyp SIDOR

DATE OF BIRTH:	17 January, 1980
PLACE OF BIRTH:	Zaluzh, Transcarpathian region, Ukraine
NATIONALITY:	Ukrainian
CONTACT:	Groenenborgerlaan 171, 2020 - Antwerpen
	tel.: +32-(0)3-265.35.40
	e-mail: yosyp.sidor@ua.ac.be

EDUCATION

Year	Graduate Institution	Title of qualification awarded
2002 - present	University of Antwerp, Condensed Matter Theory Group, Department of Physics, Antwerpen	Ph.D. in Physics (expecting)
1997 - 2002	Uzhgorod National University, Department of Physics, Uzhgorod and Institute of Electron Physics, Ukrainian National Academy of Sciences, Uzhgorod	Master in Physics & Engineering (**honour diploma**)

PARTICIPATION AT RESEARCH PROJECTS

Year	Name of project
2002 - 2004	NANOMAT project of the EC Growth program Contract
2002 - present	Flemish Science Foundation (FWO - Vl)
2005 - present	European Commission Network of Excellence: SANDiE
2005 - present	IMEC

THEORETICAL EXPERIENCE

• Numerical modelling based on the finite difference method;
• Numerical modelling based on the finite element technique;
• Mathematical methods: Fourier transformation, Monte - Carlo method, logarithmically weighted method.

COMPUTER SKILLS

• OS: Windows, Microsoft Office, some experience with Linux;

• Programming languages: Fortran (4 years of experience), C++ (1 year of experience), Java (1 year of experience);
• Specialized computing software (advanced level): Technical modelling package COMSOL Multiphysics, MATLAB, Mathematica.

LANGUAGES

Ukrainian (native), English, Russian, Dutch, Hungarian.

INTERESTS

Languages, swimming, computer literature, instrumental music, cooking.

List of publications

1. J. Maes, M. Hayne, Y. Sidor, B. Partoens, F. M. Peeters, Y. González, L. González, D. Fuster, J. M. García, and V. V. Moshchalkov, *Electron wave-function spill-over in self-assembled InAs/InP quantum wires*, Phys. Rev. B **70**, 155311 (2004). **Also** selected for the November 1, 2004 issue of Virtual Journal of Nanoscale Science & Technology.

2. Y. Sidor, B. Partoens, and F. M. Peeters, *Exciton in a quantum wire in the presence of parallel and perpendicular magnetic fields*, Phys. Rev. B **71**, 165323 (2005). **Also** selected for the May 9, 2005 issue of Virtual Journal of Nanoscale Science & Technology.

3. Y. Sidor, B. Partoens, F. M. Peeters, N. Schildermans, M. Hayne, V. V. Moshchalkov, A. Rastelli, and O. G. Schmidt, *High-field magnetoexcitons in unstrained $GaAs/Al_xGa_{1-x}As$ quantum dots*, Phys. Rev. B **73**, 155334 (2006). **Also** selected for the May 15, 2006 issue of Virtual Journal of Nanoscale Science & Technology.

4. Y. Sidor, B. Partoens, F. M. Peeters, T. Ben, A. Ponce, D. L. Sales, S. I. Molina, D. Fuster, L. González, and Y. González, *Excitons in coupled InAs/InP self-assembled quantum wires*, Phys. Rev. B **75**, 125120 (2007). **Also** selected for the April 9, 2007 issue of Virtual Journal of Nanoscale Science & Technology.

5. Y. Sidor, B. Partoens, F. M. Peeters, J. Maes, M. Hayne, D. Fuster, Y. González, L. González, and V. V. Moshchalkov, *Exciton confinement in*

InAs/InP quantum wires and quantum wells in the presence of a magnetic field, Phys. Rev. B, (2007).

6. Y. Sidor, B. Partoens, and F. M. Peeters, *Trions in a quantum wire* (in preparation).